Reproducing the chemical composition of R Coronae Borealis stars from Nucleosynthesis in Post Double Degenerate White Dwarf Mergers

by

Athira A. Menon
B.Sc., University of Mumbai, India, 2009
B.Sc.(Hons.), University of Canterbury, New Zealand 2010

A Thesis Submitted in Partial Fulfillment of the
Requirements for the Degree of

MASTER OF SCIENCE

in the Department of Physics and Astronomy

Reproducing the chemical composition of R Coronae Borealis stars from Nucleosynthesis in Post Double Degenerate White Dwarf Mergers

by

Athira A. Menon
B.Sc., University of Mumbai, India, 2009
B.Sc.(Hons.), University of Canterbury, New Zealand 2010

Supervisory Committee

Dr. Falk Herwig, Main Supervisor
(Department of Physics and Astronomy, University of Victoria)

Dr. Chris Pritchet, Department Member
(Department of Physics and Astronomy, University of Victoria)

Supervisory Committee

Dr. Falk Herwig, Main Supervisor
(Department of Physics and Astronomy, University of Victoria)

Dr. Chris Pritchet, Department Member
(Department of Physics and Astronomy, University of Victoria)

ABSTRACT

The R Coronae Borealis (RCB) stars are an enigmatic class of hydrogen-deficient supergiant stars, which along with the companion classes of Hydrogen-deficient Carbon (HdC) stars and Extreme Helium (EHe) stars, have been touted as being a result of mergers of low mass carbon-oxygen (CO) and helium (He) white dwarfs. Such mergers of white dwarfs are expected to be the genesis of several interesting stellar objects such as Type Ia supernovae, neutron stars and AM CVn stars, amongst others. The RCBs, HdCs and EHes are mostly near-solar mass single stars, which along with having predominantly helium atmospheres that are extremely exhausted in hydrogen and rich in carbon, are also host to some extraordinary nuclear isotopic ratios. The RCBs and EHes have $^{12}C/^{13}C \geq 100$, enhancements of up to 3 orders in fluorine compared to solar and significant amounts of s-process elements. The most outstanding characteristic of RCBs is that they, along with the HdCs, have the lowest O-isotopic ratios measured in any star in the Universe viz., $^{16}O/^{18}O \simeq$ 1-10. We perform nucleosynthesis calculations with conditions found in the three-dimensional hydrodynamic simulations of CO and He WD mergers and compare the nuclear yields thus obtained with those measured in the surfaces of RCB stars. We do not find an agreement between the calculated yields and the measured ones and thus conclude that RCBs are not formed immediately after the merger of the white dwarfs. This leads us to surmise that the surface chemical composition of RCBs may be due to the result of nuclear processes occuring in a longer evolutionary period following the merger. To this end, we first construct chemical compositions of the merged white dwarfs based on the results of the hydrodynamic simulations. We then impose these compositions on homogeneous, spherically symmetric,

one-dimensional stellar models and evolve these models through the giant phase of RCBs. Along with convection zones that develop in the stellar envelope, we induce a continuous envelope mixing profile that is meant to represent processes related to rotation in these merged objects. We then analyse the nuclear yields from the surface of these models and compare them with those of RCBs. Our models achieve the aforementioned striking characteristics of RCBs, viz., the low O-isotopic ratios, high C-isotopic ratios, high fluorine and s-process element enhancments. Along with these, for the first time, we have reproduced simultaneously, the range in observations of almost all the other elements measured in RCBs. Moreover, our one-dimensional models also place useful constraints on so far unexplored three-dimensional processes, thus providing directives for future studies about them.

Contents

List of Tables

List of Figures

ACKNOWLEDGEMENTS

I would like to thank:

Dr. Falk Herwig for being a dedicated mentor and motivating me to work harder and reach further. I've learnt immensely from him and am sure I will continue to do so in the future.

Dr. Pavel A. Denissenkov for all the patient help with the tools and the encouraging reviews of my work.

Our collaborators, Dr. Geoffrey Clayton and Dr. Jan Staff for their insightful perceptions to the bigger picture and the time spent at Louisiana State University.

And the ideal woodsman, **Master Benjamin Hendricks**, for all his help with programming and his ever-reassuring presence.

All intelligent thoughts have already been thought; what is necessary is only to try to think them again.

Johann Wolfgang von Goethe

DEDICATION

To Dad, my strongest believer, who introduced me to Outer Space, Einstein and the Discovery Channel,
To Mom, for teaching me my first words and letters,
To Grandma, for her bountiful love and affection,
And to my friends, old and new, for their moral (and technical) support.
A special mention of my old gang of office 408 for all the good times we have had, that will make me nostalgic about Canada.

Chapter 1

Introduction

1.1 R Coronae Borealis stars

Our Galaxy consists of 10^{10} white dwarfs (WDs), of which 3×10^6 WDs are detected to be in double degenerate (DD) WD systems (Nelemans et al., 2001). WDs are nearly the size of the Earth and are extremely dense objects, supported by the pressure exerted by degenerate electrons. They are the end states of stars with an initial mass between $1 - 8M_{\odot}$. Out of the detected DD WD systems, 19% are CO+CO WDs, 20% are He+He WDs and 61% are CO+He WDs. The merger of these DD WD systems are expected to result in the formation of exotic objects such as Type Ia Supernovae and neutron stars from CO+CO WD mergers (Han, 1998; Nelemans et al., 2001; Napiwotzki et al., 2001), hot Helium subdwarfs (sdO and sdB stars) from He+He WD mergers (Saio & Jeffery, 2000; Han et al., 2002) and the R Coronae Borealis stars (RCBs) along with their companion classes of Hydrogen-deficient Carbon stars (HdCs) and Extreme Helium stars (EHes) from the mergers of the majority of the observed DD systems viz., the CO+He WD systems.

R Coronae Borealis stars (RCBs) are a rare class of hydrogen-deficient stars, that are dominated by helium, are rich in carbon, nitrogen and oxygen and are host to many intriguing chemical characteristics. If RCBs are formed from the evolution of CO+He WD mergers, the spectral database available for these stars will help in unearthing the nucleosynthesis processes that produced their chemical compositions. This will in turn help in tracing the evolutionary history of the progenitor system that led to their formation and allow us to probe the physics in extreme conditions such as those found in WD mergers. Along with these, we can also provide clues in understanding the evolution of the remnants of other WD merger systems.

Alternative to the CO+He WD merger scenario, RCBs are also expected to evolve from the late evolutionary stage of a single star (Renzini, 1990), which undergoes a final flash (FF) ignition of its Helium-shell. Both these scenarios are discussed in detail in section 1.2.1.

RCB stars were first noticed due to their unusual light curves - they are known to rapidly decline (in a few weeks) in their brightness by up to eight orders of magnitude, at irregular intervals, and make slow recoveries (over months to years) back to their initial brightness Fig. 1.1. The first star of this class was found in the Coronae Borealis constellation over 200 years ago (Pigott & Englefield, 1797). Being the first variable star to be recorded in the constellation, it was by nomenclature termed as the 'R'th star of Coronae Borealis, thus coining the name for its class - R Coronae Borealis stars. The strange light curve behaviour of RCBs are not seen in any other variable stars and their huge declines are attributed to clouds of dust appearing in front of them (O'Keefe, 1939; Clayton, 1996), the evidence for which is an omnipresent IR signature around the star (Clayton, 1996). Such deep declines and IR excesses have not been observed in the otherwise chemically similar Hydrogen-deficient Carbon (HdC) stars or the hotter Extreme Helium (EHe) stars. They are all pulsating stars and the formation of dust close to their surface, is deemed to be linked to their pulsation phase (Lawson et al., 1992; Woitke et al., 1996; Crause et al., 2007).

RCBs are near-solar mass F-G type supergiants and are all observed to be single stars (with an exception of the recent discovery of DY Cen (Rao et al., 2012) being in a binary system) and belong to the old, bulge population of the galaxy (Cottrell & Lawson, 1998; Tisserand et al., 2008). Their atmospheres are dominated by helium, are rich in carbon, nitrogen and oxygen and play host to many other intriguing chemical characteristics. These include (Clayton, 2012): large $^{12}C/^{13}C$ ratios, enhancements in fluorine and elements heavier than iron. The most outstanding feature however comes from a relatively recent discovery of their $^{16}O/^{18}O$ ratios ; RCBs have the lowest value of this O-isotopic ratio ever measured in any star in the Universe (Clayton et al., 2007; García-Hernández et al., 2010). Deriving a scenario in which these chemical signatures of RCBs can be obtained, has been the focus of many studies in the past (Saio & Jeffery, 2002; Clayton et al., 2007; Lorén-Aguilar et al., 2009; Staff et al., 2012). A more detailed review of the surface chemical composition of RCBs is done in section 1.3.5.

So far 65 RCBs have been found in our Galaxy and 25 in the Magellanic Clouds by various microlensing groups such as MACHO,OGLE and EROS (Tisserand et al., 2004; Zaniewski et al., 2005; Tisserand, 2012). However with the techniques of Alcock et al. (2001), by extrapolating the population of RCBs in the Large Magellanic Cloud (LMC) and

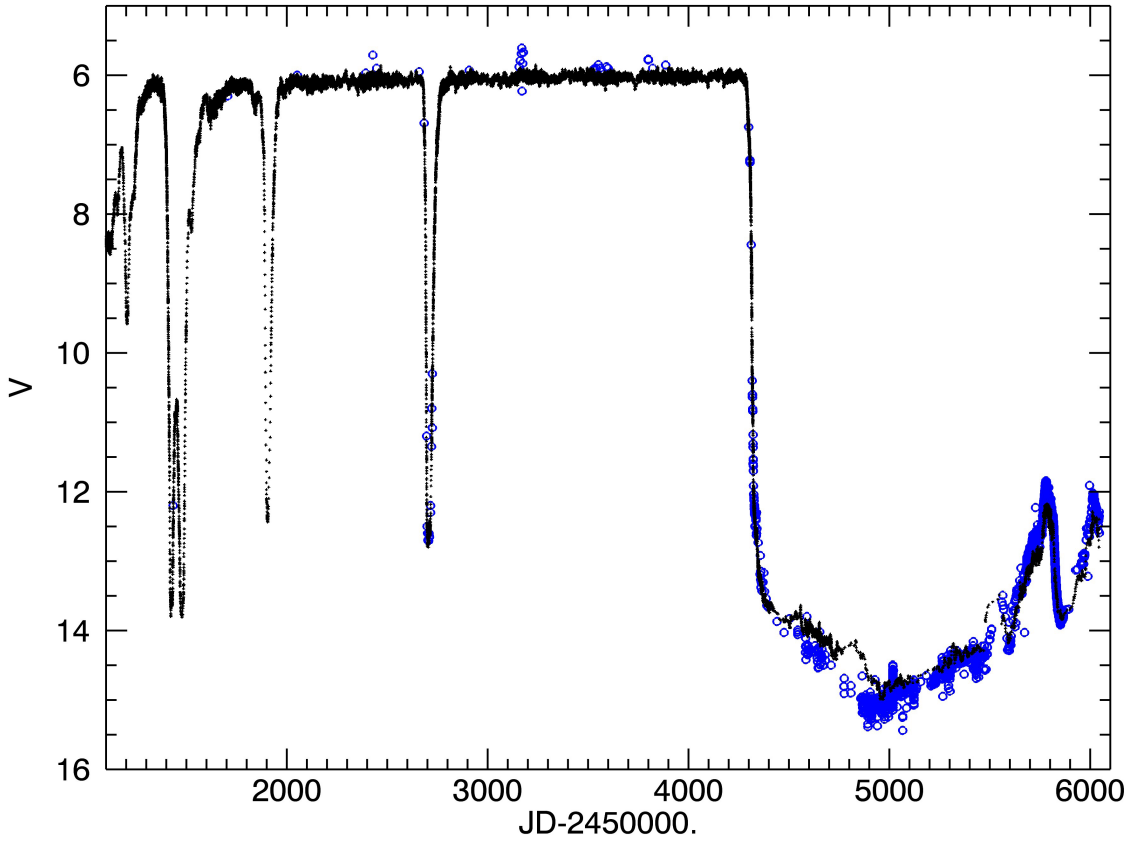

Figure 1.1: Lightcurve of R CrB from 1998-2012 using AAVSO data (Clayton, 2012). Visual magnitudes (V) are plotted as black dots against time in days (JD stands for Julian Date). Blue open circles are V data taken with the Johnson filter.

by considering a DD merger rate of 0.018 yr^{-1} (Han, 1998), the number of RCBs in our Galaxy is expected to be between 5400-5700 (Clayton, 2012). The surface luminosity of RCBs are derived to lie in the range between $3.5 <= \log L/L_{\odot} <= 4.0$ (where $L_{\odot}$ is the solar surface luminosity) for a corresponding range in the effective temperature of the surface (T_{eff}) between $5000\,\mathrm{K} <= T_{\mathrm{eff}} <= 8000\,\mathrm{K}$ (Feast, 1979; Alcock et al., 2001; Tisserand et al., 2009).

1.2 Stellar Evolution

A star is essentially a massive gaseous body that is in hydrostatic equilbrium. It maintains this equilibrium by balancing between gravity (exerted by its mass downwards) and gas and radiation pressure created by nuclear energy generation (which is exerted upwards). The basic structural and chemical evolution of a star through the various nuclear burning phases over its lifetime are discussed below (Ryan & Norton, 2010; Salaris & Cassisi, 2008; Rose, 1998). After igniting hydrogen in its core, a low - intermediate mass star ($1 - 3.5\,M_{\odot}$) (where $M_{\odot}$ is one solar mass) begins its life on the Main-Sequence (MS) Fig. 1.2. Here it spends the majority of its life, fusing hydrogen (H) to helium (He) in the core and begins its next phase when it exhausts the supply of H-fuel. The star then leaves the MS and due to the lack of thermal pressure from nuclear burning, contract under its own weight, until a shell above the He-core is ignited to once again begin H-burning, but now in a shell. The energy provided by the H-shell burning causes the star to inflate to a luminous, cool (red) giant and the star ascends the Red Giant Branch (RGB). The H-fuel in the shell too, is eventually exhausted and the star once more undergoes a period of gravitational contraction. The He-core compresses to such an extent that it becomes increasingly degenerate while continuously increasing its temperature. This degeneracy causes He to ignite in a flash in the core triggering runaway He-fusion to carbon (C) and the star enters the Zero Age Horizontal Branch (ZAHB). Such an He-core flash occurs only for $M \leq 1.75 M_{\odot}$; for higher initial masses, the star ignites He placidly without a flash. During core He-burning, some of the C nuclei capture He nuclei to produce oxygen (O) in the core. Once the He is completely consumed and nuclear burning has stopped in the core, the star again undergoes a period of gravitational compression without a balancing thermal source, until He begins to burn in a shell above the degenerate CO core. The star once again becomes a giant and now ascends the Asymptotic Giant Branch (AGB). Just above the He-burning shell, a very thin H-shell is ignited and above which is a large, convective H-rich envelope Fig. 1.3. The He and H shells go through periodic flashes in luminosity causing the star to thermally pulsate (TP) on the AGB (the wiggles in the AGB portion of Fig. 1.2). During the AGB phase the star losses mass and its duration in this phase is determined by its rate of mass-loss. Once the star leaves the AGB, it turns to the hot Planetary Nebula (PN) phase. The star keeps moving towards hotter temperatures during which time its H-shell extinguishes and the He-shell becomes dormant, thus decreasing its surface luminosity and temperature and causing it to descend the White Dwarf cooling track.

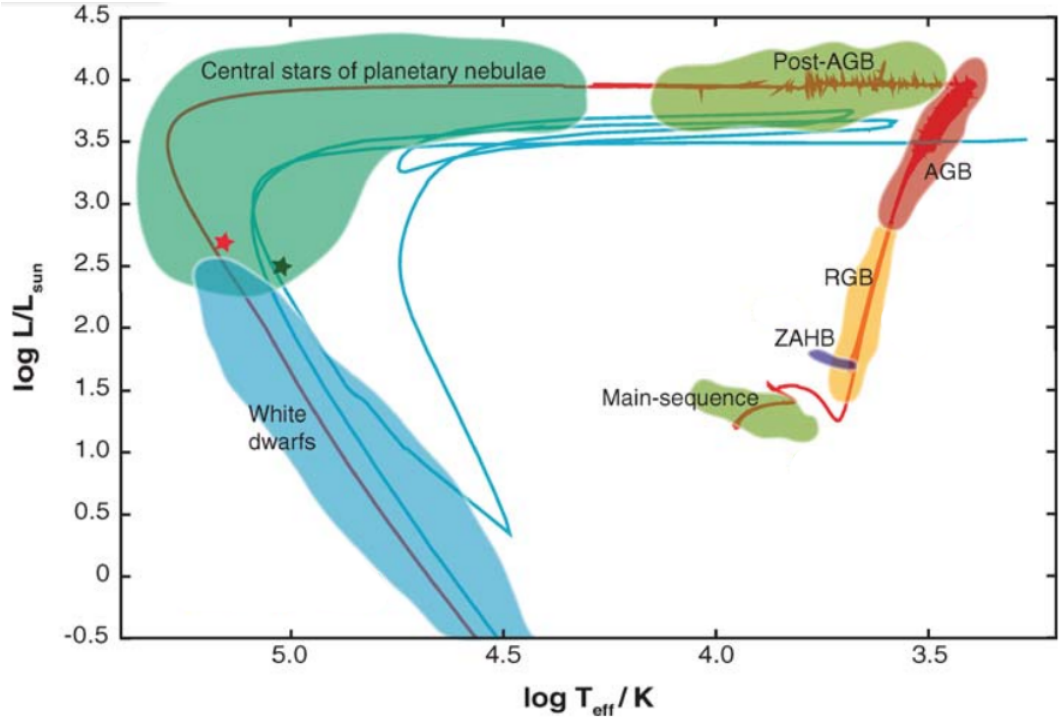

Figure 1.2: Hertzsprung-Russell diagram of a complete 2 $M_{\odot}$ evolution track for solar metallicity from the main sequence to the white dwarf evolution phase, taken from Herwig (2005).

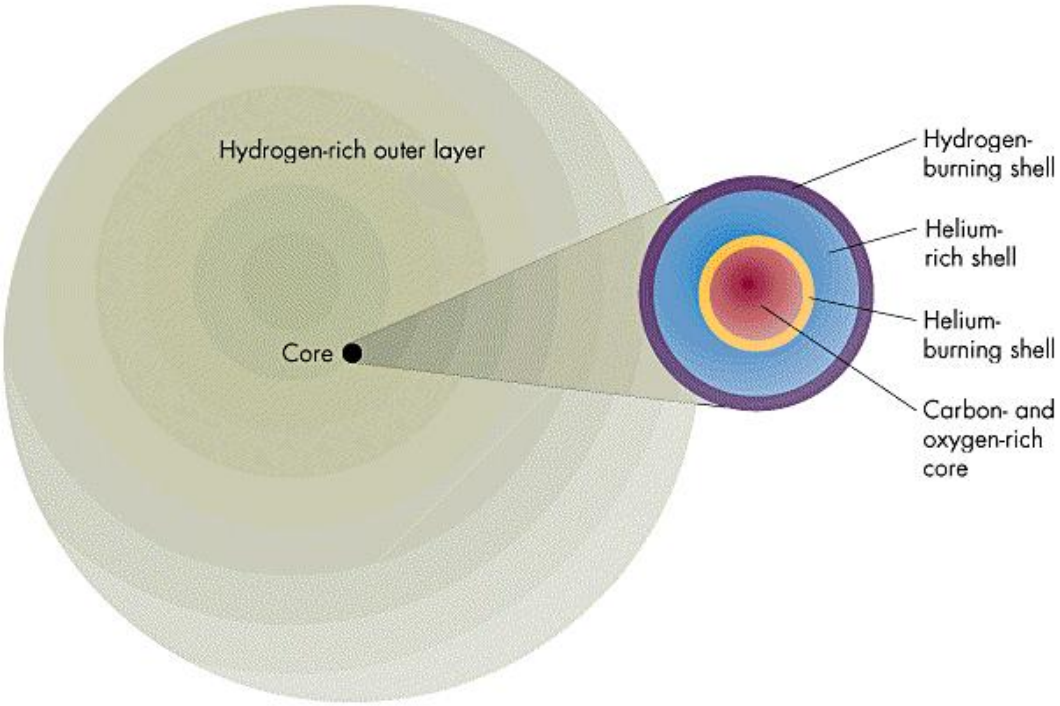

Figure 1.3: The structure of an AGB star. Figure from http://www.mhhe.com /physsci/astronomy/fix/student/chapter19/19f22.html.

1.2.1 Evolutionary channels for RCBs

The fact that RCBs are highly H-deficient and overabundant in He-burning elements (such as C and O) in their surfaces, coupled with their cool temperatures and high luminosities, point to them being in a post-AGB phase of their evolution. AGB stars are known to undergo mass-loss through radiation-powered winds from their surface. But, the rate of such a mass-loss is far too low to completely remove the H-rich envelope of the star before it leaves the AGB. Thus RCBs cannot have formed immediately after departing from the AGB (Asplund et al., 1997). They are therefore, considered to be 'born-again' luminous giants whose progenitor(s) lie on the WD track. Currently there are two competing scenarios put forth to explain the origin of RCBs as re-born stars - the final flash (FF) model involving a single star and the merger of a double degenerate (DD) white dwarf system. However the current consensus leans towards the merger scenario being the more dominant mechanism

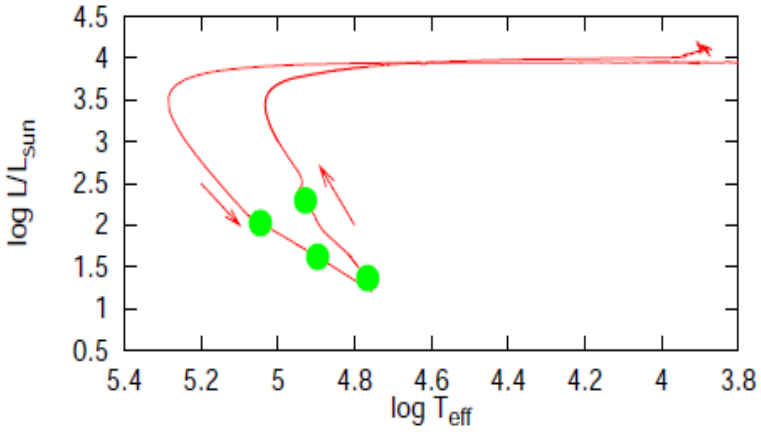

Figure 1.4: Track in the HR diagram of the post-AGB model of (Herwig et al., 1999) during the evolution through a very late TP . At the first mark along the track, the He-flash has already caused a prominent convectively unstable region. At the second mark, the outwards growing convection zone has reached the envelope and protons start to enter the convective zone. At the third mark the hydrogen luminosity has reached its peak. The surface composition is hydrogen-free beyond the last mark as the star evolves to the domain of cool, luminous giants.

to produce RCBs. In the following sections we shall discuss both these scenarios, with a special emphasis on the DD merger scenario and how they compare with the characteristics of RCBs.

The final flash (FF) scenario

When a post-AGB star descends the WD cooling track, there is a possibility for the star to ignite its He-shell in a flash and result in a very late thermal pulse (VLTP) (Herwig, 2001). About 10-15% of all post-AGB stars are expected to undergo such an FF after the H-shell has been extinguished (Renzini, 1990; Asplund, 1999). The He-shell flash forms a convective zone that ingests the residual hydrogen in the envelope. This H-ingestion into the convective He-burning shell, results in a large, positive entropy barrier that causes the shell to split in to two separate convective shells (Renzini, 1990; Herwig et al., 2011). In the base of the upper shell (closer to the surface) H-burning occurs, while in the base of the lower shell, He-burning occurs. The energy released by the top H-burning shell, causes the star to reinflate to a cool, luminous giant (Renzini, 1990) (Fig. 1.4). The lifetime of the star in this 'born-again' giant phase is determined by the amount of H in the envelope.

Evolution leading to a binary WD system

Most stars in our galaxy are found in multiple systems, particularly in binary systems (Popova et al., 1982). Many processes are at play during the evolution of these systems, such as gravitational wave radiation (GWR), magnetic stellar winds (MSW) and magnetic braking, tidal interactions and the transfer of mass from one component of the binary system to the other (Iben & Tutukov, 1984; Iben & Webbink, 1987; Webbink & Iben, 1987). Those systems that are close enough to allow mass-transfer between them are called 'interacting binaries' and almost 50 % of binary systems are close interacting binaries. Most interacting binaries are low-intermediate mass systems (Iben & Tutukov, 1984, 1987). The exchange of mass during a binary evolution causes changes in the separation distance between the two stars, their orbital period and individual structures as well. Typically a binary system is addressed by the mass ratio between its components, $q = M_2/M_1$ where M_1 is the more massive component called the primary and M_2 is the secondary component.

Before beginning with the actual process of transfer of mass, it is important to understand the three types of timescales associated which stellar events. These are the dynamic, thermal and nuclear timescales (Ryan & Norton, 2010; Salaris & Cassisi, 2008). The dynamical timescale ($\tau_{\rm dyn}$) is the minimum time required for one part of a star to communicate a change to another part. If a change takes place faster than the dynamical timescale, then the star cannot come back to hydrostatic equilibrium in that timespan and responds to the change by expanding or contracting itself. The thermal timescale ($\tau_{\rm the}$) is the time taken by the star to radiate all its luminosity when its nuclear reactions are cut off. This is the timescale that determines how quickly a star contracts before the onset of nuclear fusion, during the evolution of the star. The nuclear timescale ($\tau_{\rm nuc}$) is the time required for the star to exhaust its nuclear fuel and hence determines the period of a given nuclear burning phase in the star. For a given star, $\tau_{\rm dyn} << \tau_{\rm the} << \tau_{\rm nuc}$.

Next, we look at how mass-transfer can occur from one component to another during their interaction phase. Mass is accreted from one star to another via two ways - one is by stellar wind and the other more efficient way is by a Roche-lobe overflow of one or both the stars. The Roche lobe is the volume within which material is gravitationally bound to the star. It is a teardrop-shaped space surrounding each star which is determined by drawing equipotential surfaces around both stars. A unique equipotential contour intersects itself at what is called the inner Lagrangian point 'L1' thus defining two regions, one around each star (de Loore & Doom, 1992). When a star expands as a giant and exceeds the size of its Roche lobe, mass from it can be transferred through L1 to its companion (Fig. 1.5). This

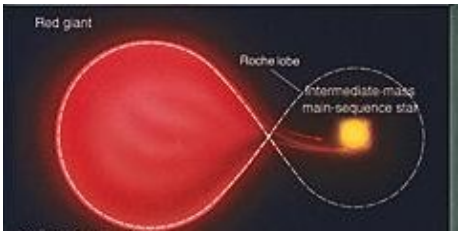

Figure 1.5: Mass-transfer by Roche-lobe overflow from a red giant to a main sequence companion.

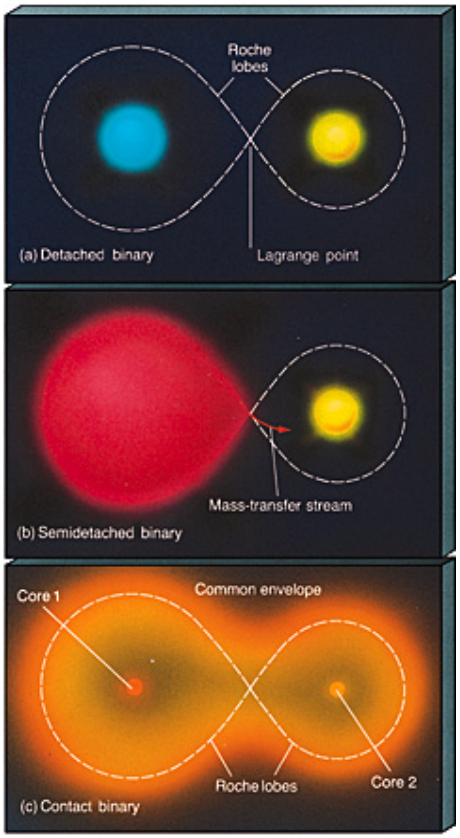

Figure 1.6: The evolution of a detached binary system of main-sequence stars to a contact binary system .

mechanism of mass-transfer is called the Roche-lobe overflow (RLOF) and it occurs when the orbital period of the system is $\leq$ 1000 days (Podsiadlowski, 2008b).

The Roche-lobe radius of a star ($R_{\rm L}$) is determined by the value of q and the separation (A) between the two stars. For star 1 with $q = M_1/M_2$,

$$\frac{R_{\rm L}}{A} = \frac{0.49q^{2/3}}{0.6q^{2/3} + ln(1 + q^{1/3})} \tag{1.1}$$

For star 2, $R_{\rm L}$ is calculated from Eq. 1.1 with $q = M_2/M_1$.

Let us consider an initially non-interacting 'detached' binary system consisting of two main sequence (MS) stars of masses M_1 (primary) and M_2 (secondary), $M_2 < M_1$ (Fig. 1.6(a)). A star can overfill its Roche-lobe spontaneously, typically when it expands to a giant. Since the primary is the more massive component of the system, it will be evolve faster to a giant.

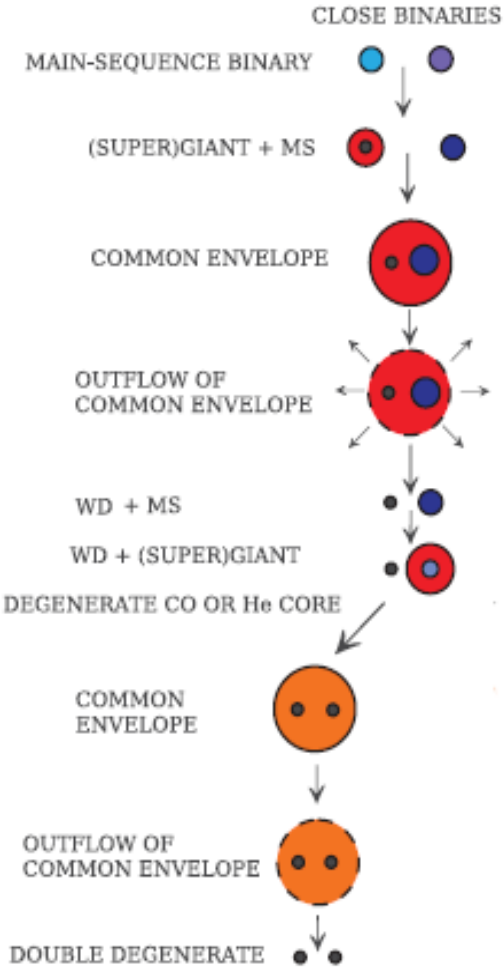

Figure 1.7: Evolution of a close binary MS system to a double degenerate WD system (figure from Solheim (2010)).

Mass-transfer can occur via in a stable or unstable manner, which is decided by two factors - the mass ratio $q = M_2/M_1$ and whether the giant star (M_1) overfilling its Roche lobe has a fully convective envelope (Podsiadlowski, 2008a). If $q > q_{\rm crit} = 0.67$ (Paczyǹski, 1976) (this value is expected to be even lower at 0.4, Marcello private comm. with Staff) and the giant has a completely convective envelope, then the RLOF is dynamically unstable.

In the stable manner, the primary begins to overfill its Roche lobe when it becomes a red giant star (now called the donor) with a degenerate He core but without a fully convective envelope and mass is accreted on to the secondary (now called the accretor). The H-rich envelope of the donor red giant is lost mostly in the transfer of mass to the accretor, while some of it may be lost from the system as well. At the end of this stable mass-transfer

phase, the orbit is widened (to conserve angular momentum) and the donor is transformed to a degenerate He WD with a small H-rich envelope, while the companion becomes a more massive MS star. Such a binary system, where mass is transferred from one component to the other is called a 'semi-detached binary' (Podsiadlowski, 2008b) (Fig. 1.6(b)).

The situation is dramatically different in the other case. When the RLOF of the donor giant becomes dynamically unstable, mass is transferred rapidly from it to the companion MS star. The companion is unable to accommodate the large rate of mass being accreted on to it and maintain its hydrostatic equilibrium, thus causing the companion MS too to overfill its Roche lobe. The envelope of the donor engulfs both the stars and leads to a CE formation (Fig. 1.6(c)). By conventional notion, in order for an unstable RLOF to occur, the primary must be a red giant with a deep convective envelope (typically at the tip of the RGB). This is because mass-loss from a convective giant causes the star to become larger in radius and at the same time shrinks its Roche lobe radius due to its mass being decreased by mass-transfer to the accretor. Thus the donor overfills its Roche lobe at an increasing rate and a runaway mass-transfer is ensued. Such a system where both stars fill their Roche lobes is called a 'contact binary' (Podsiadlowski, 2008a). However recent work by (Passy et al., 2012) counter this notion of unstable RLOF of a convective giant where they found that mass-loss from a convective giant does not increase its radius but actually decreases it.

During a CE event, friction between the core of the donor and the companion star causes orbital energy from the system to be transferred to the common envelope. As more orbital energy is expelled to the envelope, angular momentum decreases in the system and the two components inspiral towards each other. When the orbital energy released is large enough to unbind the common envelope, it is ejected and we are left with the core of the donor and the companion star in a short-period orbit of hours to a few days. A CE event lasts for only a few years (De Marco et al., 2011) and because of its short duration, the companion star is unable to accrete any of the mass of the donor and emerges largely unchanged after the CE phase. Many short-period binaries are observed such as cataclysmic variables, subdwarf B binaries, low mass X-ray binaries and those stars that have been thought to form from the mergers of WDs such as the RCBs and other hydrogen-deficient stars (EHes and HdCs) (Webbink, 1984), Type Ia supernovae and neutron stars (Iben & Tutukov, 1984; Nelemans et al., 2001; Napiwotzki et al., 2001) are expected to have undergone atleast one CE event during their evolution.

There are many formulations in literature that approximates the shrinking of the orbital distance between the stars after a CE event occurs. For our purposes we use the first-order

approximative α-formalism of Iben & Tutukov (1984) to calculate this shrinking (Eq. 1.2).

$$\frac{M_1^2}{A} = \alpha \frac{M_{1,\mathrm{R}} M_2}{A_\mathrm{f}} \tag{1.2}$$

Here, M_1 and M_2 are the mass of the primary and secondary at the time of the CE event, $M_{1,\mathrm{R}}$ is the remnant of the primary after the CE phase and A and A_f are the separation between the stars before and after the CE event. α is the parameter that decides the efficiency of how the orbital energy is used to unbind the common envelope viz., $\alpha = \frac{E_\mathrm{bin}}{\Delta E_\mathrm{orb}}$, which is typically ≤ 1.

Formation of a low mass CO+He WD system

An RCB star is expected to form out of the merger of a degenerate pair of CO and He WDs. The formation of such a double degenerate (DD) WD system occurs through two mass-transfer phases and requires atleast one CE event (Webbink, 1984; Iben & Tutukov, 1984; Han, 1998; Nelemans et al., 2001). This is supported observationally, as all the double WD (DWD) systems are measured to have $q > q_\mathrm{crit}$, which indeed confirms that these systems have undergone atleast one CE event during their evolution (Maxted et al., 2002; De Marco et al., 2011).

A possible binary evolution scenario that would lead to a DD CO and He WD system, was charted by Iben et al. (1996). To illustrate this, we again consider a close binary system of low-intermediate mass main sequence stars, M_1 and M_2, $M_1 > M_2$ (Fig. 1.7). When the primary M_1 evolves to become an AGB star with a degenerate CO core, it fills its Roche-lobe and mass-transfer occurs via RLOF to the secondary. This RLOF is unstable and thus the first CE event takes place, with the donor AGB star's envelope engulfing the companion M_2. This common envelope is ejected leaving behind a CO WD and the nearly unchanged MS star M_2, in an orbit that has decreased by a factor typically between 4-15 (depending on M_1,M_2 from Eq. 1.2) from its initial amount. Later, when M_2 evolves into a giant with a degenerate He core, it too overflows its Roche lobe and transfers mass on a dynamic timescale to the CO WD, thus ensuing a second CE event. The orbit shrinks even further and after the outflow of the common envelope, the end result is of a system consisting of a degenerate CO and He WD (CO+He WD).

An alternative channel of evolution outlined by Iben et al. (1996), is when a stable RLOF of the red giant M_1 leads to the formation of a degenerate He WD and a more massive MS ($> M_2$) companion. The massive companion then evolves to a star on the AGB, with a

degenerate CO core and overfills its RLOF. This RLOF is unstable and a CE event ensues, shrinking the orbital distance between the two components and causing an outflow of the envelope. At the end of this one gets a degenerate He + CO WD system. Such stable mass-transfer systems are considered to be rare; they are deemed to be possible only for the extremely low values of q.

Through either channel, the orbital period should be $\sim$ few hours for the double degenerate WD system to merge within the lifetime of the Universe (Marsh et al., 1995). This happens through a continuous loss of angular momentum from the system, caused by the exchange of GWR and MSW, that decreases the orbital separation between the two WDs. Eventually the He WD is tidally disrupted by the more massive CO WD. This causes the He WD (the donor) to overfill its Roche-lobe and transfer mass in a dynamically unstable manner to the CO WD (the accretor). The RLOF is unstable due to the donor being supported by degeneracy (electron) pressure, which causes it to expand as it loses mass, thus increasing the mass-transfer rate with time (Lorén-Aguilar et al., 2009). Ultimately the entire He WD is disrupted by the CO WD and settles over the accretor in a dynamic timescale of 100-1000 seconds (Dan et al., 2012; Staff et al., 2012; Raskin et al., 2012). This timescale is so short that the accretor cannot incorporate the mass of the donor. Hence the donor settles as a radially large thick disk around the accretor. The merger remnant is expected to evolve into a spherically symmetric star undergoing solid body rotation, with an He-burning shell that puffs it up to an RCB-like luminous, cool supergiant (Saio & Jeffery, 2002; Clayton et al., 2007; Schwab et al., 2012).

1.2.2 RCBs from FF or DD - the stellar evolution perspective

Both, the FF and the DD scenarios, predict a higher number of RCBs than what is observed; the FF scenario would produce 30-2000 galactic RCBs (Iben et al., 1996) as while the DD scenario is expected to produce between 5400-5700 RCBs (Clayton, 2012). Sky surveys such as SPY (Nelemans et al., 2005; Brown et al., 2011a; Badenes & Maoz, 2012) have discovered atleast a 100 binary WD systems. Out of this a significant number of systems are found to be short-period binaries (Brown et al., 2011b; Marsh et al., 1995); the Extremely Low-Mass (ELM) survey has found 24 such systems to date (Kilic et al., 2012). In particular for RCBs, the merger rate of CO+He WD systems is deduced to be $\sim$0.0018/year (Han, 1998). Using this merger rate, the expected number of RCBs resulting from such a merger is calculated to be at 5,400, which is very close to the estimated number of RCBs obtained by extrapolating the Large Magellanic Cloud RCB population viz., 5,700 (Clayton, 2012).

The mass of RCBs is estimated to be between 0.8-0.9 $M_{\odot}$ (Weiss, 1987; Saio, 2008) through stellar-evolution pulsation modelling. This tallies well with the combined mass of low-mass merged WD systems, but does not agree well with the candidates of FF stars viz., the mass of single WDs, which are found to predominantly lie between 0.55-0.6 $M_{\odot}$ (Bergeron et al., 2007). The inferred lifetime of a 1 $M_{\odot}$ WD after it has undergone a late He-shell flash to become an RCB star, is of a few years (Schönberner, 1986; Renzini, 1990). This timescale, is far too small compared to the observed lower limit of 200 years of existence of the prototype of this class, R CrB. There have been three FF objects detected so far; Sakurai's object (V4334 Sgr) (Asplund et al., 1997), FG Sge (Gonzalez et al., 1998) and V605 Aql (Clayton et al., 2006). Two years after its outburst in 1921, V605 Aql had a temperature of $T_{\rm eff}$=5000 K. However it has evolved since then to its present state of $T_{\rm eff}$=95000 K, which is far hotter than all known RCBs. Sakurai's object which was found to have $T_{\rm eff}$ =7000 K, is expected to evolve along a similar path (Kerber et al., 2002; Hajduk et al., 2005). Thus overall, FF objects seem to have much shorter duration as RCBs than required. On the other hand, the supergiant star evolving from a merged CO + He WD system is expected to stay in the RCB phase for $\sim 10^4$ years (Clayton, 2012).

The outburst of Sakurai's object was detected in 1996, three years after which it became enshrouded in dust, during which time the light curve of Sakurai's object dipped to > 10 mag, which is much higher than those of RCBs. Since FF objects originate from hot central stars surrounded by a PN, the detection of such PNs is mandatory for RCBs as well, if they are produced via an FF. However there have been only three RCBs discovered so far (UW Cen, R CrB and V348 Sgr) with a PN around them (Clayton, 2000) and thus is not a characteristic observed in most RCBs.

Thus based on number statistics, evolutionary timescales and other observational features, the DD merger scenario is more favoured as the progenitor of RCBs. A more decisive inference can be arrived at by studying the distribution of elements in the surface of these stars.

1.3 Nucleosynthesis

The temperature in the interior of stars is so hot that chemical species exist in the form of nuclei. The assembly of reactions that involve the creation, destruction or transformation of nuclear species is called nucleosynthesis. After the Big Bang, once the Universe cooled down to allow protons and neutrons to assemble from quarks, nucleosynthesis processes in

the first few minutes following the Big Bang created hydrogen, deuterium, lithium, unstable isotopes of beryllium and helium (Wagoner, 1973), as discovered in a historic paper by the authors Alpha-Bethe-Gamow. 75% of our Universe is made of hydrogen and 25% of helium. The seminal work by Burbidge, Burbidge, Fowler and Hoyle (BBFH) in 1957, showed how heavier elements than helium, which occupied the rest of the periodic table, were made in the interiors of stars. Stellar nucleosynthesis encompasses processes such as the fusion of nuclei and proton, neutron and alpha particle capture reactions on them.

The various nuclear burning processes that occur during the evolution of a star, primarily depend on the initial mass of the star; a star lying in a particular mass range can produce only a particular set of nuclear yields. Hence by measuring the abundances of elements in the surface of a star, one can deduce the nuclear reactions that created them, which in turn depend on the internal structure, temperature and density conditions of the star. Thus, on identifying the nucleosynthesis processes responsible for the surface chemical composition of RCB stars, one can draw conclusions about whether they may have originated from the DD merger or the FF scenario.

In the following sections, we enumerate various nuclear burning processes that occur in the interior of stars. RCBs are low mass stars and their progenitors are also considered to be stars of low - intermediate masses. Hence we will direct our focus on nucleosynthesis processes occuring in low-intermediate mass stars. We first begin with a brief introduction to the nomenclatures used in nuclear astrophysics.

1.3.1 Measuring the chemical composition of star

The standard representation of nuclear species is ${}^{A}\mathrm{X}_{Z}$, where X stands for the element, Z stands for the atomic number (the number of protons) and A for the mass number (the sum of the number of neutrons and protons). A given element is identified by its value of Z but it can have variants with different number of neutrons, and hence A, called isotopes. For example, carbon has two stable isotopes ${}^{12}\mathrm{C}$ and ${}^{13}\mathrm{C}$, ${}^{12}\mathrm{C}$ being the more copious one.

The measurement of how abundant a nuclear species is in a stellar atmosphere, is made in terms of its 'mass fraction'. For a particular species i in a region of mass between mass coordinates m_1 and m_2, it is given by $X_i = \int_{m_1}^{m_2} M_i(m)\,\mathrm{dm} / \int_{m_1}^{m_2} \mathrm{dm}$, where $M_i(m)$ stands for the mass of the species at mass coordinate m. Since hydrogen and helium are the most dominant species in the Universe ($\sim 90\%$), their mass fractions in a given star are specially assigned by the symbols X and Y respectively. All the other nuclear species in the stars are collectively called 'metals' and their total mass fraction is designated as Z, such that

Z=1-(X+Y). The values of X,Y and Z of a star are important indicators of the evolution phase that the star is in. For the Sun, which is a low mass main-sequence star, these values are : X=0.70, Y=0.28 and Z=0.02.

A widely used representation of surface chemical abundances by astronomers, is the absolute abundance ϵ_i, given by $\epsilon_i \equiv \log\, n_i + C$, n_i being the relative number fraction of species i and C being a constant (Jeffery et al., 2011). Another notation of abundances, is the [X] value of the element, which tells how much an element is enhanced or depleted with respect to the solar value viz., $[X_i] = \epsilon_{i_\star} - \epsilon_{i_\odot} = \log n_{i_\star} - \log n_{i_\odot}$. The unit of measurement used here is 'dex' and as this is a logarithmic representation, 1 dex stands for an order of magnitude. Thus if $[X_i]$=+1, then the element i is enhanced by 10 times compared to its solar value.

1.3.2 Central nuclear burning phases

When a star begins its life on the main sequence, the composition of the core is dominated by hydrogen. Hence the first phase of stable burning is that of hydrogen (or proton) fusion, which is triggered when the temperature in the core reaches an order of 10^7 K. There are two ways hydrogen fuses into helium - the proton-proton (pp) chain or the Carbon-Nitrogen-Oxygen (CNO) cycle. In both these reaction sets, a net of four hydrogen nuclei fuse to form one helium nucleus. Generally, both reaction sets occur simultaneously during H-burning, one more efficiently than the other. In the case of low-mass stars, such as the Sun, where the core temperature is $\leq 1.5 \times 10^7$ K, the pp chain is the more dominant method of hydrogen fusion (Ryan & Norton, 2010). It begins with two hydrogen nuclei combining to form a nucleus of deuterium or deuteron. The deuteron then reacts with another proton to form a ${}^3_2$He nucleus.

$$\begin{aligned} {}^1_1\mathrm{H} + {}^1_1\mathrm{H} + &\longrightarrow {}^2_1\mathrm{D} + \mathrm{e}^+ + \nu_\mathrm{e} \\ {}^2_1\mathrm{D} + {}^1_1\mathrm{H} + &\longrightarrow {}^3_2\mathrm{He} + \gamma \end{aligned} \tag{1.3}$$

The proton-proton chain itself has three branches. The most dominant one is the pp(I) chain where the ${}^3_2$He nuclei combine to form one ${}^4_2$He nucleus.

$${}^3_2\mathrm{He} + {}^1_1\mathrm{H} + \longrightarrow {}^4_2\mathrm{He} + \gamma \tag{1.4}$$

Once there is a significant amount of ${}^{4}_{2}\mathrm{He}$ available, the ${}^{3}_{2}\mathrm{He}$ nucleus can capture a ${}^{4}_{2}\mathrm{He}$ nucleus, to form beryllium-7 which then captures an electron to form lithium-7. ${}^{7}_{3}\mathrm{Li}$ captures a proton to produce two ${}^{4}_{2}\mathrm{He}$ nuclei. This is the pp(II) chain :

$$\begin{aligned} {}^{3}_{2}\mathrm{He} + {}^{4}_{2}\mathrm{He} + &\longrightarrow {}^{7}_{4}\mathrm{Be} + \gamma \\ {}^{7}_{4}\mathrm{Be} + \mathrm{e}^{-} &\longrightarrow {}^{7}_{3}\mathrm{Li} + \nu_{\mathrm{e}} \\ {}^{7}_{3}\mathrm{Li} + {}^{1}_{1}\mathrm{H} + &\longrightarrow {}^{4}_{2}\mathrm{He} + {}^{4}_{2}\mathrm{He} \end{aligned} \tag{1.5}$$

The least frequent chain is the pp(III), where the ${}^{7}_{4}\mathrm{Be}$ nucleus reacts with a proton to form a boron-8 nucleus, which then undergoes beta-decay to form a ${}^{8}_{4}\mathrm{Be}$ nucleus, which itself decays to two ${}^{4}_{2}\mathrm{He}$ nuclei.

$$\begin{aligned} {}^{7}_{4}\mathrm{Be} + {}^{1}_{1}\mathrm{H} &\longrightarrow {}^{8}_{5}\mathrm{B} \\ {}^{8}_{5}\mathrm{B} &\longrightarrow {}^{8}_{4}\mathrm{Be} + \mathrm{e}^{+} + \nu_{\mathrm{e}} \\ {}^{8}_{4}\mathrm{Be} &\longrightarrow {}^{4}_{2}\mathrm{He} + {}^{4}_{2}\mathrm{He} \end{aligned} \tag{1.6}$$

In the case of more massive stars ($\geq 1.2 - 1.3\, M_{\odot}$), where the core temperature (T_{c}) can reach $\geq 1.5 \times 10^{7}\,\mathrm{K}$, the CNO cycle dominates over the pp chain (Salaris & Cassisi, 2008). In order to begin this method of H-burning, the isotopes of C,N and O are required as initial seeds. It is comprised of two parts - the CN and NO cycles:

The CN cycle:

$$\begin{aligned} {}^{12}_{6}\mathrm{C} + {}^{1}_{1}\mathrm{H} &\longrightarrow {}^{13}_{7}\mathrm{N} + \gamma \\ {}^{13}_{7}\mathrm{N} &\longrightarrow {}^{13}_{6}\mathrm{C} + \mathrm{e}^{+} + \nu_{\mathrm{e}} \\ {}^{13}_{6}\mathrm{C} + {}^{1}_{1}\mathrm{H} &\longrightarrow {}^{14}_{7}\mathrm{N} + \gamma \\ {}^{14}_{7}\mathrm{N} + {}^{1}_{1}\mathrm{H} &\longrightarrow {}^{15}_{8}\mathrm{O} + \gamma \\ {}^{15}_{8}\mathrm{O} &\longrightarrow {}^{15}_{7}\mathrm{N} + \mathrm{e}^{+} + \nu_{\mathrm{e}} \\ {}^{15}_{7}\mathrm{N} + {}^{1}_{1}\mathrm{H} &\longrightarrow {}^{12}_{6}\mathrm{C} + {}^{4}_{2}\mathrm{He} \end{aligned} \tag{1.7}$$

The NO cycle:

$$\begin{aligned} {}^{15}_{7}\mathrm{N} + {}^{1}_{1}\mathrm{H} &\longrightarrow {}^{16}_{8}\mathrm{O} + \gamma \\ {}^{16}_{8}\mathrm{O} + {}^{1}_{1}\mathrm{H} &\longrightarrow {}^{17}_{9}\mathrm{F} + \gamma \\ {}^{17}_{9}\mathrm{F} &\longrightarrow {}^{17}_{8}\mathrm{O} + \mathrm{e}^{+} + \nu_{\mathrm{e}} \\ {}^{17}_{8}\mathrm{O} + {}^{1}_{1}\mathrm{H} &\longrightarrow {}^{14}_{7}\mathrm{N} + {}^{4}_{2}\mathrm{He} \end{aligned} \tag{1.8}$$

The C and N isotopes act as catalysts during these reactions and are consumed and produced again during one complete loop of the cycle. The bottleneck of the CNO cycle is at the reaction ${}^{14}_{7}\mathrm{N} + {}^{1}_{1}\mathrm{H} \longrightarrow {}^{15}_{8}\mathrm{O} + \gamma$, i.e ${}^{14}_{7}\mathrm{N}$ is not readily destroyed by proton capture, making it the most abundant isotope to be produced during the CNO cycle (after ${}^{4}_{2}\mathrm{He}$). Thus material processed by the CNO cycle is rich in N and low in C and O. The equilibrium value (i.e the value when the production rate of the nucleus becomes equal to its destruction rate) of ${}^{14}_{7}\mathrm{N}$ in a star of solar metallicity, is 0.147 which is $\sim 98\%$ of the initial CNO mass fraction, $X_{\mathrm{CNO}} = 0.15$ (Clayton, 1983). The ${}^{12}\mathrm{C}/{}^{13}\mathrm{C}$ ratio at the end of the CNO cycle is typically $\sim$ 3.5 - 4 (Bohm-Vitense, 1992; Rose, 1998).

The conversion of H into He is the most efficient nuclear burning process in the star (Salaris & Cassisi, 2008) in terms of the energy released per reaction ($\sim$ 23.6 MeV). It is also the longest phase of burning during the evolution of a star of a given mass. Once the hydrogen in the core is exhausted, these reactions once again take place in a hydrogen-rich shell above the core, which causes the star to become a red giant. As the star ascends the RGB, its core contracts due to the weight of the helium ashes formed from H-shell burning. The next phase of burning in the core begins when $T_{\mathrm{c}} \sim$ 1-2.0$\times 10^{8}$ K (Ryan & Norton, 2010). Three He-4 nuclei (or α particles) are fused into ${}^{12}_{6}\mathrm{C}$ via the triple-α chain :

$$\begin{aligned} {}^{4}_{2}\mathrm{He} + {}^{4}_{2}\mathrm{He} &\rightleftharpoons {}^{8}_{4}\mathrm{Be} \\ {}^{8}_{4}\mathrm{Be} + {}^{4}_{2}\mathrm{He} &\longrightarrow {}^{12}_{6}\mathrm{C} + \gamma \end{aligned} \tag{1.9}$$

Once enough ${}^{12}_{6}\mathrm{C}$ has been produced it can be synthesised to ${}^{16}_{8}\mathrm{O}$ by further He-burning and when a sufficent amount of ${}^{16}_{8}\mathrm{O}$ has been produced, a further α-capture leads to the formation of ${}^{20}_{10}\mathrm{Ne}$.

$$
\begin{aligned}
{}^{12}_{6}\mathrm{C} + {}^{4}_{2}\mathrm{He} &\rightleftharpoons {}^{16}_{8}\mathrm{O} \\
{}^{16}_{8}\mathrm{O} + {}^{4}_{2}\mathrm{He} &\longrightarrow {}^{20}_{10}\mathrm{Ne} + \gamma
\end{aligned}
\tag{1.10}
$$

Further α-capture reactions leading to heavier nuclei such as magnesium-24 ($^{24}_{12}$Mg), silicon-28 ($^{28}_{16}$Si) etc., become increasingly rare because of the high coulomb barrier potential of these nuclei (Ryan & Norton, 2010). These nuclei are synthesised in other manners, which will be discussed below.

The phase of He-fusion in the core releases an energy of 7.65 MeV per reaction and is completed within a period about a 100 times shorter than the previous H-fusion phase (Salaris & Cassisi, 2008). Towards the end of exhaustion of helium in the core, He-burning begins in a shell above the core and the star once again becomes a red giant and ascends the AGB. During the AGB phase, the star also ignites an H-rich shell above the He-burning shell. During this phase, primary and secondary proton and α-capture reactions occur giving rise to O, F and Ne isotopes such as $^{18}_{8}$O, $^{19}_{9}$F and $^{22}_{10}$Ne via,

$$
\begin{aligned}
{}^{14}_{7}\mathrm{N} + {}^{4}_{2}\mathrm{He} &\longrightarrow {}^{18}_{9}\mathrm{F} \longrightarrow {}^{18}_{8}\mathrm{O} + \beta^{+} \\
{}^{15}_{7}\mathrm{N} + {}^{4}_{2}\mathrm{He} &\longrightarrow {}^{19}_{9}\mathrm{F} + \gamma \\
{}^{18}_{8}\mathrm{O} + {}^{4}_{2}\mathrm{He} &\longrightarrow {}^{22}_{10}\mathrm{Ne} + \gamma \\
{}^{19}_{9}\mathrm{F} + {}^{4}_{2}\mathrm{He} &\longrightarrow {}^{22}_{10}\mathrm{Ne} + p
\end{aligned}
\tag{1.11}
$$

If the star is a low-mass star, it would take off from the AGB when its envelope mass falls below a certain critical value (typically when ~ 10 % of its initial value is lost) by mass-loss from its surface, and turn towards hotter temperatures and eventually begin cooling and descending towards lower luminosities as a degenerate CO WD.

If a star is more massive than $8\,M_{\odot}$ (Herwig, 2005), then further core contraction results in higher temperatures which paves way for further fusion reactions to occur. The more massive a star is, the hotter its core can get and the higher number of burning phases it undergoes. For high-mass stars, after He-fusion is completed and $T_{\mathrm{c}} > 5 \times 10^{8}\,\mathrm{K}$, the next phase of burning commences, viz., that of carbon-fusion which forms isotopes of Ne, sodium(Na) and Mg (Ryan & Norton, 2010). This is followed by the photodisintegration of $^{20}_{10}$Ne ($T_{\mathrm{c}} \sim 10^{9}\,\mathrm{K}$)

where high-energy gamma-ray photons break apart the $^{20}_{10}$Ne nucleus, leading to the creation of a fresh source of $^{4}_{2}$He nuclei, and then combining with it to form $^{24}_{12}$Mg. The next phase of burning is oxygen-fusion ($T_c > 2 \times 10^9$ K) to form $^{28}_{14}$Si and $^{4}_{2}$He or alternatively, sulphur-32 ($^{32}_{16}$S). The $^{28}_{14}$Si nuclei later undergo another phase of photodisintegration ($T_c > 3 \times 10^9$ K), thus forming α-capture nuclei that include isotopes of sulphur (S), silicon (Si), argon (Ar), calcium (Ca), titanium (Ti), chromium (Cr) and finally iron (Fe).

Elements that are heavier than iron cannot be formed by further fusion reactions as the binding energy/nucleon is the highest for iron. They are formed through another process, that of neutron-capture on iron nuclei (as will be discussed in section 1.3.4).

In future sections, we shall resort to the shorter nomenclature of writing nuclear reactions. This would be in the form - $^{A_X}X(a,b)^{A_Y}Y$. For example the reaction, $^{13}_{6}\mathrm{C} + ^{1}_{1}\mathrm{H} \longrightarrow ^{14}_{7}\mathrm{N} + \gamma$ will be written as $^{13}\mathrm{C}(p,\gamma)^{14}\mathrm{N}$. Subsequently from hereon, we shall use the shorthand notation of writing a nuclear species with its atomic number only viz., ^{A_X}X.

1.3.3 Na - Ti

As discussed in section 1.3.2, Si, S, Ca and Ti are heavily produced in the nucleosynthesis of high mass stars, where temperatures are of the order of 10^9 K and are ejected in the end state of these stars namely, supernovae. In low-intermediate mass stars however, the abundances of these elements can be considerably altered by neutron and proton capture reactions.

Mg and Al isotopes are constituents of the Ne-Na-Mg-Al cycle. The four nuclear species of this cycle are formed by recurssive proton capture reactions Fig. 1.8. This reaction chain needs Ne isotopes such as ^{20}Ne and ^{22}Ne as seeds; these are produced in copious amounts during He-shell burning (as in the case of AGB stars, Eqs. 1.11– 1.12). Thus this reaction chain sets in by dropping in protons on the ashes of He-burning. Na isotopes are formed by proton captures on isotopes of Ne, the only stable one being ^{23}Na, which then undergoes another proton capture to form ^{24}Mg. ^{24}Mg further undergoes p-capture to form ^{25}Al, which being unstable, beta decays (losing a positron) to ^{25}Mg, thus forming isotopes of magnesium. ^{25}Mg further goes through another p-capture to form ^{26}Al that is unstable and decays to ^{26}Mg, which also captures a proton to form the only stable isotope of aluminium, ^{27}Al. A very small amount of ^{28}Si is formed by p-capture on ^{27}Al, but it is not very significant.

When neutrons become available, it is possible to break out from the Ne-Na-Mg-Al cycle. The abundance of ^{26}Al is increased by continuous proton capture during this cycle. But it is also a neutron poison, i.e. it is has a large cross-section of capturing neutrons within the duration of its radioactive half life. The neutron source in low mass stars is from the

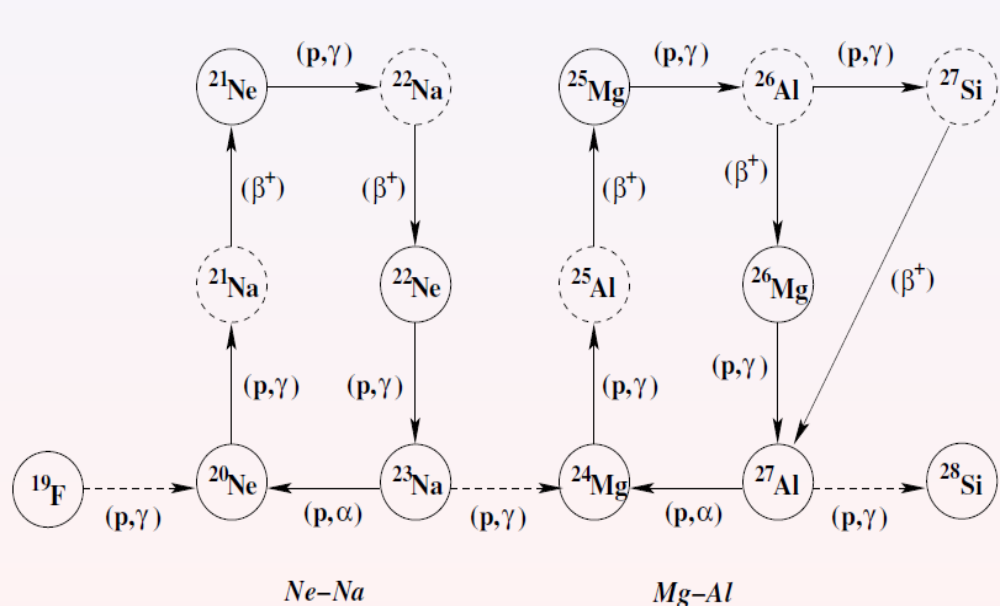

Figure 1.8: The Ne-Na-Mg-Al cycle. Figure from J. & Olofsson (2004).

He-burning of ^{13}C and/ ^{22}Ne (Eqs. 1.15) (more in section 1.3.4). The ^{26}Al is transformed to ^{26}Mg and ^{23}Na via,

$$^{26}\mathrm{Al(n,p)}^{26}\mathrm{Mg} \qquad (1.12)$$
$$^{26}\mathrm{Al(n,a)}^{23}\mathrm{Na}$$

Ca isotopes are also susceptible to n-capture reactions such as (n,g),(n,p) and (n,a), that cause an overall decrease in its abundance and produce isotopes of potassium (K) and Ti.

$$^{40}\mathrm{Ca(n,g)}^{41}\mathrm{Ca} \qquad (1.13)$$
$$^{41}\mathrm{Ca(n,p)}^{41}\mathrm{K}$$
$$^{44}\mathrm{Ca(n,g)}^{45}\mathrm{Ca}(\beta^-)^{45}\mathrm{Sc}(\beta^-)^{46}\mathrm{Ti}$$

1.3.4 Heavy elements: s-process elements

As we have seen in the previous section, for stars with an initial mass $1\,M_{\odot} \leq M \leq 8\,M_{\odot}$, fusion reactions progress beyond that of helium nuclei to carbon; with further increase in initial mass, carbon fuses to form oxygen, oxygen to silicon and silicon to iron (Fe). Fe nuclei have the highest binding energy/nucleon, which implies that the fusion of Fe nuclei is an endothermic process that needs enormous temperatures that cannot be obtained in stars. The main synthesis process to create nuclei heavier than Fe is by neutron(n)-capture on seed nuclei from the Fe-group (iron, nickel(Ni) and cobalt(Co)). Neutrons are captured by these seed nuclei and continuously assimilated until eventually an unstable nucleus, beta decays into a stable nucleus. It is through such n-capture reactions that elements heavier than iron are made in stars. There are two types of n-capture processes - the s (slow)-process and r (rapid)-process. The main distinction between these two processes is the rate at which neutrons are captured against the beta-decay rate of the unstable isotopes of the seed nuclei.

The s-process occurs in an environment where relatively low neutron densities $N_{\rm n}{\sim}10^{6} - 10^{11}$ per cm^3 (Herwig, 2005) are available. The mean period of time between two neutron captures is typically $\tau_{n\gamma}{\geq}10$ years (Iliadis, 2007). As there is a long passage of time between two consecutive neutron captures on a seed nucleus, the resulting unstable isotope undergoes a beta-decay to a higher Z stable nucleus, after just a few n-captures (Fig. 1.9). This stable nucleus also captures neutrons and progresses up the nuclear chart to higher atomic numbers, along the valley of stability Fig. 1.10. The origin of isotopes with mass, $90 < A < 204$, is majorly contributed by s-process occuring in low-mass AGB stars during their thermal pulsing phase (Herwig, 2005) and weakly by the massive AGB stars. Environments of CO+He WD mergers are also conducive to the formation of s-process elements.

The r-process needs neutron densities of the order of, $N_{\rm n}{\sim}10^{21}$ per cm^3 and has a mean neutron capture lifetime $\tau_{n\gamma}{\leq}10^{-4}$ seconds (Iliadis, 2007). The r-process nuclides are on the heavier side with $A > 130$, as the seed nuclei can undergo many n-captures before they can undergo beta-decay. Continuous and rapid n-capture occurs, and the seed nuclei progress horizontally as they grow neutron-rich until finally a heavy unstable isotope decays into a stable nucleus. It is still not very clear about the environment in which the r-process can take place. The conventional notion is that r-process occurs in the supernovae explosions of massive stars and perhaps in the core-collapse phase during the death of a super-AGB star (of initial $M > 10\,M_{\odot}$) (Herwig, 2005). CO+He WD mergers do not produce any r-process elements.

A heavy element can be formed solely out of the s-process or the r-process or with

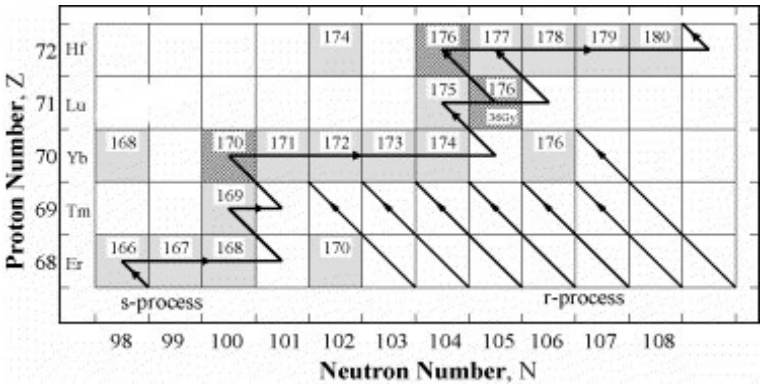

Figure 1.9: A schematic diagram of the mass region 166≤A≤180 showing the s-process path and the r-process decay chains. The s-only process nuclide ^{170}Yb is shielded from the r-process by ^{170}Er (figure from de Laeter & Bukilic (2006)).

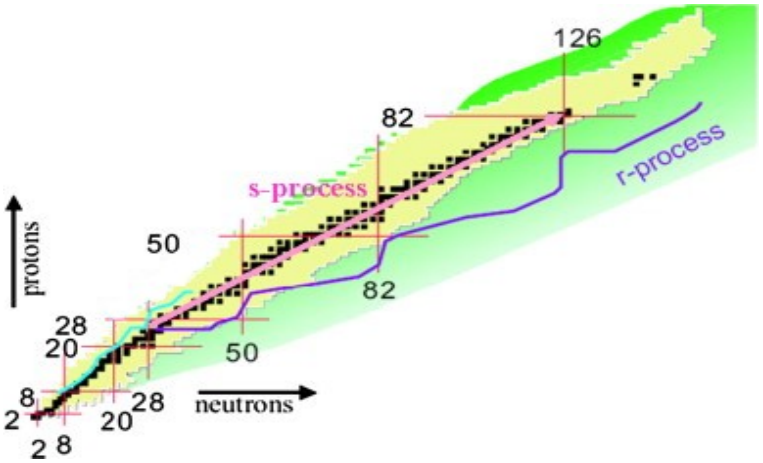

Figure 1.10: Chart of nuclei representing the different element nucleosynthesis processes. The nuclei located on the valley of beta stability are represented by the black squares (figure from Jurado et al. (2010)).

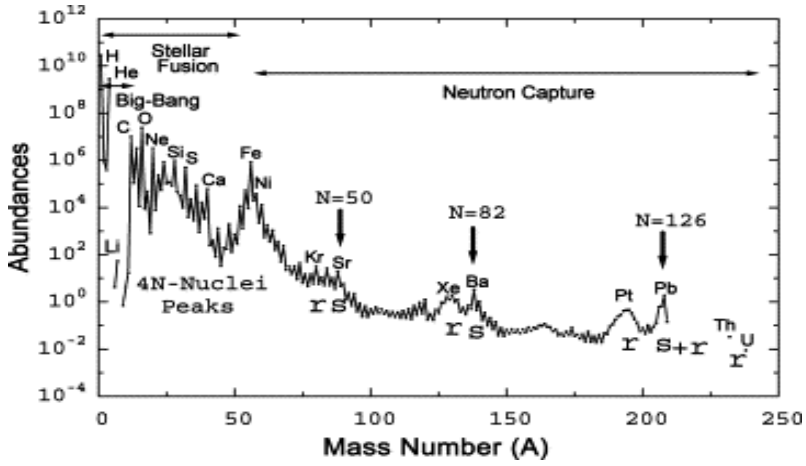

Figure 1.11: Solar-system abundances vs. mass number (A); r or s means that the corresponding peaks or shoulder are caused by the r- or s-process nuclei, respectively (figure from Igashira & Ohsaki (2004)).

contributions from both, one more dominant than the other. There are two peaks in solar abundances associated with s-process dominant elements viz., the light s-process (ls) peak of strontium (Sr), Yttrium (Y) and Zirconium (Zr) and the heavy s-process (hs) peak of barium (Ba), Lanthanium (La) and Nd (Fig. 1.11). These peak elements have small neutron-capture cross sections that prevent them from undergoing further n-capture reactions. As a result, the s-process on seed nuclei piles up at the elements in these peaks. For creating hs elements from the ls ones through the s-process, a high neutron density and a reservoir of seed nuclei are required. The hs/ls ratio indicates the efficiency of the s-process and thus the stellar environment in which these elements were created.

Since heavy nuclei are generated by the s-process in low-intermediate mass star, we shall look at the conditions for this process to occur in more detail. In the internal conditions of AGB stars, neutrons are created by α-capture reactions on ^{13}C and/ ^{22}Ne :

$$\begin{aligned} {}^{13}\mathrm{C}(\alpha, n)^{16}\mathrm{O} \\ {}^{22}\mathrm{Ne}(\alpha, n)^{25}\mathrm{Mg} \end{aligned} \tag{1.14}$$

In AGB stars of $M \leq 3\,M_{\odot}$, the He-burning shell has temperatures between $1.2 < T < 2.5{\times}10^{8}$ K. In this range of T, ^{13}C is the major source of neutrons while at higher T (in He-burning shells of AGB stars of $M > 3\,M_{\odot}$) ^{22}Ne becomes the dominant source of neutrons.

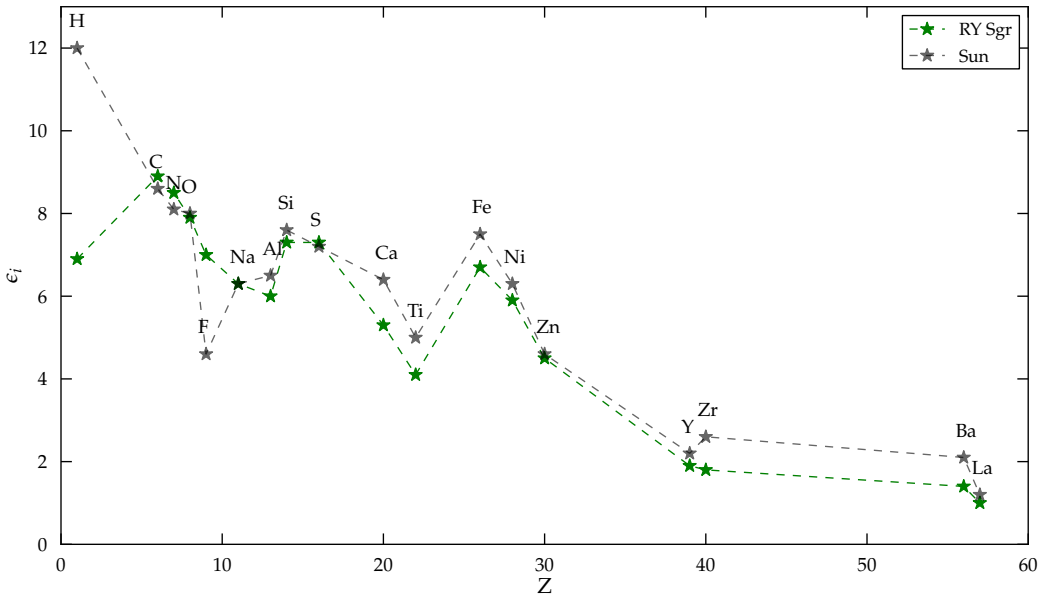

Figure 1.12: The surface composition of the RCB star RYSgr (data from Asplund et al. (2000), with uncertainities between 0.2-0.3 dex) along with that of the Sun, in terms of its absolute elemental abundance (ϵ_i) against atomic number (Z).

1.3.5 The surface composition of RCBs : from the FF or DD scenario ?

The typical composition of an RCB star is shown in Fig. 1.12. The surface of RCBs are enormously depleted in hydrogen, dominated by helium ($\sim$ 98%) and rich in carbon (C/He = 1-10 %) (Lambert & Rao, 1994; Asplund et al., 2000), nitrogen and oxygen with C>N>O. These stars have $^{12}C/^{13}C$ ratios > 40 - 100 (Hema et al., 2012) and F enhancements that are nearly 3 orders of magnitude above solar (Pandey et al., 2008). They also show considerable enhancements in s-process elements (Asplund et al., 2000) and certain characteristic trends in the abundances of elements between Na and Ti.

The RCBs, along with the HdCs, are particularly noteworthy for their extremely low $^{16}O/^{18}O$ ratios. Beginning with the discovery of this ratio being at an enormously low value of 0.83±0.02 in the HdC star, HD 137613 (Clayton et al., 2005), compared to the solar value of 500, more RCB and HdCs stars were measured to have their O-isotopic ratio to be between 1 - 20 (Clayton et al., 2007; García-Hernández et al., 2010). So far no other star in the Universe has had such a low $^{16}O/^{18}O$ value measured in them. Clayton et al.

(2005) mention the existence of other objects that have large amounts of ^{18}O, such as the circumbinary disk material of the post-AGB star, HR 4049 and the presolar graphite grains of the Murchison meteorite. However HR 4049 (not H-deficient) and the presolar grains (low ^{12}C/^{13}C ratios) are different from RCBs and HdCs in their other chemical aspects.

The hotter EHe stars have similar compositions (barring a few exceptions) to RCBs suggesting a common evolutionary origin and link. ^{18}O lines are absent from the spectra of EHes and hence one cannot know whether their ^{18}O has been depleted or are simply not detected due to their hot surfaces ($\geq$10,000K) being unable to show these lines. As one of our primary goals in this paper is to obtain the low O-isotopic ratios seen in RCB stars, we exclude EHe stars from our study. It should be noted however that EHes do have high F enhancements reported, like those in RCBs (Pandey et al., 2008).

We now analyse the above spectral characteristics of RCBs in context with the nucleosynthesis processes that occur in the FF and the DD scenarios.

From section 1.3.2, it is clear that He is formed by fusing H nuclei (thus exhausting it) and that if this fusion occurs via the CNO cycle then the material is enriched in N as well. Further fusing of He would lead to the production of C (via the triple-α process) and some of this C undergoes He burning to form O. Thus we can conclude that these stars have undergone episodes of H and He burning during their progenitor evolution or are doing so in their current evolutionary stage.

A star formed out of the FF scenario, will have a ^{12}C/^{13}C ratio closer to the CNO cycle equilbrium value (Herwig, 2001; Herwig et al., 2011), as is the case of the born-again AGB star Sakurai's object (V4334 Sgr) (Asplund et al., 1997) which has has ^{12}C/^{13}C $(1.5-5)$ much lower than what is seen in RCBs (>100). The structure of a VLTP star in which a final He- flash occurs, is very much like that of an AGB star with an H-burning shell sitting atop an He-burning shell (see section 1.2.1). ^{13}C is produced by convectively mixing protons from the envelope to the top of the He-burning shell which is rich in ^{12}C via $^{12}\mathrm{C}(\mathrm{p},\gamma)^{13}\mathrm{N}(\beta^{+})^{13}\mathrm{C}$. Sakurai's object is also enhanced in lithium in its surface, which again can be reproduced in the surface of FF stars as well (Herwig, 2001; Herwig et al., 2011).

In order to achieve the high levels of enhancements in ^{18}O (which would lead to the low ^{16}O/^{18}O ratio) and ^{19}F found in the surfaces of RCBs, partial helium burning reactions must occur on ^{14}N and ^{15}N nuclei (Eq. 1.12). The production of these nuclei should dominate over their possible destruction at higher temperatures by further α-capture to ^{22}Ne. For the efficient production of ^{18}O and ^{19}F, it is essential that the temperature be kept in the range $T = 1.2 - 1.9 \times 10^{8}\,\mathrm{K}$ (Clayton et al., 2007). The merger of two WDs in the DD

scenario are found to result in temperatures in the range of $1.23 - 2.42 \times 10^8$ K in a particular area of the merged object (Clayton et al., 2007; Staff et al., 2012). This temperature range when maintained for a certain period of time (of the order of 100 - 10,000 years) allows the production of ^{18}O to increase beyond ^{16}O, consequently bringing down the ratio of ^{16}O/^{18}O to $\simeq$ 1-10, as is wont in RCB stars. The fluorine produced in this area is also expected to be enhanced significantly above solar. At these temperatures, the ^{13}C that is present in this area is consumed by He-burning to form ^{16}O (Eq. 1.15). This destruction of ^{13}C coupled with the creation of ^{12}C via the triple-α chain leads to ^{12}C/^{13}C ratios much higher than 100 as is observed in RCBs.

In the FF model, the He-flash in the star results in temperatures as high as 3×10^8 K (Renzini, 1990; Asplund, 1999) which persisted long enough to cause the destruction of ^{18}O and ^{19}F by He-burning to ^{22}Ne (Eq. 1.12) (Herwig et al., 2011). This may explain the lack of ^{18}O (from CO bands, (Eyres et al., 1998; Geballe et al., 2002)) and F I bands (Pandey et al., 2008) detected in the spectrum of Sakurai's object.

In the DD scenario, the He-burning of ^{13}C would be the neutron source for creating s-process elements. The surface of Sakurai's object is also seen to be enhanced with s-process elements that are more pronounced compared to their levels in RCBs. ^{13}C would be the neutron source in FF stars too and it is expected that the s-process elements would form in a single neutron exposure at the time of the final He-flash (Asplund, 1999; Herwig et al., 2011).

The variations of elements between Na–Ti in RCBs and Sakurai's object, can be reasonably explained by the proton and neutron capture reactions discussed in section 1.3.3. It is however difficult to explain the overabundances of S and Si in both RCBs and Sakurai's object. From section 1.3.2, temperatures of the order of 10^9 K are needed to produce these nuclei and such temperatures do not result in either the FF or the low mass DD merger scenario.

1.4 The hypothesis: RCBs are from DD mergers

The essential spectral characteristics of RCBs such as the remarkably low O-isotopic ratio, high C-isotopic ratio and its large F enhancements can only be obtained via the merger of low-mass CO+He WDs. A few exceptions include those RCBs that are found to be richer in hydrogen compared to the majority, four RCBs in which lithium is enhanced in their surface (Asplund et al., 2000; Kipper & Klochkova, 2006) and four other RCBs that have a significant

amount of ^{13}C in their surface with their C-isotopic ratios <= 25 (Rao, 2008; Hema et al., 2012). These features are also found in the FF star Sakurai's object thus suggesting that these RCBs may have originated from an FF themselves. In terms of their physical features, such as the number of RCBs that can be produced, the timescale of recovery to maximum brightness after a dust ejection episode and the total lifetime of an RCB star, the values obtained from the DD scenario is closer in agreement than the FF scenario.

Thus from an overall perspective, the DD scenario seems to be the more probable evolutionary channel to explain both, the physical aspects and chemical compositions of RCBs. We now proceed to study the evolution of RCBs and the origin of their characteristics from the perspective of the DD scenario.

Chapter 2

Aims of this thesis

The main goal of this thesis is to perform a detailed, intensive investigation of the stellar and nucleosynthesis processes taking place in the remnant of a merger of a double degenerate CO and He WD system. Such an investigation of the nuclear yields from an evolved WD merger remnant has not been undertaken in the past.

As explained in the previous chapter, a double degenerate WD system evolves, from a gravitationally bound pair of main sequence stars. Over a period of $\sim 10^9$ years, through one or more episodes of mass-transfer events (with atleast one of them via a CE), we obtain the required compact double degenerate WD system. The orbital separation between the WDs decreases by the exchange of GWR and MSW, causing a loss of orbital angular momentum from the system. Eventually the two WDs merge, the merging process itself taking place only within $\sim 10^2 - 10^3$ seconds, with the less massive, secondary WD (in this case the He WD) being tidally disrupted by the more massive primary (the CO WD). Due to the rapid infall of the He WD during the merger, a part of the surface of the CO WD undergoes shock-heating. The final object consists of the disrupted secondary forming a radially large thick disk around the primary, which has a shock-heated surface and a cold core (Yoon et al., 2007; Lorén-Aguilar et al., 2009; Dan et al., 2012; Raskin et al., 2012).

There have been attempts made to understand the RCB surface composition from the angle of WD mergers. They were done by evolving simple homogenous stellar models (Weiss, 1987; Saio & Jeffery, 2002) in to the RCB domain of the HR diagram. However these models were not equipped to make quantitative predictions of surface nuclear abundances to be compared with those of RCBs. Clayton et al. (2007) showed through a single-zone analysis that it was possible to obtain the low O-isotopic ratios and high $^{12}C/^{13}C$ found in RCBs by keeping the likely thermodynamic conditions following a CO+He WD merger constant

for 250 - 300 years. On the other hand, analysis of Smooth Particle Hydrodynamics (SPH) simulations of merging CO and He WDs showed that it was possible to obtain the low O-isotopic ratios in the immediate merged object (after $\simeq$ 100s) (Longland et al., 2011), but not all the other chemical aspects of RCBs. Morover these simulations were performed for total masses higher than those of RCBs ($\geq 1.2 M_{\odot}$). A one-zone cold nucleosynthesis model to examine whether RCB surface abundances can result by mixing different amounts of masses from progenitors of CO and He WDs without accounting for any nucleosynthesis processes during or after the merger, was done by Jeffery et al. (2011). The nuclear abundance predictions of their models were not in complete agreement with those of RCBs. A more detailed summary of these works are presented in future chapters.

None of these investigations have been able to simultaneously obtain all the chemical signatures of RCB stars in a single, self-consistent framework. The question of whether these signatures are formed in the immediate post-dynamic merger phase or over a longer period of evolution following the merger, also remains to be solved. The aim of this thesis is to provide a robust, quantitative comparison between the nuclear abundances derived from a theoretical model to those of RCB stars. This model is a one-dimensional, nuclear abundance distribution scheme of the three-dimensional DD-merger scenario. Specifically we explore the following questions:

- What phase of the merger between the CO and He WDs can lead to the chemical composition of RCBs ? Is it : (a) The dynamic merging phase (b) A long-term evolution after the merger?
- What are the nucleosynthesis processes taking place in both (a) and (b) ?
- What is the role of the progenitor AGB and RGB stars (of the CO and He WDs respectively) in the final nuclear yields of the merged object?
- How do nuclear abundances change with respect to the parameters of the DD WD system viz., the mass-ratio between the CO and He WDs, the temperature-density (T, ρ) conditions of the merged object and the duration of these conditions.
- What kind of physical processes can occur after the merger has taken place that would affect the surface abundances of the merged object (in particular the mixing of material from the interior of the object to the surface)? Can our models place constraints on such physical processes?

There are three striking charactersitics in the surface of RCB stars - their large $^{12}C/^{13}C$ ratios, high fluorine enhancements and their extremely low $^{16}O/^{18}O$ ratio. The last characteristic is particularly noteworthy as the O-isotopic ratio of RCBs is the lowest ever observed in any star so far and is about 500 times lower than its value in the Sun. We begin our nucleosynthesis quest like (Clayton et al., 2007) by trying to look for the elusive $^{16}O/^{18}O \sim$ 1-20 found in RCBs, in a merged CO+He WD system.

The first part of this quest would be to study the nucleosynthesis that occurs during the dynamic merger of a CO and He WD system. For this purpose a 3D hydrodynamics grid code was used to simulate the merger of CO and He WD systems, with a total mass of $0.9M_{\odot}$ (simulations performed by Dr. Jan Staff at the Louisiana State University (LSU)). The merged object formed as a result of the dynamic event, was then analysed for locations in which low O-isotopic ratios could be produced. This was done by performing separate single zone nucleosynthesis calculations with the conditions of those locations and the evolution of the $^{16}O/^{18}O$ ratio was studied over the dynamic merging period of 1000 seconds. It was found that the $^{16}O/^{18}O$ ranged between $10^4 - 10^7$ in this time period, for all the hydrodynamic simulation cases. Thus, we found that the low O-isotopic ratio associated with RCB stars cannot form immediately after the CO+He WD merging phase. This in effect led to the conclusion, that RCBs are not immediate post-dynamic merger objects.

However it was found that on keeping the T, ρ conditions longer in our nucleosynthesis calculations, the $^{16}O/^{18}O$ ratio dropped to a value between 30-4 over a timescale of 10^6 - 10^9 seconds, similar to the timescale predicted by Clayton et al. (2007). This became a motivation to the next step in the quest - whether RCBs are products of a long-term evolution following the dynamic merging of CO+He WDs.

The merged object is expected to evolve into a luminous, cool giant star, with a deep convective envelope driven by internal nuclear burning (Shen et al., 2012; Schwab et al., 2012). On performing a stellar evolution calculation of the merger remnant, we find that the results are similar to the above prediction but not entirely.

In this work spherically symmetric stellar models are constructed with their internal chemical composition based on the structure of the merged object from the hydrodynamic simulations. These stellar models are allowed to evolved over a period of $\sim 10^6$ years into giants that lie in the RCB region of the HR diagram. During the evolution, we find that convection cannot be the dominant mixing mechanism in these stars and an extra mixing component, perhaps induced by the rotation of the merger remnant, becomes necessary. Once the stellar evolution simulation is complete, we perform a complete, multizone nucle-

osynthesis analysis of the stellar evolution tracks and compare the surface compositions of our models with those of RCBs. Such a detailed long-term nucleosynthesis behaviour of a merged WD system has not been performed in the past.

Depending on the initial conditions of our models, we obtain a range of surface nuclear yields. On comparing these yields with those of RCBs, we find that our models are successful in recreating the surface abundance patterns of RCB stars. Our main objective of obtaining the three essential chemical characteristics is met; amongst the models computed, we achieve O-isotopic ratios between 9 - 15, C-isotopic ratios above 100 and fluorine enhancements between $\sim$ 1.4 - 2.3 dex (1 dex is an order of magnitude) compared to solar. Along with these we are also successful in obtaining the s-process enrichments of RCBs along with the abundances of the other secondary elements between Na-Ti.

Thus, our main goal of the question of whether RCBs are formed from the merger of CO and He WDs is answered with robust results that show that RCBs are formed during the long stellar evolution phase following the merger event. Aside from achieving the main goal of the thesis, we also find important constraints on the long term behaviour of a merged system, in terms of the duration of the immediate post-dynamic merger conditions and on the mixing that occurs during the stellar evolution phase. The following chapters entail these results in more detail. We begin with the results of the nucleosynthesis in the dynamic merging phase of the CO and He WDs.

Chapter 3

RCBs - Products of dynamic merger phase of WDs ?

3.1 Introduction

In this chapter, we investigate whether the strikingly low O-isotopic ratio of RCBs of the order of 1-10 can be obtained in the dynamic merger phase of low-mass CO and He WDs. Previous simulations have been performed for mergers larger than the mass of RCB stars, viz., with a total mass of $> 1M_{\odot}$. The hydrodynamic simulations from which the thermodynamic conditions of the merging phase of the CO and He WDs are extracted for the nucleosynthesis calculations, are performed for a total mass of $0.9M_{\odot}$, over a range of mass-ratios.

The work in this chapter is published in the paper, Staff, J., Menon A., et al., 2012, ApJ, 757, 76S. Three-dimensional hydrodynamic simulations of the merger were performed (by Dr. J. Staff, LSU) for pairs of degenerate low-mass CO and He WDs. The final merged object from the simulations, was examined for locations that were suitable to produce a sufficient quantity of ^{18}O to compete with the amount of ^{16}O present there. Additionally we also assess the ^{19}F abundance in those regions and their ^{12}C/^{13}C ratios. The T, ρ, and nuclear abundances of these locations were then fed as inputs to a nucleosynthesis code (NuGrid, (Herwig et al., 2008)), which was run over a suitable period of time. The evolution over this time period of various nuclear species that affect the O-isotopic ratio were studied and the value of this ratio at each timestep of evolution were compared to its observed value in RCB stars.

In section 3.1, the results of the hydrodynamic simulations are summarised. Section 3.2 includes a description of the nucleosynthesis code used, the construction of a likely progenitor

evolution scenario and the initial nucleosynthesis models. In Section 3.3 we present the results of the nucleosynthesis calculations and finally in section 3.4 a summary of the results is put forth, followed by its discussion and directives to the next steps.

3.2 Dynamic merger of WDs: Results of hydrodynamic simulations

The hydrodynamic grid code 'Flower' (Motl et al., 2002) was used to perform the merger of a system of degenerate CO and He WDs, over a range of mass-ratios $q = 0.5 - 0.99$, where q stands for the ratio between the mass of the less massive donor ($M_{\rm He\,WD}$) to that of the accretor ($M_{\rm CO\,WD}$), $q = M_{\rm He\,WD}/M_{\rm CO\,WD}$ and having a fixed total mass of $0.9 M_{\odot}$. The fluid of the CO WD in the simulations was composed of 50% C and 50% O while that of the He WD was pure He. As Flower did not have a nuclear network built in to it, the hydrodynamic simulations could not account for nuclear burning processes that may have occured in the merger.

During the course of the merger between the CO (accretor) and He WD (donor) in the hydrodynamic simulations, the donor is tidally disrupted by the more massive accretor. The initially cold donor material falls onto the cold accretor and causes the accretor to be heated through shocks or adiabatic compression and leads to a very hot and dense region surrounding the accretor, labelled as the 'Shell of Fire' (SOF). Such an SOF is a common feature in simulations of this kind (see for instance Yoon et al., 2007; Lorén-Aguilar et al., 2009; Raskin et al., 2012). Beneath the SOF is the cold core of the accretor while above it is a nearly cold envelope containing primarily the He-rich material of the donor (Fig. 3.1). Amongst the simulations performed, only those cases with $q \lesssim 0.7$ show a sustained SOF around the merged core, where q stands for the ratio between the mass of the donor ($M_{\rm He\,WD}$) and the accretor ($M_{\rm CO\,WD}$). The SOF is the region with the hottest temperature and highest density above the cold CO core and unlike the high-q cases, it is found to last until the very end of the simulation . Thus the SOF is identified as the location that is hot enough to perform nucleosynthesis in the merged object and hence we focus our attention on the low-q cases [1].

In the merging phase of the two WDs in the low-q cases, a large amount of accretor

[1]Movies of all the simulations showing density, temperature,and mass ratios in the equatorial plane can be found here:
`http://phys.lsu.edu/~Astroshare/WD/index.html`

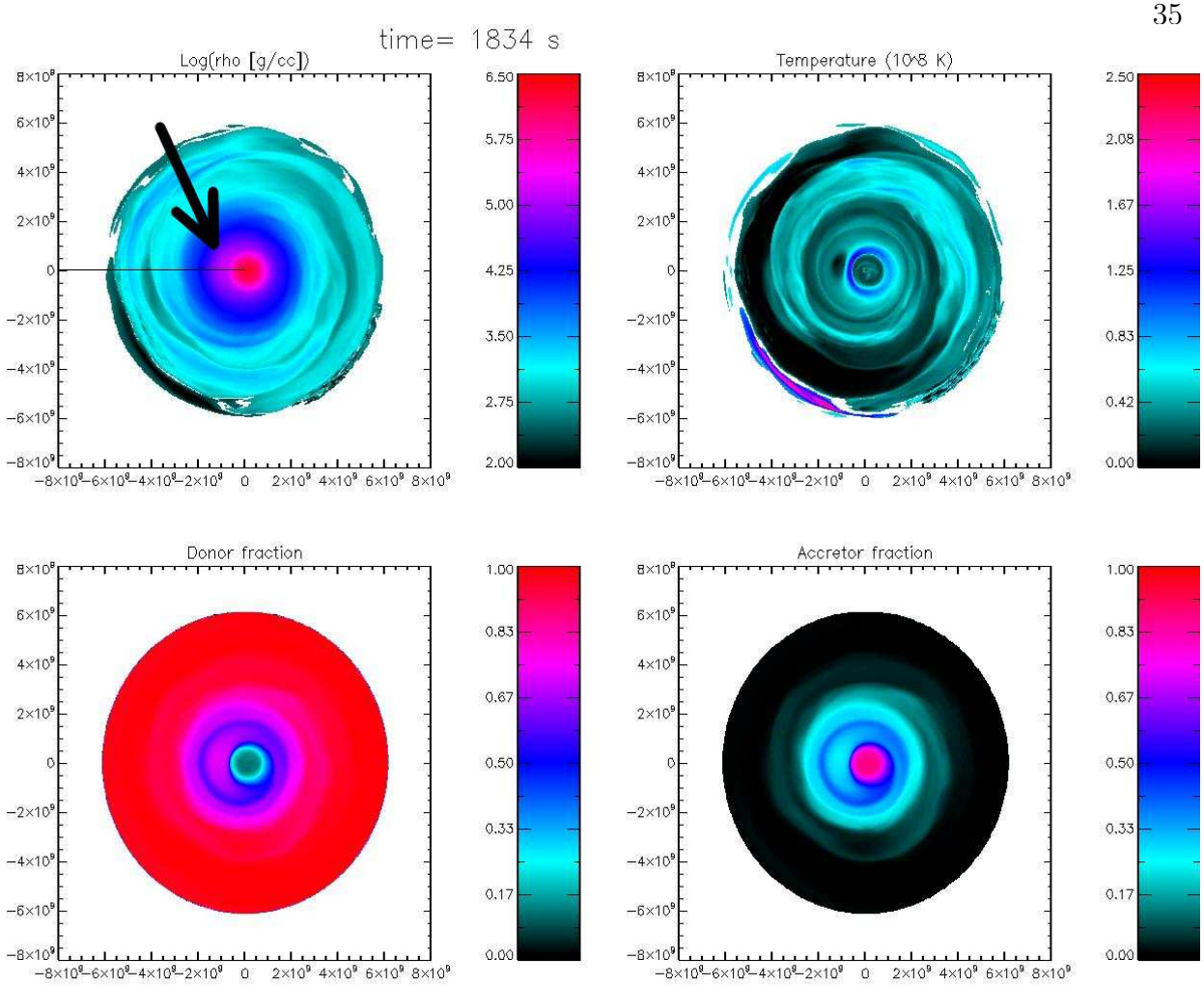

Figure 3.1: The $q = 0.7$ simulation after the two stars have merged, showing log density (upper left), temperature (upper right), mass fraction of donor material (lower left), and mass fraction of accretor material (lower right) in the equatorial (r-ϕ) plane. A hot SOF (indicated by the black arrow in the log density plot) forms around the merged core with temperatures $\sim 1.5 \times 10^8$ K (assuming C and O only)).

material is dredged up and mixes with the incoming donor material. The SOF is formed in this layer of mixed donor and accretor material and thus has contributions from both in its nuclear makeup (Table 3.1). It has temperatures of the order of $\sim 10^8$K (hot enough to burn He) and densities of the order of $10^4\,\mathrm{gcm}^{-3}$ (Table 3.2). The SOF (in all low q cases) if seen to be located just outside the merged core ($r \sim 10^9$ cm), with a thickness of about $1 - 2 \times 10^8\,\mathrm{cm}$ (Table 3.2). The core of the merged object is defined to be the region where $\rho > 1.58 \times 10^5 \mathrm{gcm}^{-3}$ and $T < 10^8\,\mathrm{K}$, while the SOF is defined as the region where

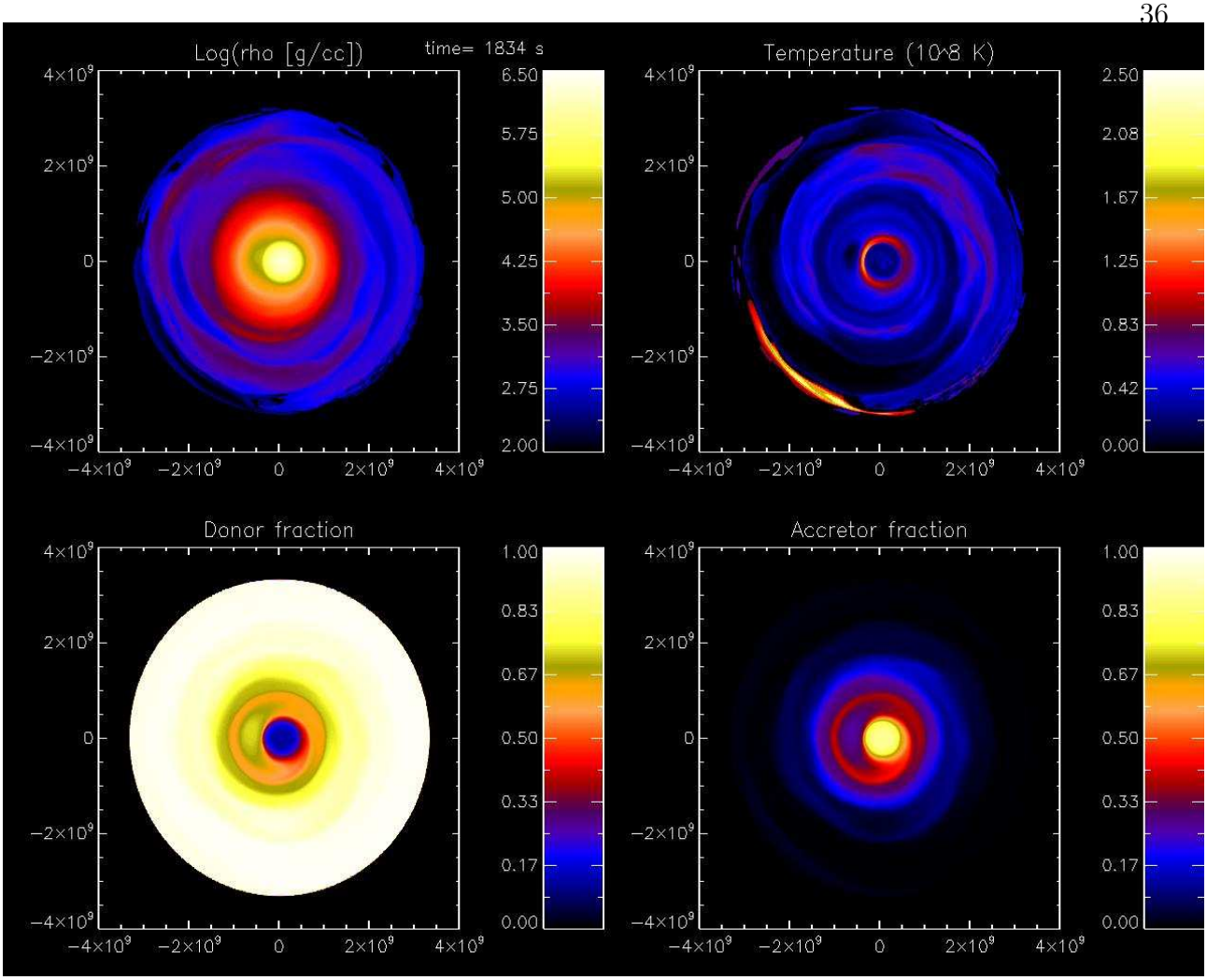

Figure 3.2: Same as Fig. 3.1 but with a different colour scheme.

$\rho > 1.78 \times 10^4 \mathrm{gcm}^-3$ and $T > 10^8$ K. The temperatures deduced from the hydrodynamic simulations were based on a composition of equal amounts of C and O. These temperatures were found to be lower by a factor of $\sim$ 1.5 on including the He content of the SOF, which are the values reported in Table 3.2. Table 3.3 lists the details of important parameters of the low-q cases.

3.3 Initial nucleosynthesis models

In order to perform nucleosynthesis calculations, we use the temperature and density conditions of the SOFs. After the merging of the WDs, the SOFs are seen as a feature solely

Table 3.1: For each of the low-q simulations, the fraction of mass ($f_{\rm acc-dredged}$) dredged up from the accretor, the accretor mass in the SOF ($m_{\rm acc-SOF}/M_\odot$) and the accretor mass that is outside the SOF in the envelope ($m_{\rm acc-out}/M_\odot$).

q	$f_{\rm acc-dredged}$	$m_{\rm acc-SOF}/M_\odot$	$m_{\rm acc-out}/M_\odot$
0.5	0.17	0.08	0.02
0.6	0.18	0.07	0.03
0.7	0.15	0.05	0.03

Table 3.2: Summary of the conditions found in the SOF after the merger. In particular, q is the mass ratio used in the hydrodynamic simulations, $T_{\rm SOF}$ and $\rho_{\rm SOF}$ are representative values of density and temperature in the SOF, $f_{\rm acc-SOF}$ represents the fraction of the SOF made of the accretor material and $dR_{\rm SOF}$ refers to the (approximate) width of the SOF.

q	$T_{\rm SOF}$ (10^6 K)	$\rho_{\rm SOF}$ (10^4 gcm^{-3})	$f_{\rm acc-SOF}$	$dR_{\rm SOF}$(10^9 cm)
0.5	242	3.16	0.67	0.2
0.6	210	3.16	0.54	0.15
0.7	123	5.01	0.50	0.2

Table 3.3: Details of the low-q simulations - mass of the accretor CO WD ($M_{\rm CO\,WD}/M_\odot$), mass of the donor He WD ($M_{\rm He\,WD}/M_\odot$), mass of the SOF ($M_{\rm SOF}/M_\odot$), the mass that is present above the SOF in the envelope ($M_{\rm env}/M_\odot$), the time from the beginning of the simulation to the end of the merger ($t_{\rm merge}$ (s)), the total time for which the simulation was run ($t_{\rm end}$ (s)) and the time for which the simulation was run after the merger ($\delta t = t_{\rm end} - t_{\rm merge}$ (s)).

q	$M_{\rm CO\,WD}/M_\odot$	$M_{\rm He\,WD}/M_\odot$	$M_{\rm SOF}/M_\odot$	$M_{\rm env}/M_\odot$	$t_{\rm merge}$ (s)	$t_{\rm end}$ (s)	δt (s)
0.5	0.6	0.30	0.12	0.24	2070	2542	472
0.6	0.56	0.34	0.13	0.26	1150	1500	350
0.7	0.53	0.37	0.10	0.30	1200	1970	570

of the low q cases, with temperatures ranging from 1.23×10^8 to 2.42×10^8 K with densities between $\rho = 1.78 \times 10^4 - 1.58 \times 10^5$ g/cm^{-3} (Table 3.2) and contain material from both the accretor and the donor (Table 3.1). If the low O-isotopic ratios of RCBs originate in the dynamic merger-phase, then it would be in the SOF that we would expect this to be formed. We first briefly discuss the codes used in our calculations.

3.3.1 Nucleosynthesis code : NuGrid

We perform single zone nucleosynthesis calculations of the SOF region, using the single zone post-processing network (**SPPN**) code from the **NuGrid** project (Herwig et al., 2008). Its core unit is a nuclear network kernel, containing nuclear reactions, reaction rates and a solver

package, which evolves the nuclear network over each time step. For our purposes, we use a database of 1095 isotopes. The nuclear network kernel accordingly adjusts its size to span over the reactions involving these isotopes. **SPPN** requires the following inputs - T, ρ, the initial abundance distribution of the nuclei, the time period over which the network has to be calculated and limits on the size of the time step. On running the code over a specific period of time at constant T and ρ, we get a distribution of nuclear abundances as the output.

3.3.2 Construction of initial models for nucleosynthesis

Our first step in the construction of the initial nuclear distribution for each low-q case is to obtain CO and He WD abundance profiles. In order to do this, we need to construct a likely progenitor binary evolution scenario, that would form a double degenerate WD system. Once the CO and He WD nuclear profiles are determined, we then use the information in Table 3.1 to build the initial abundances of the SOF of each q case.

R Coronae Borealis progenitor systems

The abundance profiles of the WDs are extracted from fully post-processed, solar metallicity, models (NuGrid SEE library, Set 1.2 models for solar metallicity, Pignatari et al. in preparation) of realistic 1D stellar evolution tracks computed using the stellar evolution code MESA (Paxton et al., 2011).

In order to determine the initial abundance contribution from the CO WD, the evolutionary state of the AGB progenitor from the last common envelope (CE) phase has to be determined. During the likely binary progenitor evolution that leads to the double degenerate merger considered here (section 1.2.1), one or more CE phases can occur. For the scenario that we consider, there are two CE phases. The first one occurs when the primary MS star evolves to an AGB and overflows its Roche lobe, thus forming a system of a CO WD and the companion MS secondary star in a closer orbit. During the second CE event, the secondary star evolves to an RGB and undergoes RLOF, at the end of which we are left with a CO+He WD system. For a star to fill its Roche lobe, its radius must be greater than or equal to its Roche lobe radius ($R_{\rm L}$). $R_{\rm L}$ is the product of a function of the mass ratio $E(q)$ (Eq. 1.1) between the primary and the secondary components of the binary system and the separation (A) between them, given by $R_{\rm L} = E(q)A$. From observations of binary systems, the separation between components can range between $3 - 10^4 R_{\odot}$ (Hurley et al., 2002), which implies that the $R_{\rm L}$ of a star in a binary system, with a given initial mass ratio,

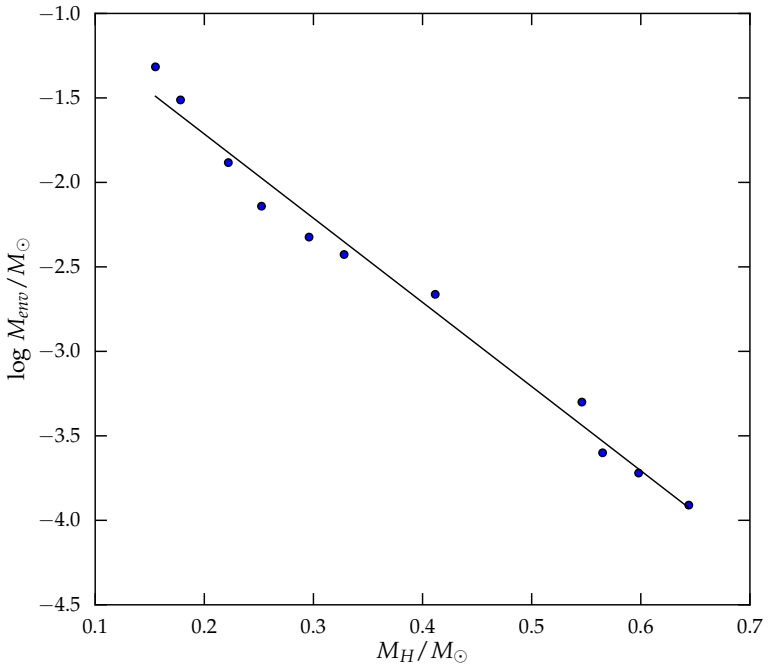

Figure 3.3: Plot showing the anti-correlation between envelope mass (log $M_{\rm env\,WD}/M_\odot$) and hydrogen-free core mass ($M_{\rm H}/M_\odot$). A best fit line using the least squares method is drawn through the blue data points.

can vary over 4 orders of magnitude depending on the separation distance between the two components.

From stellar evolution studies, the structure of a WD consists of a hydrogen-free core, $M_{\rm H}$, surrounded by a thin envelope of unprocessed material which is rich in hydrogen. The envelope mass ($M_{\rm env\,WD}$) is typically between 0.05 to 1% of the mass of the WD and is anti-correlated with $M_{\rm H}$, whose the outer boundary is the mass co-ordinate at which the hydrogen abundance $X_{\rm H} = 0.37$ (Schönberner, 1983). Using the data from the work of Schönberner (1983) for CO WDs and Driebe et al. (1998) for He WDs, a least squares fit is done between $M_{\rm H}$ and $M_{\rm env\,WD}$. The best fit line thus constructed enables us to read off $M_{\rm env\,WD}$, for a particular $M_{\rm H}$ (between 0.1552 and 0.644 $M_\odot$) (Fig. 3.3). The analytic equation of this line is $\log(M_{\rm env\,WD}/M_\odot) = -4.982\,M_{\rm H}/M_\odot - 0.7171$. The low-$q$ hydrodynamic simulations, use a range of masses of CO WDs ($M_{\rm CO\,WD}$) between 0.53 and 0.6 $M_\odot$. For the purposes of the following explanation, we can take $M_{\rm CO\,WD} = M_{\rm H}$ since the envelope mass, $M_{\rm env\,WD}$ of the CO WD is less than 0.1% of its total mass, $M_{\rm CO\,WD}$ (Fig. 3.3).

However, the white dwarf mass ($M_{\rm WD}$) alone does not directly point to the initial mass

of its progenitor star. Fig. 3.4 shows the evolution of $M_{\rm H}$ ($\simeq M_{\rm WD}$) for a range of stellar masses (1.65, 2 and 3 $M_{\odot}$). It is evident that for a given value of $M_{\rm H}$ the star could have any of the three initial masses and lie anywhere between the early AGB (E-AGB) phase and an advanced thermal pulsing (A-TP) phase. The higher the number of TPs that the star has undergone, the more enriched it is in partial He-burning and s-process products (Herwig, 2005). A parameter that will help in solving this degeneracy between the initial mass and $M_{\rm WD}$, is the $R_{\rm L}$ of the progenitor giant star.

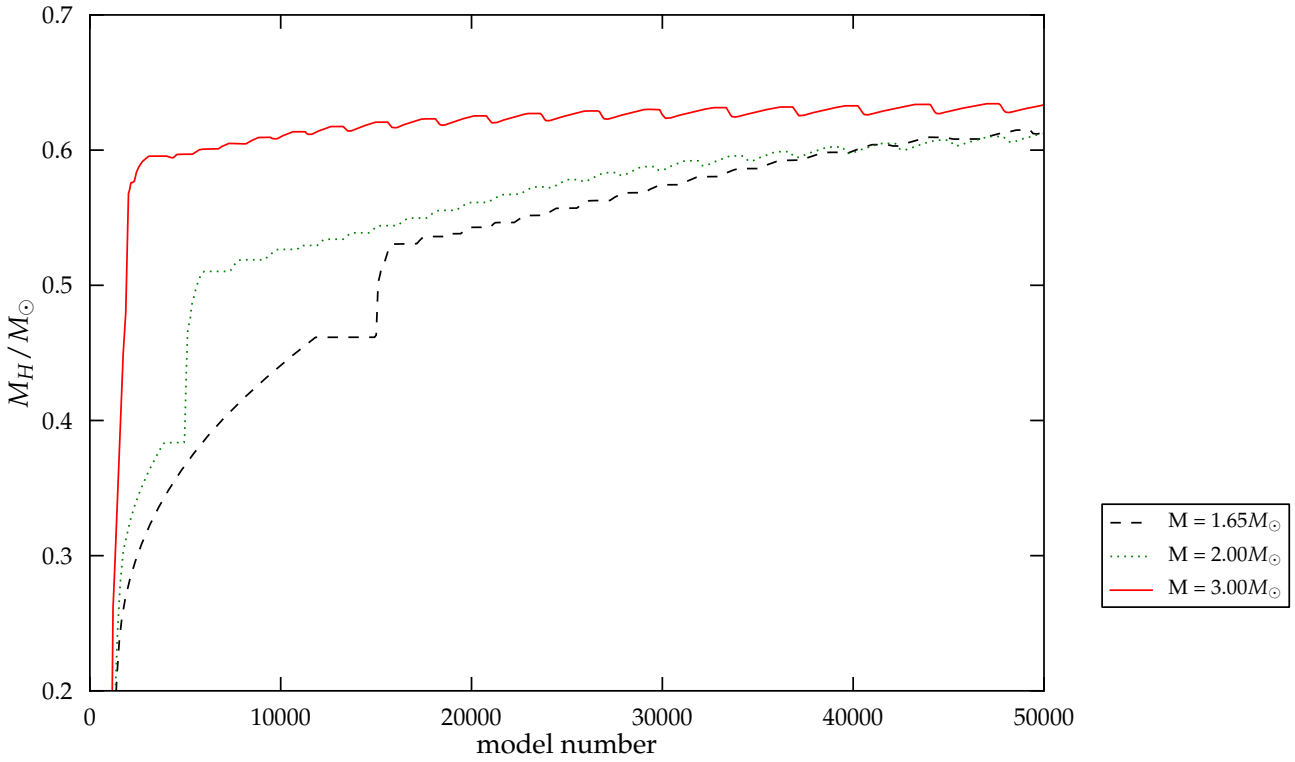

Figure 3.4: The evolution of the H-free core mass ($M_{\rm H}/M_{\odot}$) during the AGB phase of the star, for three initial masses. The model numbers on the horizontal axis are related to time, with a higher model number being a later time. The AGB thermal pulse phase occurs over a much smaller time period than the previous evolution of the star. Hence, if age were used as the x axis parameter, the thermal pulse features would be compressed and not visible. Model numbers help in visualising the entire range of evolution of the star.

To construct a likely progenitor evolution scenario, we work backwards from the second CE event that formed the He WD in the DD system. Let us consider an He WD model from the cases plotted, whose mass is nearly the same as the one in the $q = 0.5$ simulation.

This model has mass $M_{\rm He\,WD} = 0.3024 M_{\odot}$ from an RGB star of 1.65 $M_{\odot}$, which has a radius, log $R_{\rm RGB}/R_{\odot} = 1.286$. If we assume that the RGB star in the binary system fills its Roche-lobe at this particular radius, i.e log $R_{\rm L}/R_{\odot} = 1.286$, then a dynamically unstable RLOF of the RGB would lead to the second CE event. Let us assume, that the separation between the companion MS and the donor RGB, A_2, is the $R_{\rm L}$ of the RGB, i.e log $A_2/R_{\odot} =$ log $R_{\rm RGB}/R_{\odot} = 1.286$.

From the hydrodynamic simulation work on CE events of red giants by **?**, we know that the separation between the components reduces by at least 4.5 times its initial separation, after a CE event. We assume that the occurence first CE event immediately leads to the separation before the onset of the second CE event viz., log $A_2/R_{\odot} = 1.286$. Hence, the minimum separation between the primary AGB star and the MS secondary, that led to the first CE event was log $\rm A_1/R_{\odot} = 4.5 \times$ log $A_2/R_{\odot} = 1.93$. Once again, we assume that the $R_{\rm L}$ of the giant (the AGB in this case), is equal to the separation between the two components before the CE event viz., log $R_{\rm AGB}/R_{\odot} =$ log $A_1/R_{\odot} = 1.93$. Since A_1 is the minimum separation between the AGB star and the secondary MS, we consider models of AGBs which have log $R_{\rm AGB} \geq 1.93$ (Fig. 3.5). In this respect, we choose to investigate three specific cases representing different phases of the AGB evolution, from our choice of initial masses. These are, during the early AGB phase (CO WD(1), an early TP phase (CO WD(2)), and a late TP phase (CO WD(3)) (after the star becomes carbon rich in its surface). Table 3.4 summarizes the relevant parameters of these CO WD models. It must be pointed out that the post CE WD abundance profile is assumed to be that of the inner portion of the progenitor AGB models considered here. Henceforth the CO WD models are to be understood as the progenitor AGB stars with mass equal to $M_{\rm CO\,WD} = M_{\rm H} + M_{\rm env\,WD}$.

It must be noted that while the star is in the TP phase the chosen model must be at the peak of the pulse, since the radius of the star is at its maximum during the peak of a given pulse. If the star has not been able to fill its Roche lobe during an earlier pulse peak, it cannot do so until it hits the next pulse peak.

Table 3.4: The details of the CO WD models - initial mass ($M_{\star}$), model number, phase of evolution, mass of the CO WD ($M_{\rm CO\,WD}/M_{\odot}$), mass of H-free core ($M_{\rm H}/M_{\odot}$), and log $\rm R/R_{\odot}$.

Serial number	$M_{\star}$	model number	phase of evolution	$M_{\rm H}/M_{\odot}$	$M_{\rm CO\,WD}/M_{\odot}$	log $\rm R/R_{\odot}$
1	3	2364	E-AGB	0.58123	0.58148	1.97
2	2	12198	3rd TP	0.53334	0.53376	2.35
3	2	49901	21st TP	0.61226	0.612243	2.65

From the hydrodynamic simulations it is seen that the He WD is totally disrupted and

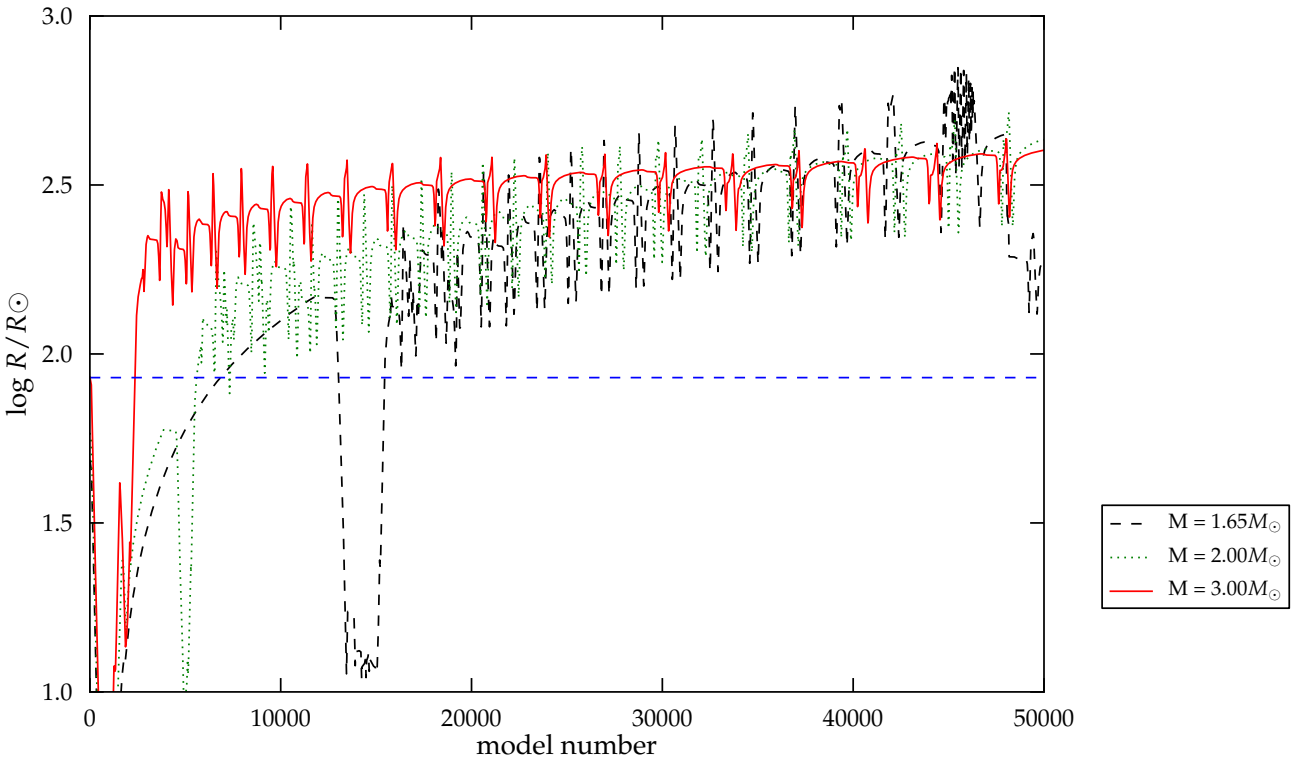

Figure 3.5: The variation of the radius of the star (log $R/R_\odot$) plotted against the model number, during the AGB phase of the star, for three initial masses. The blue dashed line is the minimum AGB radius, log $R_{AGB}/R_\odot = 1.93$ required for the first CE event. A model number corresponds to every step in time taken by the code during the run for each initial mass; a higher model number corresponds to at a later point of time.

well mixed during the final merging phase. Hence for the He WD the nuclear abundances are averaged over its entire mass, thus giving a uniform composition for the He WD. From Table 3.1, the fraction of CO WD dredged up outside is less than 20%. Table 3.5 contains the isotopic abundances of the He WD and the cumulative abundances of significant elements in the outer 20% of the CO WD models.

Initial abundances of the SOF

In order to achieve an extremely low $^{16}O/^{18}O$ ratio such as that observed in RCB stars, we take the CO WD model which provides the abundances most viable to help realize this. The model which has the highest amount of ^{14}N and ^{18}O and the least amount of ^{16}O,

Table 3.5: The averaged (approximate) abundances (%) by mass, for dominant and relevant species for the evolution of the abundance of ^{18}O in the outer part of the three CO WDs are presented in Table 3.4 (we considered the most external zone, which corresponds to about 20% of the total WD masses). The other species in the nuclear network of the code, are present in much smaller proportions.

Species	He WD	CO WD(1)	CO WD(2)	CO WD(3)
^{1}H	1.51	0.33	0.276	0.093
^{4}He	96.5	41.7	14.6	9.04
^{12}C	0.011	36.5	50.5	43.9
^{14}N	1.3	0.43	0.061	0.155
^{16}O	0.074	19.0	32.0	43.8
^{18}O	2.86×10^{-5}	2.7×10^{-3}	2.71×10^{-4}	1.11×10^{-5}
^{22}Ne	2.73×10^{-4}	1.34	1.95	2.18

amongst the three cases is selected. This model belongs to the early AGB phase of the 3 $M_{\odot}$ star , (Fig. 3.6) and has $M_{\rm CO\,WD}$=0.58148 $M_{\odot}$ (CO WD(1), Table 3.4) and an envelope of $2.5 \times 10^{-4} M_{\odot}$. It must be noted that since the progenitor of the CO WD model chosen is on the E-AGB, it does not have any s-process element enhancement on its surface. Hence the production of s-process elements, if any, will have to take place in the merger itself. Investigating s-process signatures however is beyond the scope of the aims of this study.

Thus by using the CO WD (accretor) and He WD (donor) models described above and the knowledge of the fraction of the SOF made of the accretor ($f_{\rm acc-SOF}$) and the donor (1-$f_{\rm acc-SOF}$, Table 3.2), the initial abundances of the SOF are constructed (Table 3.6). We assume that all the material from the CO WD has been dredged up from its outer layers, before the onset of hot nucleosynthesis in the SOF.

Table 3.6: The averaged initial abundances (%) for dominant and relevant species for the evolution of the abundance of ^{18}O in the SOF of the $q = 0.5$, 0.6, and 0.7 cases using the He WD and CO WD(1) models of Table 3.5. The other species in the nuclear network of the code, are present in much smaller proportions.

Species	SOF,0.5	SOF,0.6	SOF,0.7
^{1}H	0.75	0.89	0.97
^{4}He	64.8	69.5	75.9
^{12}C	22.2	18.6	15.1
^{14}N	0.76	0.85	0.92
^{16}O	10.03	8.9	5.9
^{18}O	0.021	0.016	0.018
^{22}Ne	0.81	0.68	0.55

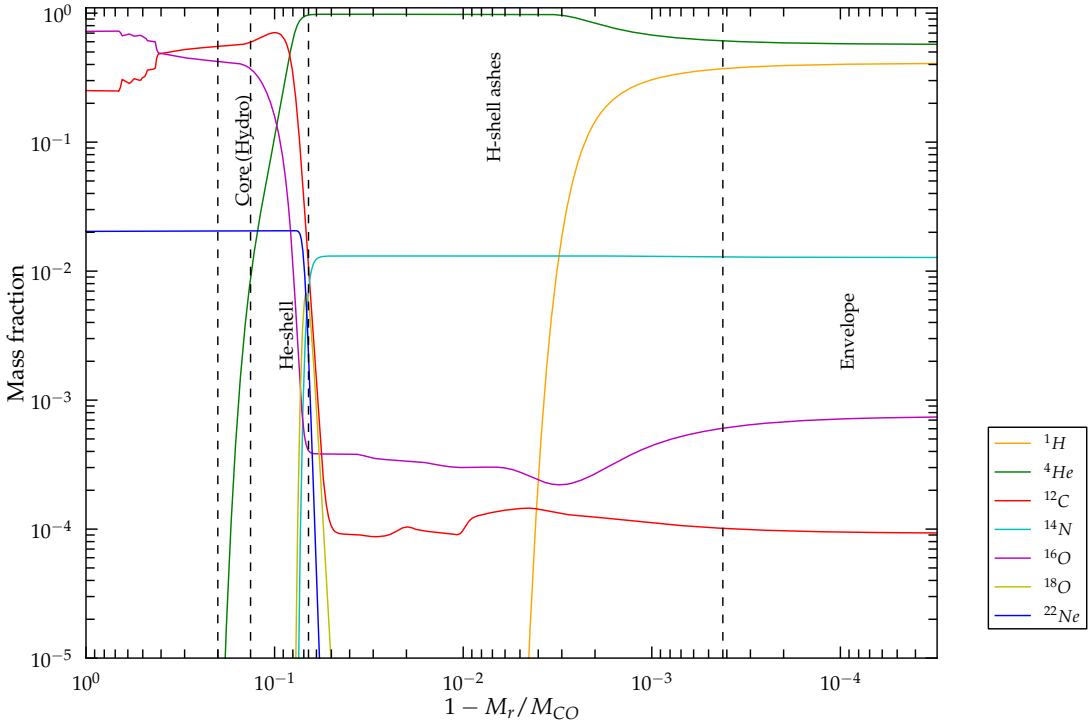

Figure 3.6: Nuclear abundance profile of the CO WD(1) model. The x-axis is $(1 - M_r/M_{\mathrm{CO\,WD}})$ where M_r is the radial mass co-ordinate and $M_{\mathrm{CO\,WD}} = 0.58148\,M_\odot$. The zones of the CO WD are labelled and marked with dashed black lines. The lower limit on the zone marked "Core (hydro)" is placed at a depth enclosing 20% of the $M_{\mathrm{CO\,WD}}$ mass, which is the upper limit on the mass dredged up of the CO WD as seen in the hydrodynamic simulations.

3.4 Nucleosynthesis in the SOF

The SOF is present until the end of the simulations for all three low-q cases, the duration of its existence is unclear. Therefore, we run the nucleosynthesis simulations until the abundance of ^{18}O begins to drop significantly. The ^{18}O abundance drops to 10^{-8} at $\sim 10^{7}$ seconds from the beginning of the nucleosynthesis calculation in the $q = 0.5$ case. We take this time period for the other two low-q cases as well and run the nucleosynthesis network at the appropriate constant temperature and density (Table 3.2).

In order to compare with observations, the abundances of all unstable elements are instantaneously decayed. These abundances are plotted in Figs. 3.7, 3.8, and 3.9, for $q = 0.5$, 0.6, and 0.7. Since the densities in the SOF are similar amongst the low-q cases, the differ-

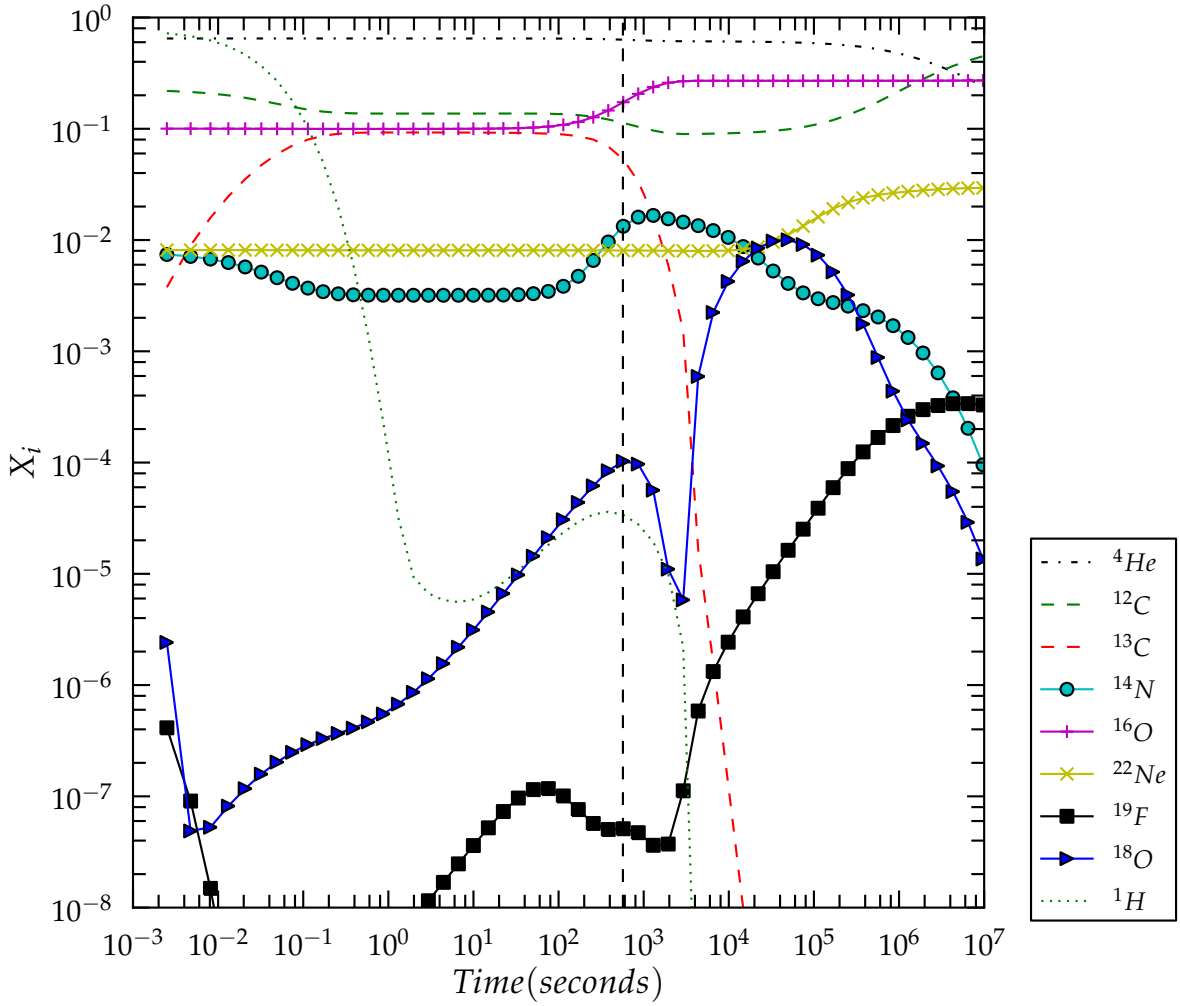

Figure 3.7: Evolution of the mass fraction (X_i) of nuclear species when starting with conditions similar to those found in the SOF in the $q = 0.5$ simulation with $T = 2.42 \times 10^8\,K$ and $\rho = 3.16 \times 10^4\,\mathrm{gcm}^-3$ over a period of 10^6 seconds. The hydrogen abundance is multiplied by a factor of 10^2. The dashed vertical line corresponds to δt (Table 3.3).

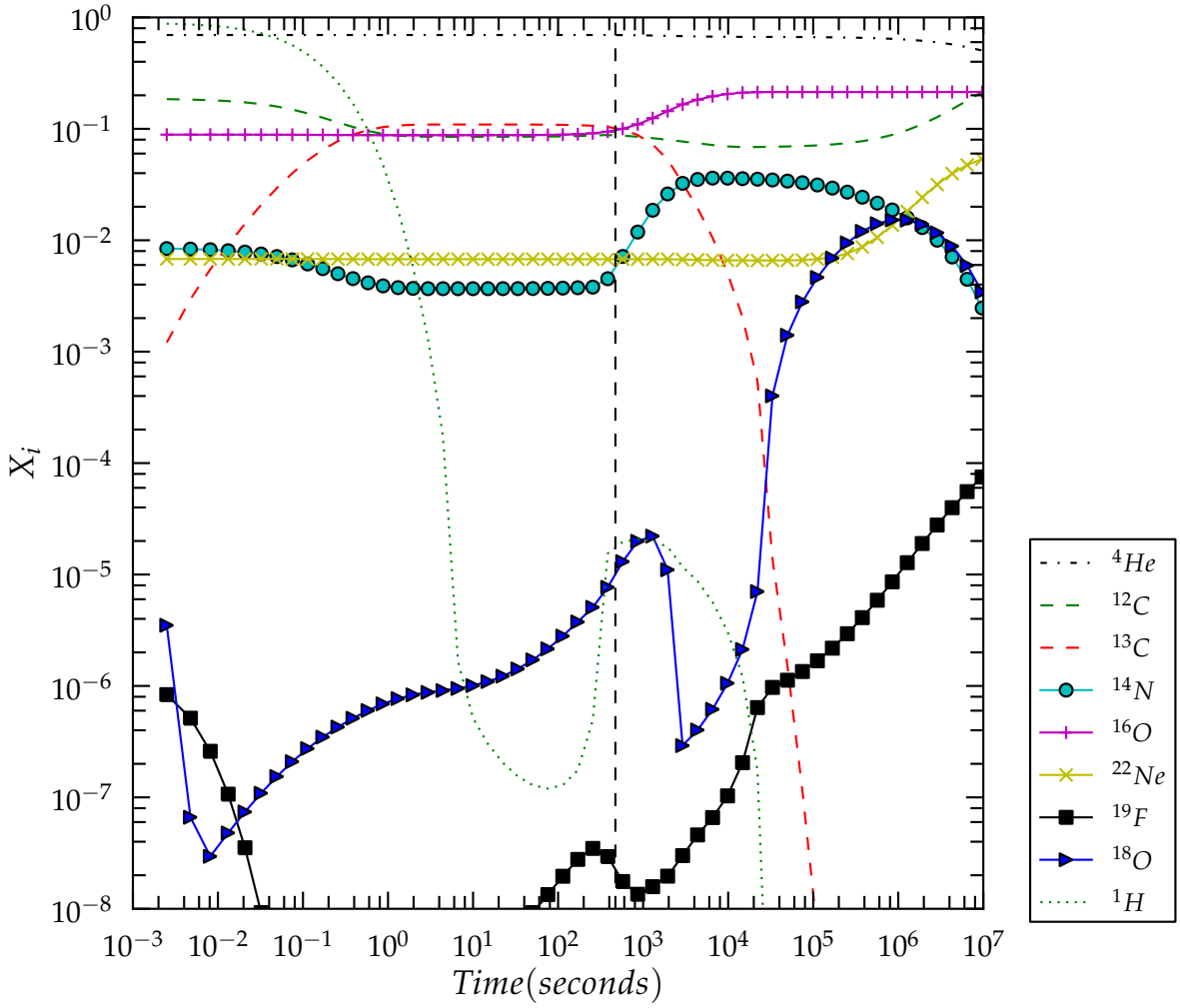

Figure 3.8: Evolution of the mass fraction (X_i) of nuclear species when starting with conditions similar to those found in the SOF in the $q = 0.6$ simulation at $T = 2.1 \times 10^8$ K and $\rho = 3.16 \times 10^4\,\mathrm{gcm}^-3$ over a period of 10^6 seconds. The hydrogen abundance is multiplied by a factor of 10^2. The dashed vertical line corresponds to δt (Table 3.3).

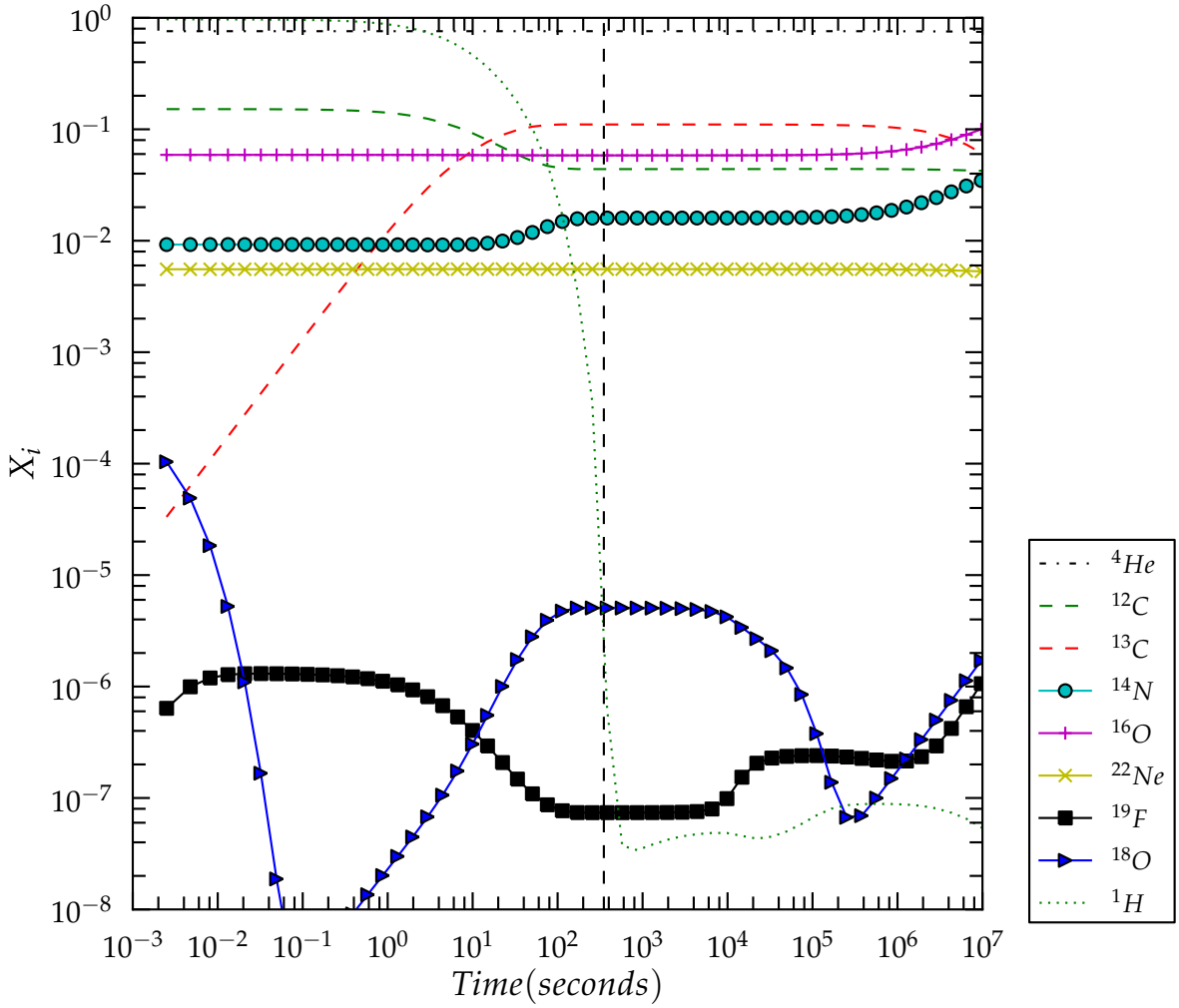

Figure 3.9: Evolution of the mass fraction (X_i) of nuclear species when starting with conditions similar to those found in the SOF in the $q = 0.7$ simulation at $T = 1.23 \times 10^8$ K and $\rho = 5.01 \times 10^4\,\mathrm{gcm}^-3$ over a period of 10^6 seconds. The hydrogen abundance is multiplied by a factor of 10^2. The dashed vertical line corresponds to δt (Table 3.3).

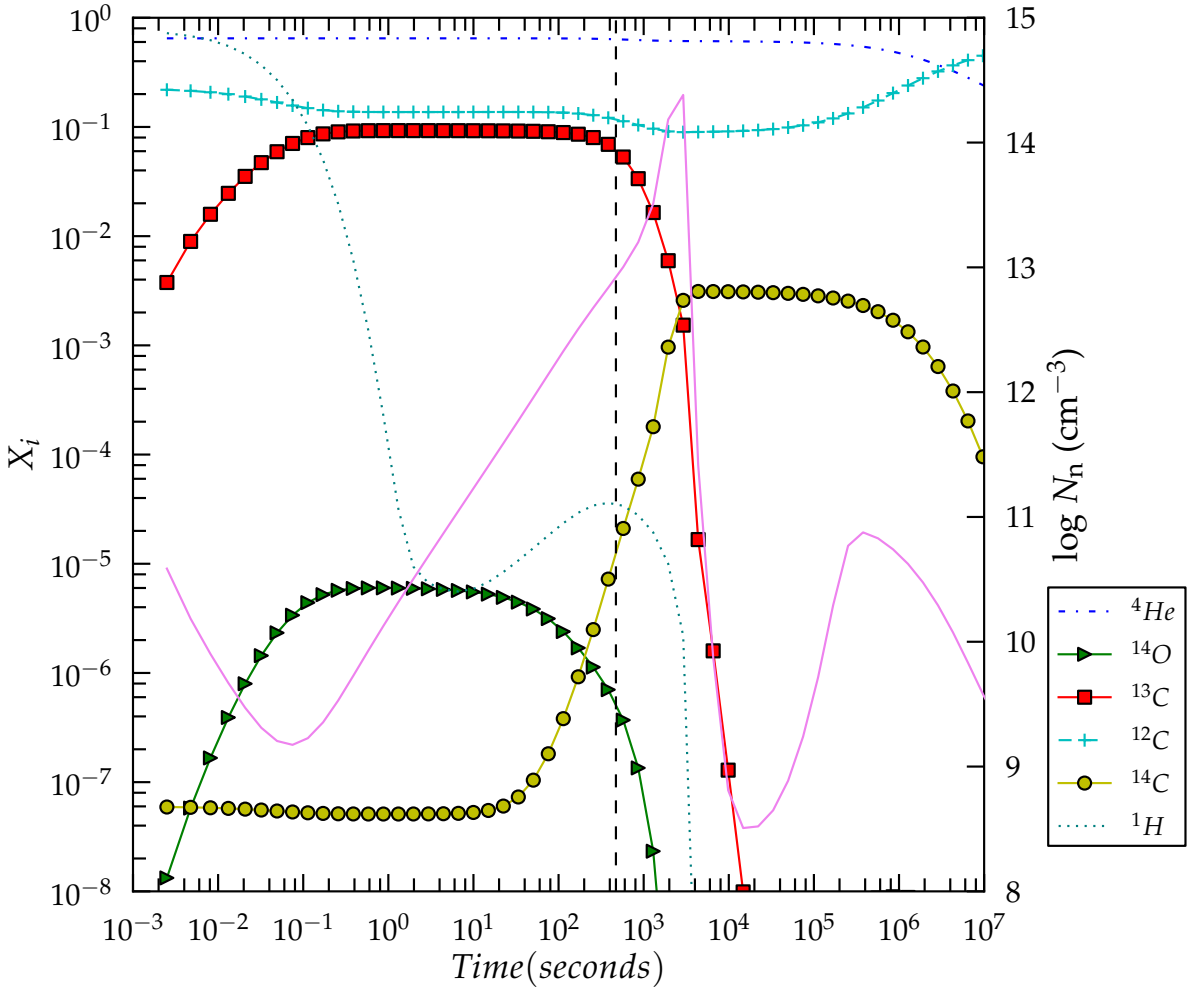

Figure 3.10: Evolution of the neutron density (solid violet line) in the SOF of the $q = 0.5$ simulation, along with the mass fraction (X_i) of those species relevant to its evolution. The hydrogen abundance is multiplied by a factor of 10^2.The dashed vertical line corresponds to δt (Table 3.3).

ences in the final chemical abundances arise mainly due to the different temperatures. Hence in order to understand the role of nuclear processes for different species, we take the case where they occur over the shortest period of time, viz., the $q = 0.5$ case.

In Fig. 3.7, it is seen that between 10^{-3} and 10^{-1} seconds, proton capture reactions on ^{12}C, ^{14}N, ^{18}O and ^{19}F bring down their initial abundances by an order of 1.5 to 3. Compared to its initial abundance, the ^{18}O abundance drops several orders of magnitude in 10^{-2} seconds. This implies that the amount of initial ^{18}O available, does not help much in lowering the ^{16}O/^{18}O ratio since most of the ^{18}O present initially is destroyed. The ^{13}N abundance reaches a quasi equilibrium value of 0.1 after 0.2 seconds via the destruction of ^{12}C by $^{12}\mathrm{C}(\mathrm{p},\gamma)^{13}\mathrm{N}$. Since the plotted abundances are only of stable nuclei, the rise in ^{13}N abundance is reflected in the increase of ^{13}C.

From 10^{-1} to 10^{3} seconds, the above nuclei are regenerated by the same proton capture reactions that caused their destruction earlier, viz.,

$$\begin{aligned} {}^{17}\mathrm{O}(\mathrm{p},\gamma)^{18}\mathrm{F}(^{+}\beta)^{18}\mathrm{O} \\ {}^{18}\mathrm{O}(\mathrm{p},\gamma)^{19}\mathrm{F} \\ {}^{19}\mathrm{F}(\mathrm{p},\gamma)^{20}\mathrm{Ne} \end{aligned} \tag{3.1}$$

During this time, the neutron abundance continually increases. The main source of neutrons is the $^{13}\mathrm{C}(\alpha,\mathrm{n})^{16}\mathrm{O}$ reaction, along with $^{22}\mathrm{Ne}(\alpha,\mathrm{n})^{25}\mathrm{Mg}$ and other auxillary (α, n) reactions. At ~ 7 seconds, there is a rise in the proton abundance. The three main sources identified to cause an increase of 90% in the proton abundance are,

$$\begin{aligned} {}^{14}\mathrm{O}(\mathrm{n},\mathrm{p})^{14}\mathrm{N} \\ {}^{14}\mathrm{N}(\mathrm{n},\mathrm{p})^{14}\mathrm{C} \\ {}^{13}\mathrm{N}(\mathrm{n},\mathrm{p})^{13}\mathrm{C} \end{aligned} \tag{3.2}$$

along with smaller contributions from auxillary (n,p) reactions.

The proton abundance begins to drop again at nearly 500 seconds as their rapid consumption overwhelms their production. As the α capture on ^{13}C becomes increasingly efficient, the ^{13}C abundance drops rapidly at near 1000 seconds. Consequently, with the neutron source exhausted, the neutron abundance also decreases due to consumption by neutron capture reactions Fig. 3.10. With a lack of neutrons, the reactions of Eqs. 3.3 stop functioning thus not producing fresh protons. Thus the proton abundance drops by being consumed by ^{18}O via

$^{18}O(p,\gamma)^{19}F$ causing the ^{18}O abundance to drop accompanied with a simultaneous increase in the ^{19}F abundance.

Thereafter, it is the reign of partial helium burning reactions. Beginning from 3000 seconds, the abundance of ^{16}O,^{18}O and ^{19}F increase via :

$$\begin{aligned} &^{12}C(\alpha,\gamma)^{16}O \\ &^{14}N(\alpha,\gamma)^{18}F(\beta^{+})^{18}O \\ &^{15}N(\alpha,\gamma)^{19}F \end{aligned} \tag{3.3}$$

At around 40,000 seconds ^{18}O reaches its peak and begins to get converted to ^{22}Ne by $^{18}O(\alpha,\gamma)^{22}Ne$. This destruction exceeds the production of ^{18}O and its abundance drops to 10^{-8} at 10^{8} seconds and continues to drop as time goes on.

The $q = 0.6$ and 0.7 cases with a constant temperature of $T = 1.23 \times 10^{8}K$ and $T = 2.1 \times 10^{8}K$ (these temperatures are calculated assuming the abundances given in Table 3.6), respectively, show a slower evolution of nuclear abundances (Figs. 3.8, and 3.9) compared to the $q = 0.5$ case. Over a longer time period, these cases will also show the same abundance trends as the $q = 0.5$ case.

Fig. 3.11 plots the evolution of $^{16}O/^{18}O$ in the SOF for each low-q case. To construct this plot the nucleosynthesis network was run for a longer time period viz., 10^{13} seconds. Within the time scale of the plots in Figs. 3.7, 3.8, and 3.9 the lowest $^{16}O/^{18}O$ value in the SOF is ~ 16 and is found in the $q = 0.6$ case at about 10^{6} seconds after the SOF forms. It increases to 23 in 2.4×10^{6} seconds and continues to increase thereon. In the $q = 0.5$ case, the minimum value of this ratio is ~ 30, which is higher than the 0.6 case due to a faster destruction of ^{18}O to ^{22}Ne while in the 0.7 case the minimum value is $\sim$ 13,900 as there is hardly any ^{18}O being produced.

However on maintaining the T, ρ conditions of the 0.7 case for $\sim 10^{9}$ seconds, the lowest possible $^{16}O/^{18}O$ value in the SOF is found to be ~ 4. The O-isotopic ratio stays close to 5 between 10^{9} and 10^{12} seconds. Thus, it is possible to reproduce in the SOF the $^{16}O/^{18}O$ ratio found in RCB stars for a significantly large period of time. However, it requires the initial abundances of the SOF of the 0.7 case and the sustainance of constant temperature and density conditions of this case.

From Eqs. 3.4, the maximum amount of ^{18}O that can be produced is also limited by the amount of ^{14}N present. The metallicity of the He WD progenitor determines the initial abundance of ^{14}N but as can be seen in the nucleosynthesis calculations, new ^{14}N is formed by

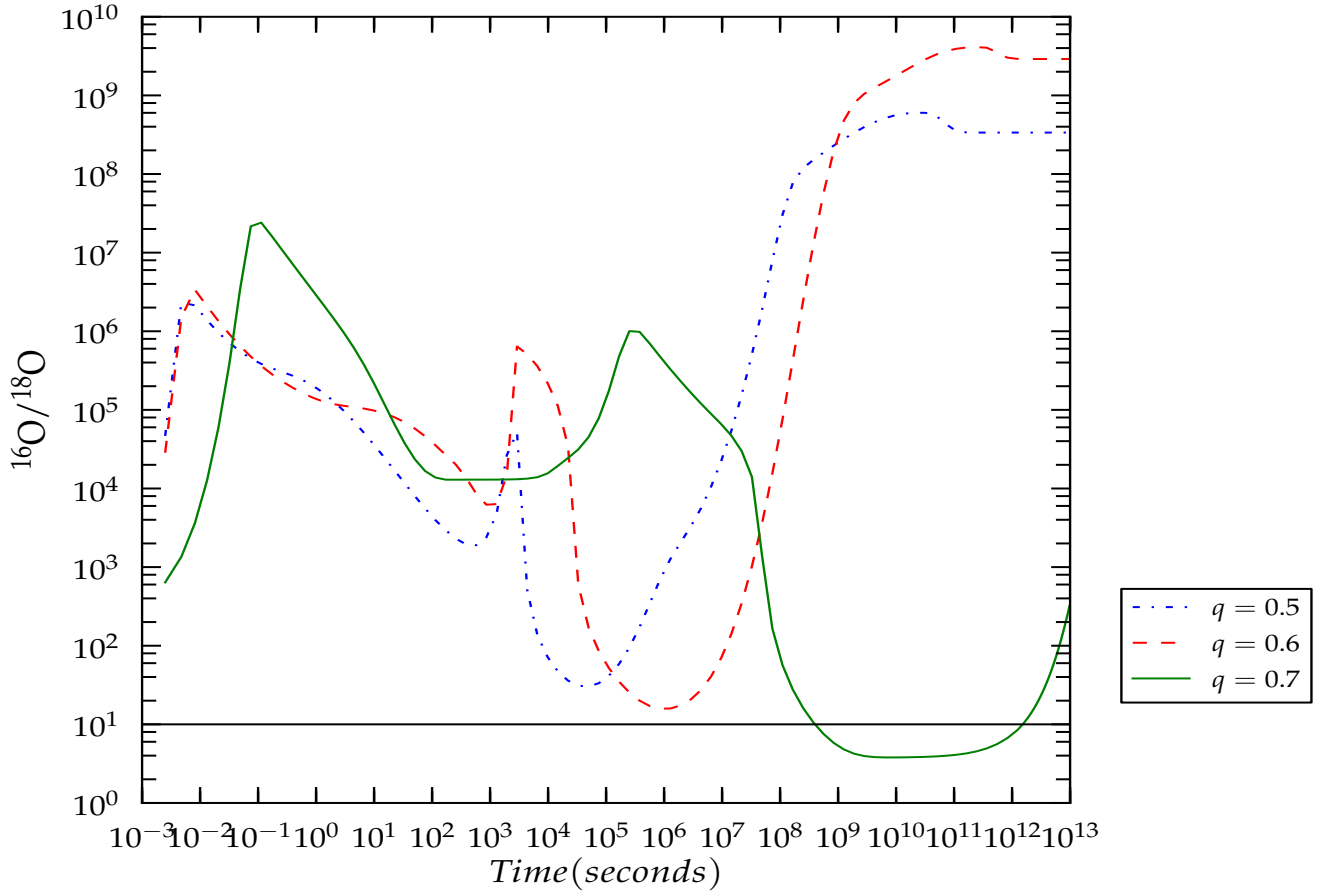

Figure 3.11: Evolution of the $^{16}O/^{18}O$ ratio in the SOF of the $q = 0.5$, 0.6, and 0.7 cases from 10^{-3} to 10^{13} seconds. The black horizontal line stands for the upper limit of 10 measured in RCBs.

H-burning via the partial CNO cycle. The dredge up of accretor material and consequently the ^{16}O added to the SOF poses another constraint on this oxygen isotopic ratio.

The fluorine enhancement in RCBs is observed to be between $1 - 2.6$ dex with respect to solar (Pandey et al., 2008). The F I lines from which the fluorine abundance is deduced, are found for stars hotter than 6200 K while CO bands required to obtain the O16/O18 ratios are detected only in stars cooler than 6000 K. Hence one does not have a set of measurements of F and the O-isotopic ratio for the same star. Nonetheless we try to see if sizeable fluorine enhancements are possible in the SOF. The ^{19}F content of the SOF, given by $[F] = \epsilon_{F_\star} - \epsilon_{F_\odot}$ in Fig. 3.12, is below solar ([F]<0) for the dynamic timescale of

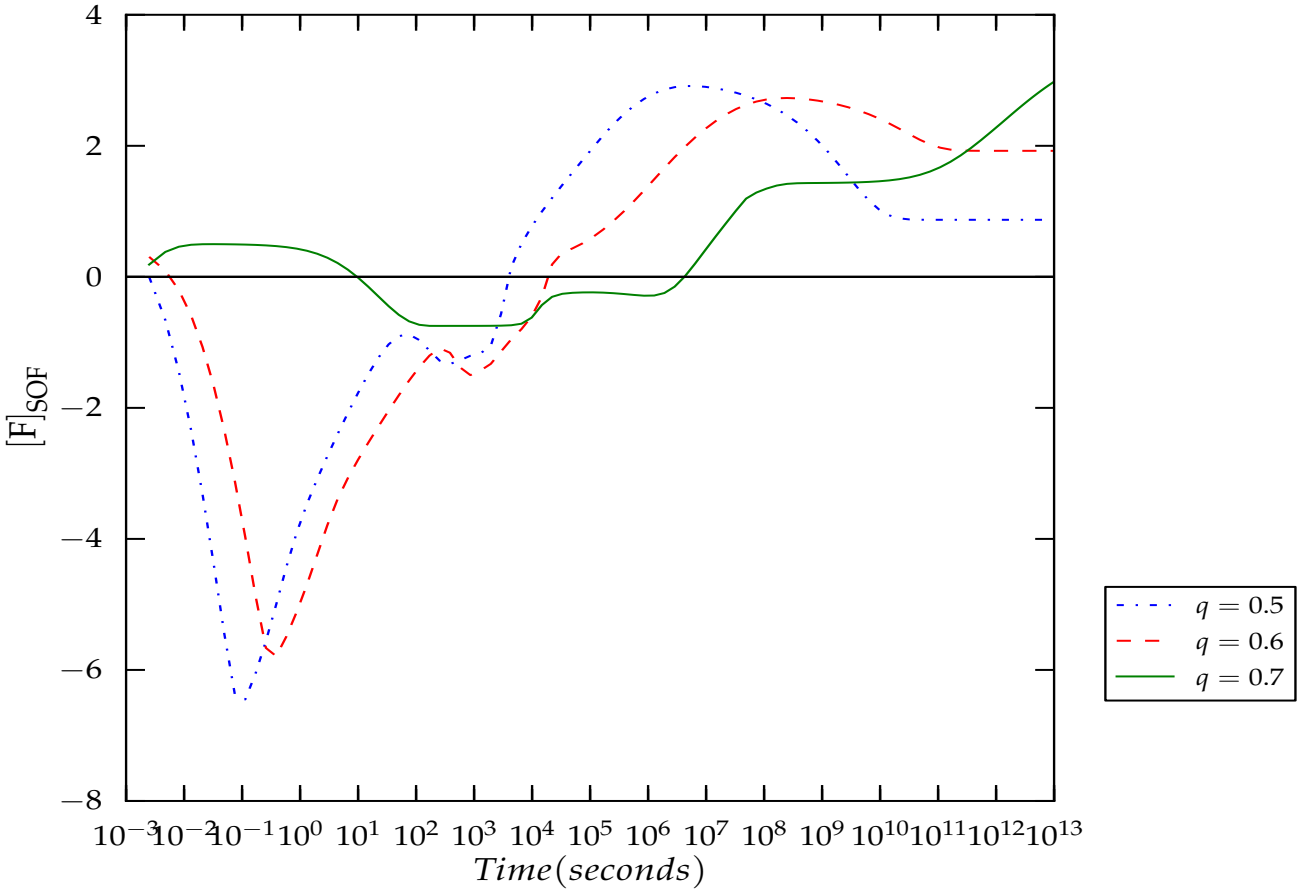

Figure 3.12: Evolution of the ^{19}F mass fraction in the SOF of the $q = 0.5$, 0.6, and 0.7 cases from 10^{-3} to 10^{13} seconds. The black horizontal line stands for [F]=0.

< 1000 s. However, it rises above solar ([F]> 0) by the reaction $^{15}\mathrm{N}(\alpha,\gamma)^{19}\mathrm{F}$, at $\sim 10^5$ s for the $q = 0.5$ and 0.6 simulations and peaks at $\sim 10^6$ s and $\sim 10^8$ s respectively, by up to 2.8 dex. It is then destroyed by $^{19}\mathrm{F}(\alpha,\mathrm{p})^{22}\mathrm{Ne}$ and [F] drops until its production and destruction reactions reach an equilbrium, after which the fluorine content becomes stable in the SOF. The enhancements of F at the time of the minimum values of the O-ratio are : up to 0.7 dex between $10^4 - 10^5$s for $q = 0.5$, 1.5 dex between $10^5 - 10^7$s for $q = 0.6$ and 2.5 dex between $10^9 - 10^11$s for $q = 0.7$. Thus it is indeed possible to have a low O-ratio simultaneously with ^{19}F enrichment.

During the initial H-burning phase of the SOF, the reaction $^{12}\mathrm{C}(\mathrm{p},\gamma)^{13}\mathrm{N}$ increases the ^{13}N abundance in the SOF and thus the ^{13}C abundance by beta decay. This explains why

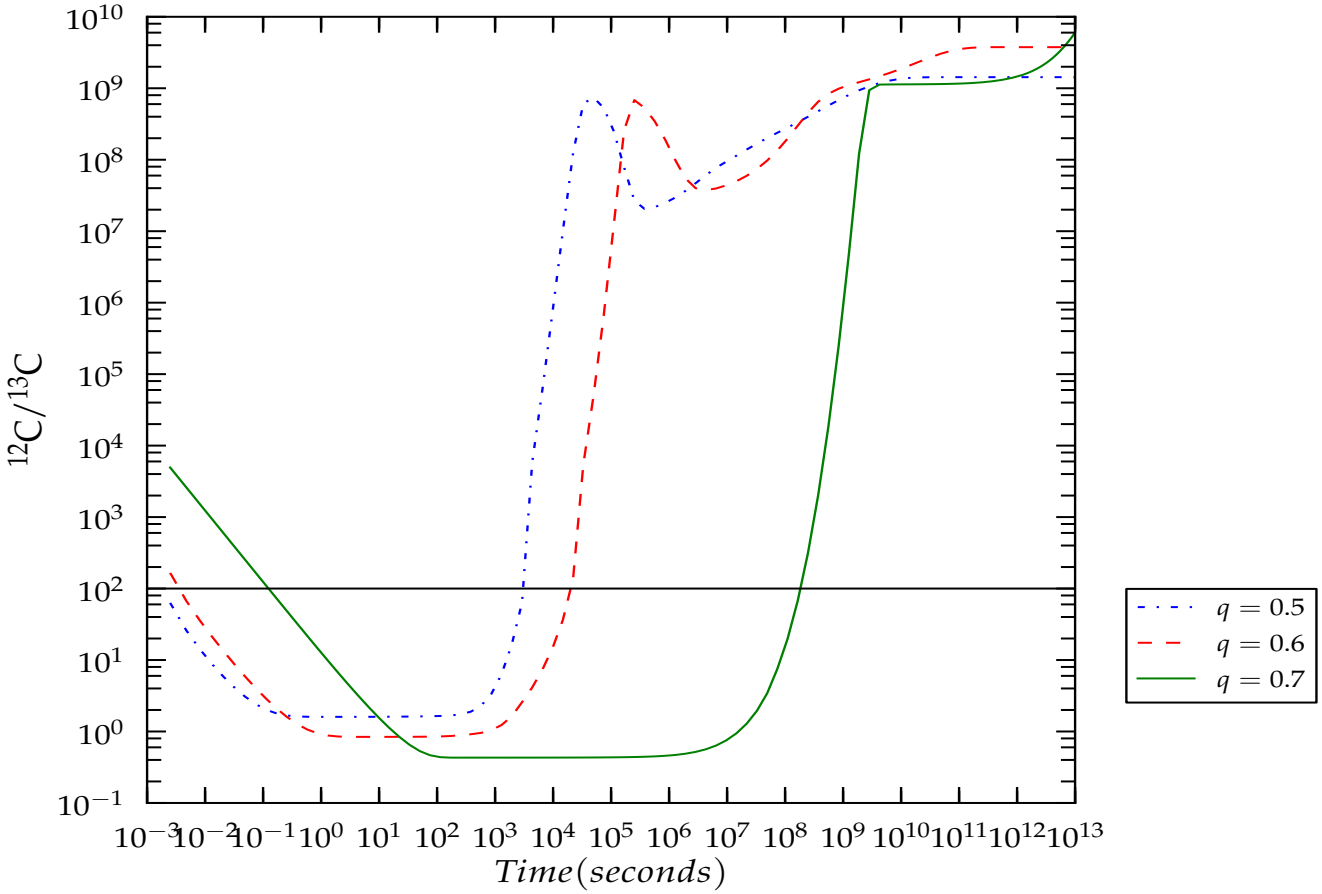

Figure 3.13: Evolution of the $^{12}C/^{13}C$ mass fraction in the SOF of the $q = 0.5$, 0.6, and 0.7 cases from 10^{-3} to 10^{13} seconds. The black horizontal line stands for the lower limit of 100 measured in RCBs.

the initial $^{12}C/^{13}C$ ratio is so low in the dynamical period of 1000 seconds (Fig. 3.13). When He-burning begins in the SOF, α-capture on ^{13}C decreases its abundance. This coupled with the production of ^{12}C, due to the triple-α chain causes the C-ratio to soar above the prescribed lower limit of 100 for RCBs, after $\sim 10^3 - 10^4$ s in the $q = 0.5, 0.6$ cases and $\sim 10^8$ s in the $q = 0.7$ case.

In order to confirm that ~ 4 is the lowest $^{16}O/^{18}O$ value one can get from our grid of CO WD models (section 3.3.2), the nucleosynthesis calculations are also done by constructing initial abundances in the same manner as done for the SOF of the $q = 0.7$ case with the same He WD model and the other CO WD models, CO WD(2) and (3). The evolution of

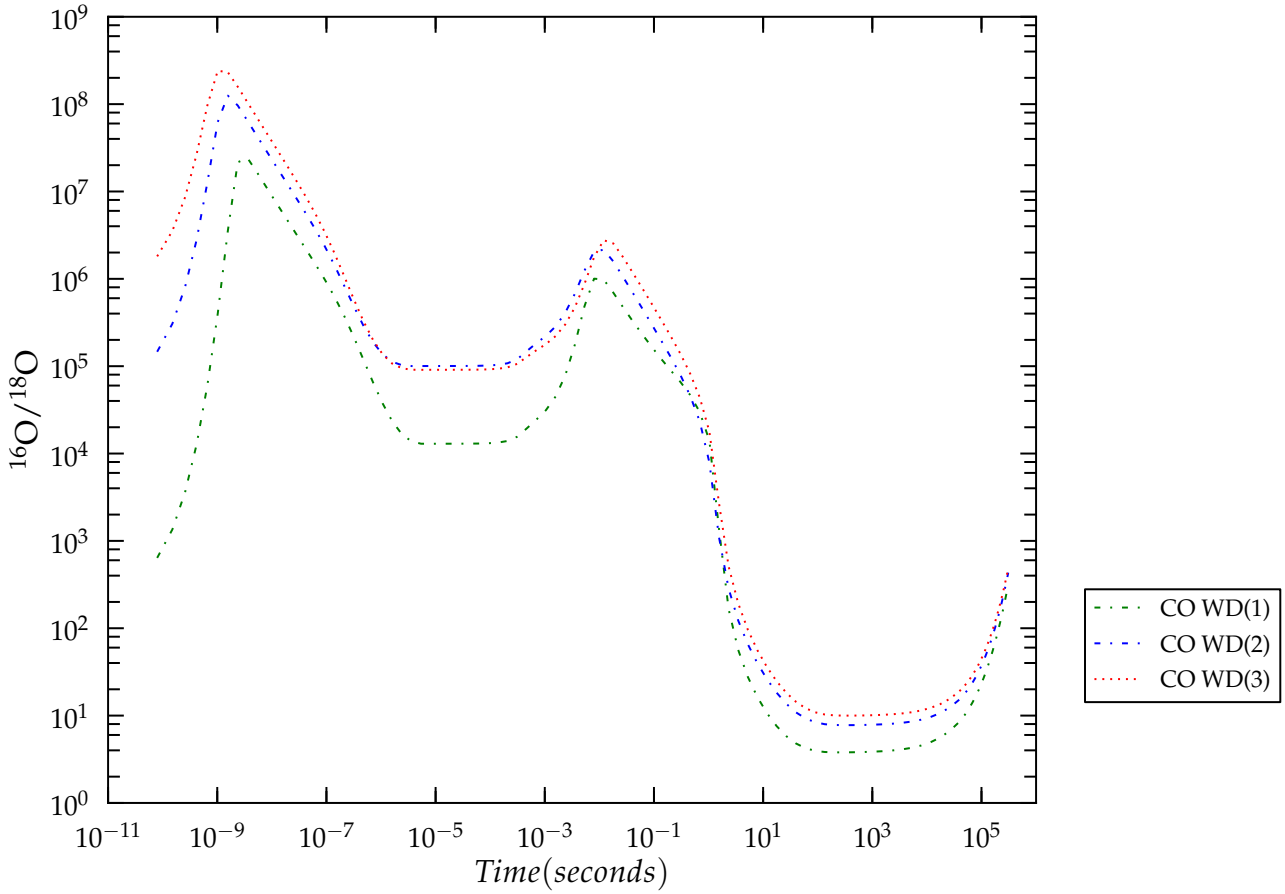

Figure 3.14: Evolution of the $^{16}O/^{18}O$ ratio for initial abundances build from CO WD(1), (2) and (3) in Table 3.4 for the SOF of the $q = 0.7$ case between 10^{-3} and 10^{13} seconds.

the isotopic ratio is quantitatively similar between each CO WD progenitor (Fig. 3.14) and it can be seen that indeed the lowest value is found for the progenitor system containing model CO WD(1).

In order to estimate an approximate value of this ratio in the surface of the merged object, we mix the post nucleosynthesis material of the SOF with the cold envelope above it (of mass $M_{\rm env}$, Table 3.3). For every timestep of the nucleosynthesis calculation of the SOFs of all three low-q cases (as in Fig. 3.11), we mix the masses of ^{16}O and ^{18}O in the SOF with their corresponding masses in the unprocessed envelope above it. The lowest value of $^{16}O/^{18}O$ amongst all three cases thus obtained in the surface, is 4.6 (corresponding to the same timestep at which 4 is obtained) belonging to the $q = 0.7$ case.

3.5 Results and Discussions

The ratio of ^{16}O to ^{18}O is observed to be very low ($\simeq 1-10$) in RCB stars. From hydrodynamic simulations of double degenerate mergers for various mass ratios, we have therefore looked for conditions that would allow for production of ^{18}O in order to explain this ratio. The hydrodynamic simulations of only the low mass ratios, $q \lesssim 0.7$ showed features where ^{18}O could possibly be produced viz., the SOF with temperatures between $1.23 - 2.42 \times 10^8$ K and densities between $3.16 - 5.01 \times 10^4\,\mathrm{gcm}^{-3}$. Within the dynamic-merger time scale, we do not find very low oxygen ratios in the SOF in any of our simulations. The lowest O-ratio we find in this timescale is about 2000 after a 1000 s in the $q = 0.5$ case. This is because not much ^{18}O is produced on such a short time scale that can compete with the large amount of ^{16}O dredged up from the accretor.

However on keeping the T, ρ conditions constant for $\simeq 10^4$ s, the O-ratio in the $q = 0.5$ simulation reaches its lowest value of ~ 30 (Fig. 3.11). After that, ^{18}O is destroyed to ^{22}Ne by He-burning and the ratio increases. The $q = 0.6$ simulation reaches its lowest value of 16 after $10^6 - 10^7$ s, after which the ratio increases again as ^{18}O is being destroyed. Our best situation for obtaining low oxygen ratios is by keeping the T, ρ of the $q = 0.7$ simulation constant for $\sim 10^2$ years. In this case, ^{16}O/^{18}O drops to a value of 4, which is well within the range of observed O-ratios in RCB stars. In fact, such a low value of ^{16}O/^{18}O has not been obtained from the results of any previous hydrodynamic simulation work.

We also find that the enhancements of F found in RCBs can be obtained in the SOF only over a longer duration following the merger, of up to 2.5 dex. During the times that the O-isotopic ratio drops to a minimum for each q case, the fluorine abundance is also within the range of observed values. Thus although F and the ^{16}O/^{18}O ratio are not detected simultaneously in RCB stars (owing to their surface temperature requirements), our results clearly indicate that all F enriched RCBs must also have low O-ratios. The ^{12}C/^{13}C ratio is also lower than observed in RCBs, during the dynamic merger period but increases above 100 after a period of $\geq 10^4$ s.

The ^{16}O to ^{18}O ratio depends both on the formation of ^{18}O, and also on the amount of ^{16}O present. In all the hydrodynamic simulations, a significant dredge up of accretor material which consists primarily of ^{16}O and ^{12}C takes place. Thus one of the reasons for the high O-ratios during the dynamic merger may be due to the high amount of ^{16}O dredged up from the accretor. The hydrodynamic simulations do not account for energy release due to nuclear reactions during the merger and this also could play a role in affecting the SOF's conditions.

An E-AGB progenitor for the CO WD, does produce the lowest $^{16}O/^{18}O$ amongst the other AGB progenitors studied, but the value of this ratio changes only slightly between the choices of the AGBs. Thus the type of progenitor AGB star does not affect the O-isotopic ratio. All the ^{18}O is formed by the He-burning of ^{14}N in the SOF and is independent of its initial value. ^{14}N is generated by the burning of ^{1}H in the SOF, which is mainly contributed by the He WD.

To summarize, from the nucleosynthesis calculations of the SOF, it was found that the low O-isotopic ratios, enhancements in F and high C-ratios of RCBs, cannot be obtained during the dynamic timescale of the merger. These ratios only reach the observed values over a much longer duration of over ~ 100 years. Thus, these results pave way for the need of an investigation of the nucleosynthesis processes in a long term evolution scenario of the merged product and whether, along with the above three chemical signatures, the other elemental abundances of RCBs can also be obtained. The details of such an investigation are what follow in the next chapter.

Chapter 4

RCBs - from long term evolution of merged WDs

In the previous chapter it was concluded that the low O-isotopic ratio, high C-isotopic ratio and high F enhancements observed in RCBs cannot be produced during the dynamic merger phase of the WDs. We hypothesize that the unusual abundance patterns of RCBs could be the result of the long-term evolution and nucleosynthesis following the dynamic phase.

4.1 Introduction

Attempts to understand whether the merger of a CO and He WD would lead to the formation of RCB supergiants were first done by Weiss (1987) with 1-D He-rich homogeneous stellar evolution models. These included C,O and trace amounts of H and were successfully evolved into the RCB region in the HR diagram. Later, Saio & Jeffery (2002) performed a stellar evolution calculation by accreting He WD material (of a pure helium composition with a very small H-rich envelope mass) onto a CO WD at the rate of $10^{-5} M_{\odot}$/year. Although the location of the final model in the HR diagram was consistent with that of EHes and RCBs, the accretion rate was much smaller than the expected rapid mass-transfer rate of $\sim 10^{3} M_{\odot}$/year (Staff et al., 2012; Lorén-Aguilar et al., 2009) during the final merging phase of degenerate WDs.

According to single zone nucleosynthesis analysis by Clayton et al. (2007), rapid mass-transfer events in He+CO WD binaries could lead to thermodynamic conditions in which these ratios can originate. Their results showed that by keeping the temperature range between $1.2 - 1.9 \times 10^{8}$ K at a density of $10^{3}\,\mathrm{gcm}^{-3}$ for $\sim 250 - 320\,\mathrm{years}$, ^{18}O can be

produced by partial He-burning via $^{14}N(\alpha,\gamma)^{18}F(\beta^+)^{18}O$, without destroying it by further α-capture to ^{22}Ne. At these temperatures, ^{13}C is consumed by He-burning to form ^{16}O via $^{13}C(\alpha,n)^{16}O$ which helped explain the high C-isotopic ratios, while the neutrons released from this reaction were expected to result in the production of s-process elements (this aspect was not inspected by these authors).

SPH simulations of the dynamic merger phase of He and CO WDs, which were performed over a range of mass combinations by Lorén-Aguilar et al. (2009), included a 14-species nuclear network. The abundance yields in the hot corona of the final models of masses $\geq 1.2M_{\odot}$, showed enrichments of Ca, Mg, S, Si, and Fe. Longland et al. (2011) carried out a one-zone nucleosynthesis post-processing analysis using the temperature and density conditions of the corona of the final model from these simulations. The AGB model used to build their initial composition consisted of 7 nuclear species from ^{1}H to ^{22}Ne. They reported that depending on the depth of mixing within the corona, the $^{16}O/^{18}O$ ratio of the corona could be between 19 - 370. However their total C and O abundances exceeded the upper limit of RCB values while their F yields were much lower than the observed values. As their models did not include s-process elements, they could not make predictions about these.

So far, Jeffery et al. (2011) have done the most detailed theoretical investigation of RCB surface abundances, by using a cold mixing recipe (i.e. without any in-situ nucleosynthesis). A 1-D 'cold merger' model was built by simply mixing different proportions of masses between He WDs and CO WDs and a 'hot merger' model was built by incorporating the results obtained in the above SPH simulations by Lorén-Aguilar et al. (2009). In both cases, barring C, N and O (and S in the hot merger model), the elemental abundances obtained from their mixing recipe fell short of the observed ones in RCBs, particularly the s-process elements, which were believed to originate solely from the progenitor AGB star. They also stated that any additional nucleosynthesis that may occur during the actual merger of an He and CO WD cannot solve the conundrum of RCB chemical compositions.

The single zone nucleosynthesis results of the 'Shell of Fire' (SOF) feature in the hydrodynamic simulations from the previous chapter, showed that the lowest $^{16}O/^{18}O$ ratio possible during the dynamic timescale of the merger was of the order of 1000. This is much lower than the observed $^{16}O/^{18}O$ of an order between 1-10 in RCB stars. Similar results were obtained for the fluorine enhancements and the $^{12}C/^{13}C$ as well. The conclusion thus arrived at, was that if the above three features are essential features of all RCBs, then RCBs are not formed immediately after the dynamic merger period.

We now explore the possibility of these chemical signatures, along with the individual

elemental abundances in RCBs being a result of the long term evolution after the dynamic merger phase of the CO+He WDs. Currently, there are two theories as to how the long term evolution of a merged WD system could proceed. One is via accretion of the post merger disk remnant onto the core over either a timescale of 10^5 years (Yoon et al., 2007) or over a few hours (van Kerkwijk et al., 2010). The other is where the merger remnant at the end of the dynamic phase enters a longer viscous evolution phase with a rigid primary WD and with a tidally disrupted secondary WD undergoing Keplerian rotation. During this phase (which lasts between $10^4 - 10^8$ s (Shen et al., 2012)), viscous mechanisms (from magnetohydrodynamic instabilities) cause shearing forces in the remnant that stimulate an outward transport of angular momentum. These shearing forces also cause an increase in the peak temperature of the SOF/corona of the remnant by a factor of ~ 2 and work on expanding the material to larger radii. Schwab et al. (2012) show that towards the end of the viscous phase, the remnant evolves towards a spherically symmetric, almost shear-free steady state with a thermally-supported envelope, undergoing solid body rotation. These authors expect a star-like long term evolution of the object to occur after the viscous phase wherein, the object would grow into a giant star with the luminosity from its internal nuclear-burning, driving convection in its cool extended envelope, thus creating a path leading from the merger of white dwarfs to the formation of giant stars such as RCBs.

Based on the latter scenario, we construct spherically symmetric one-dimensional models of merged WDs, with a range of initial conditions and follow their evolution into the domain of the HR diagram where RCBs are observed to lie. Along with convective mixing, these models also include an induced, continuous mixing profile purported to result from the rotation of the merger-remnant. We then perform a multi-zone post-processing nucleosynthesis analysis of these models and compare their surface abundances with those of RCBs. Such a study of the nucleosynthesis occuring during the long-term evolution of a merged WD system, is an endeavour that has not been undertaken in the past. The results of this chapter are submitted as a paper to the Astrophysical Journal (arXiv: 1211.3392).

This chapter is divided into the following sections - Methods (section 2), where the progenitor evolution of the system, the construction of the initial models, a brief description of the codes used, the formulation of the mixing profile and the four nucleosynthesis cases studied are presented. This is followed by the Results (section 3), where the stellar and nucleosynthesis processes of the model during its evolution and the comparison between the results from the cases and the observations are analysed, and ends with a section on the Summary and Discussion of our results (section 4).

4.2 Methods

4.2.1 The initial models

Progenitor evolution

The final merging of the CO and He WDs takes place within a dynamic timescale of $10^2 - 10^3$ s and results in a structure consisting of a CO core, surrounded by a shock-heated layer and an envelope in Keplerian rotation (Lorén-Aguilar et al., 2009; Dan et al., 2012; Raskin et al., 2012). In the results of the hydrodynamic simulations discussed in chapter 3, this shock-heated layer was termed as the Shell of Fire (SOF) as it was the hottest and a very dense part of the merged object and was found to last until the end of the simulations. Hence it was considered to be the region where any relevant nucleosynthesis would occur within the dynamic time period.

In light of the work done by Shen et al. (2012); Schwab et al. (2012), we build an initial composition for a model that has a CO core, an SOF and a differentially rotating envelope, which then evolves over the viscous timescale and is followed by a long term thermal evolution into the RCB phase.

Construction of initial composition

The first step in building the internal composition of the post-merged object is to choose the progenitor AGB and RGB stars of the CO and He WDs respectively, during the CE phase. For constructing the initial abundances, three AGB models are chosen as progenitors to the CO WDs from the Early-AGB (E-AGB), the Early-Thermal Pulse AGB (E-TP AGB) and the Advanced-Thermal Pulse AGB (A-TP AGB) phases (the same as those in Table 3.4). The motivation to take these particular AGB models is to examine how (or if) they would influence the final abundances of the computed models, particularly the s-process elements.

For the purpose of this study we choose the E-AGB and A-TP ($21^{\rm st}$ TP) AGB models as progenitors for the CO WD (which has an H-rich envelope of the order of $10^{-4} M_{\odot}$) and the RGB model for building a homogenous He WD (with an H-rich envelope of mass of an order of $10^{-3} M_{\odot}$). The masses of the different layers of the WDs are listed in Table 4.1.

The one-dimensional realization of composition of the post-dynamic merger object, motivated by the hydrodynamic simulation results, is in the form of a four-zone model consisting of the relatively cold, degenerate core (of the CO WD), a buffer zone, the SOF itself and a relatively cold envelope (Fig. 4.1). For each mass ratio, $q = M_{\rm He\,WD}/M_{\rm CO\,WD}$, a certain

Table 4.1: WD masses used for the initial models of the post-merger evolution. $M_{\rm WD-core}$ stands for the mass of the WD core and $M_{\rm env}$ for the H-rich envelope in factors of 10^{-4}

WD	Progenitor (initial mass/$M_\odot$)	$M_{\rm WD}/M_\odot$	$M_{\rm WD-core}/M_\odot$	$M_{\rm env}(10^{-4})M_\odot$)
CO	E-AGB (3.00)	0.58148	0.4876 (He-free)	2.4
CO	A-TP AGB (2.00)	0.61243	0.5789 (He-free)	1.7
He	RGB (1.65)	0.3024	0.296 (H-free)	64.3

fraction of mass ($f_{\rm dre}$) being dredged up from the CO WD ($M_{\rm CO\,WD}$) and mixed with the He WD ($M_{\rm He\,WD}$) on the surface. The amount of dredge up defines the outer boundary of the core ($m_{\rm core}$, (Eq. 4.2)). As this dredged-up mass from the He-rich layers of the CO WD mass ($m_{\rm dre}$) is pulled up to the envelope (see Fig. 11 Staff et al., 2012), an equal mass of He WD also makes its way into the CO WD. Thus a partially mixed zone is formed between the two WDs. A major portion of the mass in this zone occupies the SOF ($m_{\rm SOF}$) while the rest is in buffer the zone between the core and the SOF ($m_{\rm buffer}$). Of the $m_{\rm dre}$ from the He WD , a small fraction of it resides in the SOF ($m_{\rm he-sof}$) while the majority of this mass is in the buffer zone. The SOF thus contains most of the mass dredged up from the CO WD ($m_{\rm co-sof}$). Finally, the envelope ($m_{\rm env}$) contains the fraction of $m_{\rm dre}$ from the CO WD that is not present in the SOF and the remaining unmixed He WD mass.

$$
\begin{aligned}
m_{\rm dre} &= f_{\rm dre} \times M_{\rm CO\,WD} \\
m_{\rm core} &= M_{\rm CO\,WD} - m_{\rm dre} \\
m_{\rm buffer} &= m_{\rm dre} - m_{\rm he-sof} \\
m_{\rm SOF} &= m_{\rm he-sof} + m_{\rm co-sof} \\
m_{\rm env} &= M_{\rm HeWD} - m_{\rm co-sof}
\end{aligned}
\tag{4.1}
$$

The assumptions we make to construct the initial abundances of the four-zone model are the same as those made in the single zone calculations of chapter 3. These are that the exchange of masses during the dynamic merger phase occurs before the onset of burning in any given layer. The initial model of the post-merger evolution for the purpose of this study, has an SOF and a buffer zone that has already been burnt for a particular time period, within the viscous timescale of $10^4 - 10^8$s (Shen et al., 2012). The abundances of the He WD are averaged over its mass, making the He WD have a uniform composition throughout. After

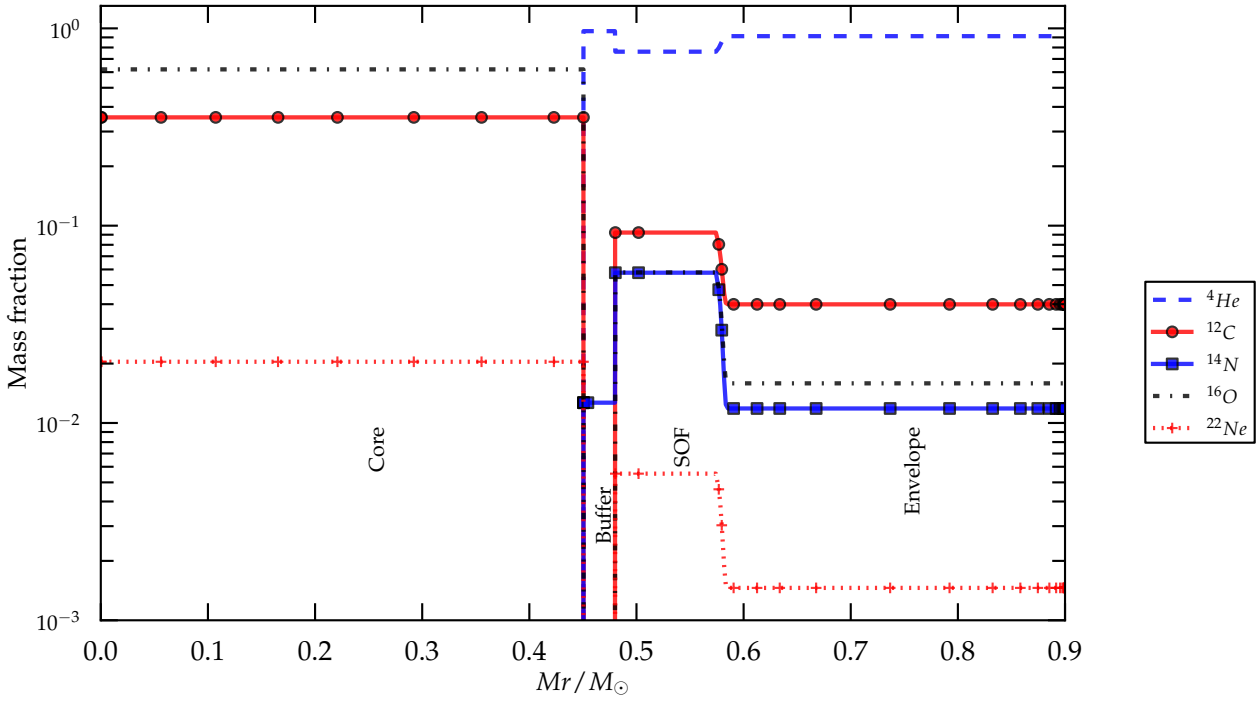

Figure 4.1: The four zone post-merger initial model of the q =0.7, E-AGB CO WD with a dredge-up depth of 15% (case 1)

extracting the abundances of each zone of the progenitor models, the isotopic abundances of that zone are averaged over its mass.

The cases

The hydrodynamic simulations reported dredge-up depths ranging from 15% to 18% of mass into the CO WD for the three low-q cases. The He-free core of a CO WD is most abundant in ^{16}O and it is located within the dredge-up depth of the simulations according to the progenitor models chosen for the single-zone analyses in chapter 3 (Table 3.4). If material is dredged up from the core, then the star becomes more enhanced in oxygen than carbon in the surface which is not observed in RCB stars. The other problem of dredging up high amounts of oxygen is that the star would have much higher ^{16}O/^{18}O ratios than the range of $\sim$ 1-10 observed in RCBs. This indicates that in order to avoid the surface pollution of ^{16}O, the dredge up of mass from the chosen CO WD models should be lower than the values obtained in the hydrodynamic simulations. We thus restrict the dredge up level in our models to just above the He-free core of the CO WD (ranging from $\sim$ 5.4% in the A-TP to $\sim$ 16% in the E-AGB CO WD model (Table 4.1).

For the purpose of this work, we study the long-term evolution of four cases built out of two CO+He WD systems from the hydrodynamic simulations, namely the $q = 0.7$ case ($M_{\rm CO\,WD} = 0.53\,M_{\odot}$ and $M_{\rm He\,WD} = 0.37\,M_{\odot}$) with an SOF of $T = 1.23 \times 10^8\,$K and $\rho = 5.02 \times 10^4\,{\rm gcm}^{-3}$ and the $q = 0.5$ case ($M_{\rm CO\,WD} = 0.60\,M_{\odot}$ and $M_{\rm He\,WD} = 0.30\,M_{\odot}$) with an SOF of $T = 2.42 \times 10^8\,$K and $\rho = 3.16 \times 10^4\,{\rm gcm}^{-3}$. From the hydrodynamic simulations, we judge that the buffer zone has a temperature of approximately $50 \times 10^6\,$K and the same density as the SOF of that case. The core being cold (and not involved in the mixing) is exempted from nucleosynthesis calculations as also is the envelope since it has a temperature and density that are too low for any significant nucleosynthesis t to occur during the short dynamic phase. The SOF and the buffer zone are burnt over a particular period of time to build the initial composition; the short-sof is burnt up to 7.2×10^4s and the long-sof up to $3.2 \times 10^6\,$s, both of which are within the viscous timescale.

The four cases are constructed over a span of the CO and He WDs of the two mass ratios (q =0.5 and 0.7), their corresponding SOF parameters (T,ρ and the proportion of CO and He WDs in them), the chosen short or long duration of SOF burning and the progenitor AGB model for the CO WD for nucleosynthesis analysis (Table 4.2). We study the stellar and nucleosynthesis cases evolved from four representative initial compositions.

Table 4.2: Summary of the physical parameters of the four cases. These are the mass of the CO WD ($M_{\rm CO\,WD}$), the He WD ($M_{\rm He\,WD}$), the core ($m_{\rm Core}$), the buffer zone ($m_{\rm buffer}$), the SOF ($m_{\rm SOF}$) along with the percentage of CO WD material and the envelope ($m_{\rm env}$); all masses are in $M_\odot$. Columns 4 and 5 contain the progenitor AGB models used to construct the CO WD (AGB) and the percentage of dredge up from within the CO WD ($f_{dre}(\%)$). The last two columns, $\tau_{\rm SOF}$ and colour indicate the duration of burning of the SOF (long : long-sof and short: short-sof) and the colour representation of the cases in Fig. 4.11.

CASE	$M_{\rm CO\,WD}/M_\odot$	$M_{\rm He\,WD}/M_\odot$	AGB	f_{dre}	$m_{\rm Core}/M_\odot$	$m_{\rm buffer}/M_\odot$	$m_{\rm SOF}/M_\odot$	$m_{\rm env}/M_\odot$	$\tau_{\rm SOF}$	colour
1	0.53	0.37	E-AGB	15.0	0.4505	0.0295	0.1000	0.32	short	orange
2	0.53	0.37	E-AGB	15.0	0.4505	0.0295	0.1000	0.32	long	red
3	0.53	0.37	A-TP AGB	5.4	0.5014	0.0107	0.0346	0.352	short	blue
4	0.60	0.30	E-AGB	15.0	0.5100	0.0141	0.1060	0.2626	long	green

4.2.2 Analysis of stellar evolution: codes and conditions

MESA (Modules for stellar experimentation) is a stellar evolution package that contains a one-dimensional stellar evolution code called MESA star (Paxton et al., 2011). The version used for this project is v.3851. MESA star solves one-dimensional coupled stellar structure and composition equations for each timestep during the evolution of a spherically symmetric stellar model. It includes nuclear reaction networks, opacity tables and other micro and macro physics modules during the stellar evolution calculation.

MESA star includes a 'relax initial composition' method. With this method, we first write a file with lines that contain mass co-ordinates along with their corresponding specific nuclear abundance distribution, in accordance with the post-merger four-zone composition that was constructed in section 4.2.1. This initial composition file is imposed on a homogeneous main sequence star of the required mass - in this case, $0.90 M_{\odot}$ (the combined mass of the CO and He WDs used in the hydrodynamic simulations). On initiating MESA star, the first part of the simulation would thermally relax the stellar model over a certain number of timesteps (specified by the user) to the required initial composition. During this relaxation phase, no nuclear burning reactions take place that would change the specified initial composition. Once the star is completely relaxed to this initial composition, it begins to evolve in the HR diagram according to its internal compositional and structural changes. We perform such a stellar evolution calculation for each of the compositions in the four cases of section 4.2.1.

The star is evolved with a mass loss rate obtained by setting the coefficient η of the Blöcker's wind formula to 0.05. The results of the stellar evolution calculations for the four cases have been obtained without turning on CO enhanced opacities. The activation of these opacities during the course of the evolution run, produced convergence issues in the code that caused the runs to stop. The few cases that did evolve smoothly with enhanced opacities, evolved to cooler temperatures than their counterparts. Whatever were the choices in opacities, the models did not show differences in the nucleosynthesis aspects. The mixing profile (section 4.2.3) is continuous throughout the star and already includes the contribution of convection and so changing opacities does not affect the magnitude of mixing in the star. Thus the surface abundances of the star remain the same in models with and without enhanced opacities.

Once the stellar evolution calculation is completed, every cycle on the HR track (a cycle corresponds to a point of time during the evolution) is post-processed using the multi-zone nucleosynthesis code **MPPN** from the **NuGrid** family (Herwig et al., 2008). The code consists of an extensive nuclear network spanning over 1000 isotopes and their corresponding

nuclear reactions. The star is divided into ∼1270 radial zones and the stellar evolution processes occuring in each zone (such as the amount of mixing, the energy generated by nuclear burning, etc.) are accounted for by the code. For each cycle, the code outputs a radial distribution of nuclear abundances which are then analysed.

4.2.3 The mixing model

The physical mechanisms of non-convective mixing processes that may occur during or after a merger are not understood well yet. The remnant of such merger understandably has some residual rotation. Shen et al. (2012) estimate that differential rotation in such an object would last for at least $10^4 - 10^8$ seconds after the merging phase after which it evolves to a solid body rotational object (Schwab et al., 2012). Mixing processes can arise out of both the differential and solid body rotation (e.g., meridional circulation). It is found that such an 'extra' mixing mechanism is essential in order to explain the complex abundance patterns found in RCB stars. The convection zone in the stellar model is only present in the surface within 0.1 $M_\odot$ and does not extend deep enough to dredge up the products of H-burning and He-burning from the interior of the star.

We formulate a toy model that may represent rotation-induced mixing in the merger remnant. The zeroeth-order approximation for such a toy diffusion co-efficient ($D_{\rm total}$) consists of convection zones ($D_{\rm MLT}$) arising from the mixing length theory (MLT) and an additional mixing ($D_{\rm add}$) component. $D_{\rm add}$ is the Eulerian representation of a constant mass diffusion coefficient $D_{\rm Lag}$ that drops sharply at the point where an entropy barrier appears due to the peak of nuclear energy generation. The location of this energy peak can be well approximated as the mass-coordinate corresponding to a certain fraction of the maximum ^{14}N abundance (k) (Eqs. 4.2, Fig. 4.2). The mixing is always restricted to the region above $m_{\rm min}$ ($= m_{\rm Core}$ in each case) (Eqs. 4.2 and Table 4.2).

The $D_{\rm total}$ is constructed in such a way that it trails along with the ^{14}N-burning shell in the star. It drops sharply at the mass-coordinate (m_k) where k is the fraction of the maximum abundance of ^{14}N in the mixing region ($m >= m_{\rm min}$), k= $X_{^{14}{\rm N_k}}/X_{^{14}{\rm N_{max}}}$. The nature of this drop (i.e. the ramp near m_k in Fig. 4.2) depends on the term f in the exponent of Eqs 4.2c. The motivation for the construction of the mixing profile is explained below.

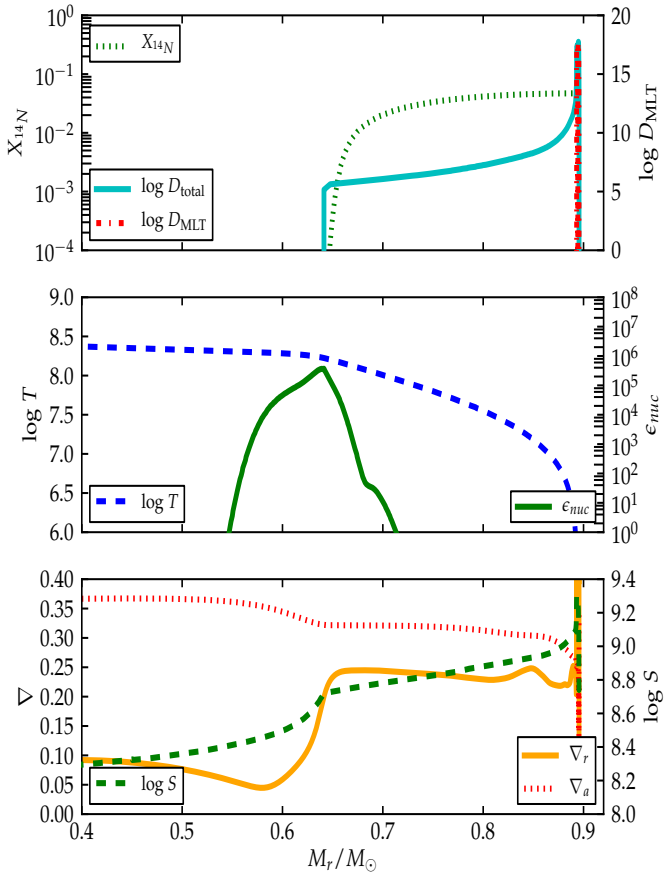

Figure 4.2: The diffusion profile $D_{\rm total}$ of timestep (iv) (Fig. 4.5) of case 1 (black dot in Fig. 4.4) along with the MLT diffusion $D_{\rm MLT}$, in comparison with relevant physical parameters such as the ^{14}N abundance ($X_{^{14}{\rm N}_{\rm k}}$, panel 1), temperature (log T) and nuclear energy generation ($\epsilon_{\rm nuc}$) (panel 2) and radiative (∇_r), convective (∇_a) gradients and entropy (log S) (panel 3).

$$D_{\rm total} = 0 \qquad m < m_{\rm min} \tag{4.2a}$$

$$D_{\rm total} = D_{\rm add} + D_{\rm MLT} \qquad m >= m_{\rm min} \tag{4.2b}$$

$$D_{\rm add} = \frac{D_{\rm Lag}}{(4\pi r^2 \rho)^2} \times exp(\frac{-(T - T_{\rm K}))}{f T_{\rm k}}) \qquad m_{\rm min} \leq m \leq m_{\rm k} \tag{4.2c}$$

$$D_{\rm add} = \frac{D_{\rm Lag}}{(4\pi r^2 \rho)^2} \qquad m \geq m_{\rm k} \tag{4.2d}$$

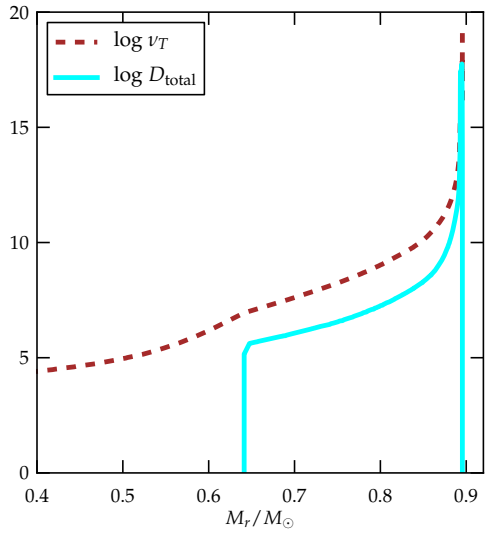

Figure 4.3: The diffusion profile (log $D_{\rm total}$) of timestep (iv) (Fig. 4.5) of case 1 (black dot in Fig. 4.4) along with the thermal diffusivity (log $\nu_{\rm T}$).

For the four cases discussed in this paper (section 4.2.1), the following values for the parameters of Eqs 4.2 are used : $D_{\rm Lag} = 4.5 \times 10^{51}$(cgs), k=0.003 and f=0.05. The manifestation of this equation as a diffusion profile in the star is shown in Fig. 4.2. In Fig. 4.3, $\rm D_{total}$ is compared with the thermal diffusivity $\nu_{\rm T}$, for one of our considered cases. It is seen that $\rm D_{total} << \nu_T$ everywhere inside the star, which means that the additional mixing could be driven by a thermal instability rather than a dynamical one. It is interesting that the ratio between $\rm D_{total}$ and $\nu_{\rm T}$, $\rm D_{total} \sim 10^{-2}\nu_T$, is close to that used by Denissenkov & Pinsonneault (2008) to model extra-mixing in low-mass red giants.

The effect of varying the three free parameters of Eq. 4.2 is briefly summarized here. On increasing $\rm D_{Lag}$ by more than two orders, the mixing becomes too fast causing an excessive increase in ^{12}C and ^{16}O on the surface and a proportionate decrease in ^{14}N, than the levels found in observations. The star tends to become more enhanced in oxygen than carbon, the opposite of which is observed in almost all RCBs. Making $\rm D_{Lag}$ lower by an order causes the mixing to become far too slow in pulling up ^{12}C and ^{16}O to the surface. As the star enters the RCB phase, it becomes more N-rich than C, which again is not observed for any RCB (except for one).

The surface chemical abundances of the star only vary within an order of magnitude, while choosing a value for the parameter k between 10^{-3} and 5×10^{-2}. Below the mass co-ordinate of k ($m_{\rm k}$), the diffusion profile drops very steeply, thus drastically reducing the amount of

mixing below $m_{\rm k}$. We choose ^{14}N as the marker nuclear species for the diffusion profile, since it is involved during the two burning phases in the star - the H-shell burning phase (where it is created via the CNO cycle) and He-shell burning phase (where it is destroyed by α-capture). However, lowering it further would cause the mixing to go deeper into the star resulting an excessive dredge-up of ^{16}O to the surface than desired, while increasing k would cause a shallower dredge up, thus reducing the amount of ^{19}F and other nuclear species brought up to the surface.

A small ramp appears in $D_{\rm total}$ just as it nears $m_{\rm k}$. The beginning of the slope of the ramp and its steepness is decided by the rather sensitive parameter f in the exponent function of T. The ramp feature affects the content of ^{19}F, ^{18}O and ^{16}O in the surface (more discussed in section 4.3.1). The optimal abundances of the star at a given value of $D_{\rm Lag}$ and k are maintained when f is chosen between 0.03 and 0.06.

Finally, we see indications from the nuclear abundance features of the models that mixing must be strongly reduced before the star enters the RCB region of the HR diagram, as will be discussed in section 4.3.3.

4.3 Results

4.3.1 Stellar and Nucleosynthesis evolution

The shapes of the evolutionary tracks of the four cases in the HR diagram are similar to each other and begin at low luminosities (Fig. 4.4). The thin lines in the lower portion of the plot correspond to when the H-shell burning in the star while the thicker lines indicate when He-shell burning takes over. Observed RCBs lie in a range of $T_{\rm eff}$ and log $L/L_{\odot}$: 3000 K<= $T_{\rm eff}$ <=8000 K and 3.5<= Log$L/L_{\odot}$ <=4.0 (Clayton, 1996; Pandey et al., 2008). The models spend between 0.1 (case3) - 2.75 (case4) $\times 10^5$ years in the RCB phase. This age is obtained when the mass-loss rate is $\sim 10^{-}7\,M_{\odot}$/year. Increasing the mass-loss rate decreases the time spent in the RCB phase; a mass-loss rate of $\sim 10^{-}5\,M_{\odot}$/year, would reduce the period of the RCB phase of the model to $\sim 10^4$ years, which is the expected age of an RCB star (Clayton, 2012).

We discuss the different phases of burning and associated nucleosynthesis processes that occur in the course of evolution of the star. To illustrate these phases case 1 is chosen (Table 4.2).

Fig. 4.5(i)a and Fig. 4.5(i)b show the initial distribution of abundances for case 1. The loop in the HR diagram shows when the first burning phase, that of 'H-shell burning' (cyan

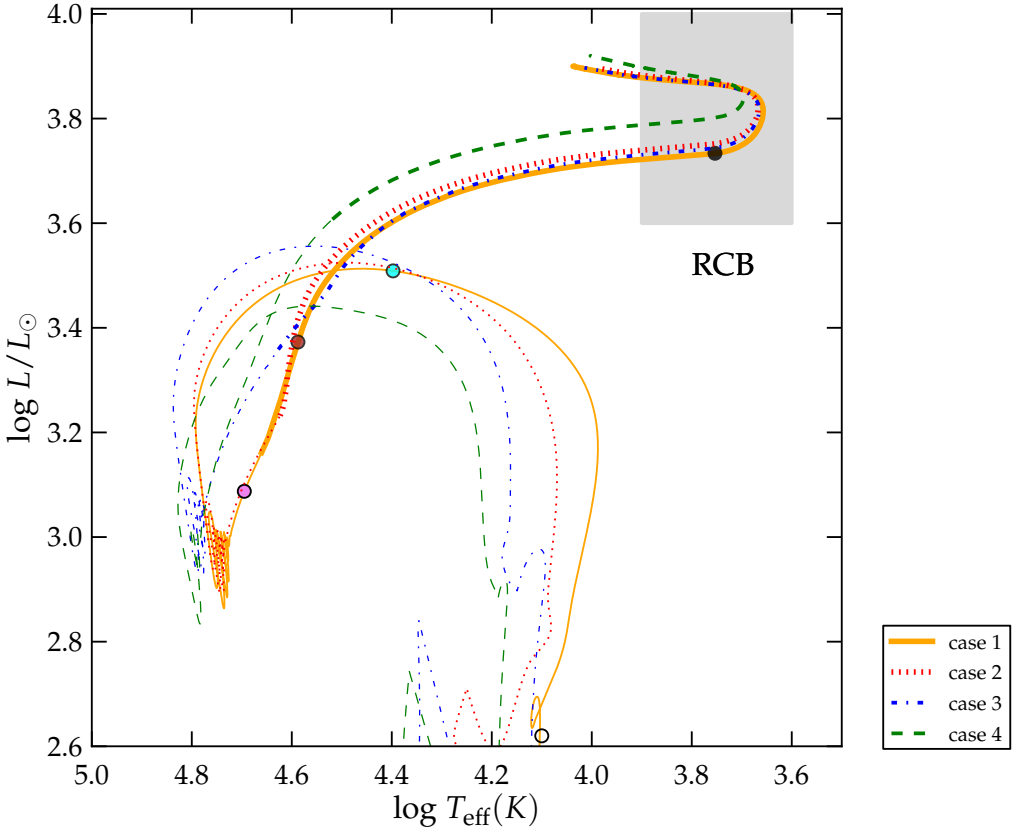

Figure 4.4: The HR diagram of the four considered cases. The thinner portion of the lines indicate part of the evolution when the star burns H in a shell and the grey box shows the area of the HR diagram in which RCBs are observed to lie. The dots correspond to timesteps in the evolution: (i) - 0 years, empty black circle, (ii) - 4.2×10^5 years, cyan dot and (iii) - 6.7×10^5 years, violet dot, (iv) - 1.3×10^6 years, brown dot and (v) - 7.2×10^6 years, black dot.

dot in Fig. 4.4) occurs via the CNO cycle. The hydrogen contribution to the merged CO+He WD system is primarily from the H-rich envelope of the original He WD, which is uniformly distributed throughout the He WD in our construction of the initial model. The maximum temperature during this phase is $\sim 10^7$ K, causing the H-shell to burn and move outwards, leaving behind ^{13}C in its wake via $^{12}\mathrm{C}(\mathrm{p},\gamma)^{13}\mathrm{N}(\beta^+)^{13}\mathrm{C}$ accompanied by the ashes of CNO burning, ^{14}N through $^{13}\mathrm{C}(\mathrm{p},\gamma)^{14}\mathrm{N}$. This phase results in an overall increase in the abundance of ^{13}C and ^{14}N in the envelope.

As time progresses, the overall temperature of the star increases; this increase starts first

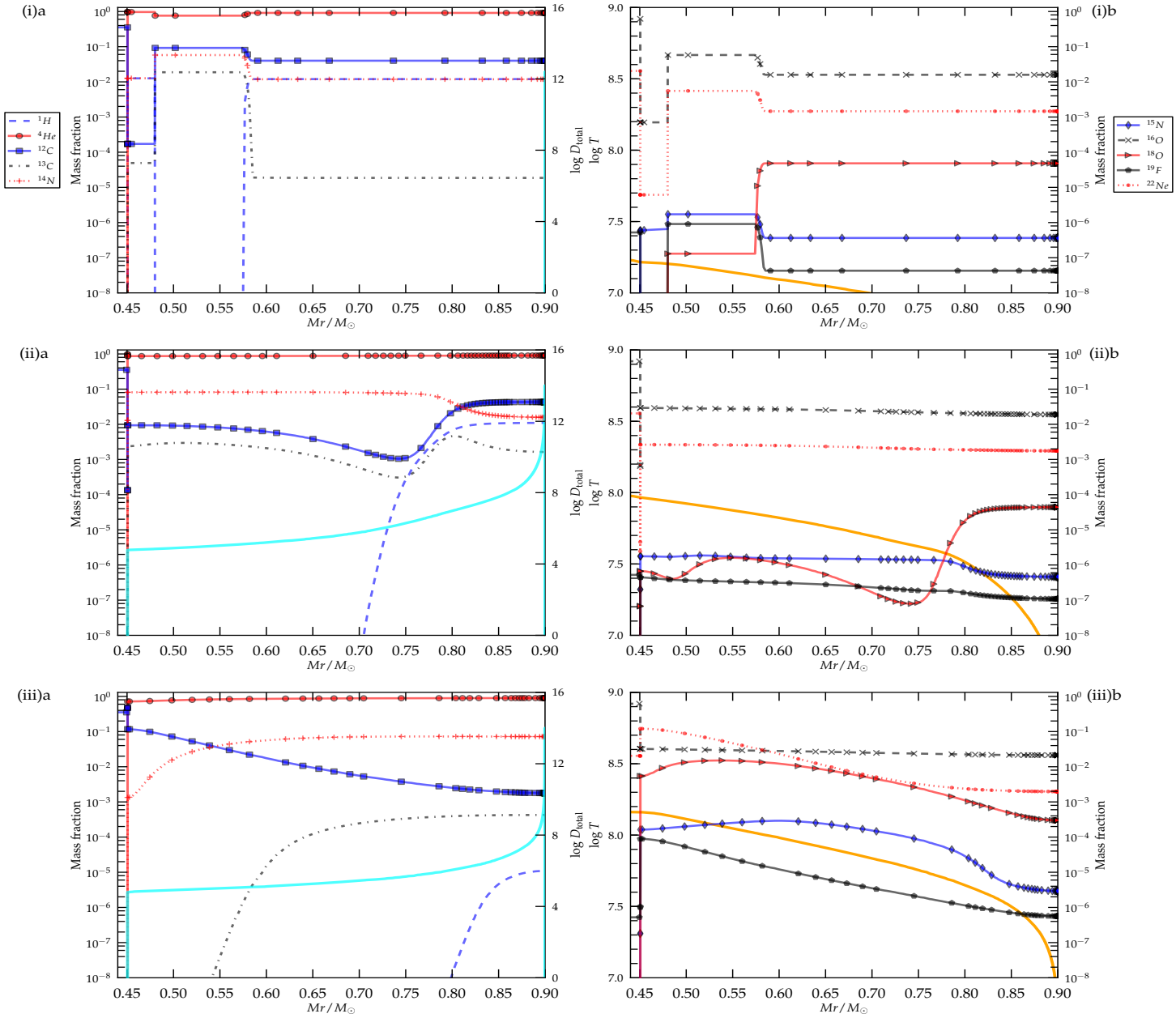

Figure 4.5: The abundance distribution for nuclear species between ^{1}H and ^{22}Ne at three timesteps of evolution of case 1. The panels correspond to the dots in Fig. 4.4. The line of every nuclear species connects the abundance of that species at every 20$^{\rm th}$ zone in the model. The panels in the left column have log $D_{\rm total}$ (solid cyan line) plotted in them and those in the right column have log T (solid orange line).

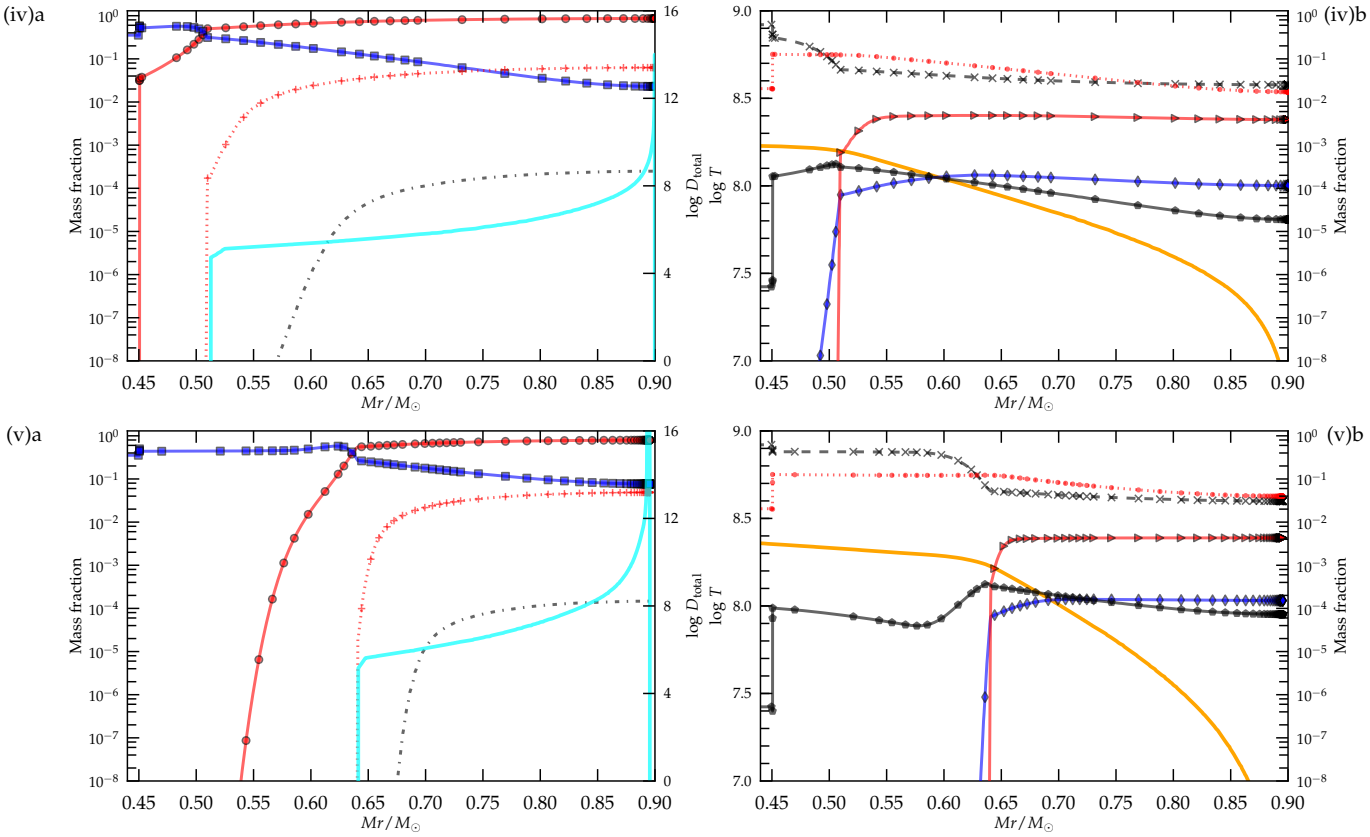

Figure 4.6: The abundance distribution for nuclear species between ^{1}H and ^{22}Ne at two timesteps of evolution of case 1. The panels correspond to the dots in Fig. 4.4 and share the same legends as Fig. 4.5. The line of every nuclear species connects the abundance of that species at every $20^{\rm th}$ zone in the model. The panels in the left column have log $D_{\rm total}$ (solid cyan line) plotted in them and those in the right column have log T (solid orange line).

at $m_{\rm min}$ (to where mixing occurs, Eqs 4.2) and then gradually moves outwards. Hence the burning of a given nuclear species begins first at $m_{\rm min}$ and then progresses to the outer layers of the star.

When the temperature at $m_{\rm min}$ is $\sim 10^8$ K, the 'He-shell burning' phase is initiated (violet dot in Fig. 4.4). By this time the H-shell has almost completely burnt outwards to become a thin layer close to the surface (Fig. 4.5(ii)a). The first neutron burst, via α-capture on ^{13}C is triggered at this time (Fig. 4.7). The ^{13}C-shell consequently moves outwards as it gets burnt to ^{16}O.

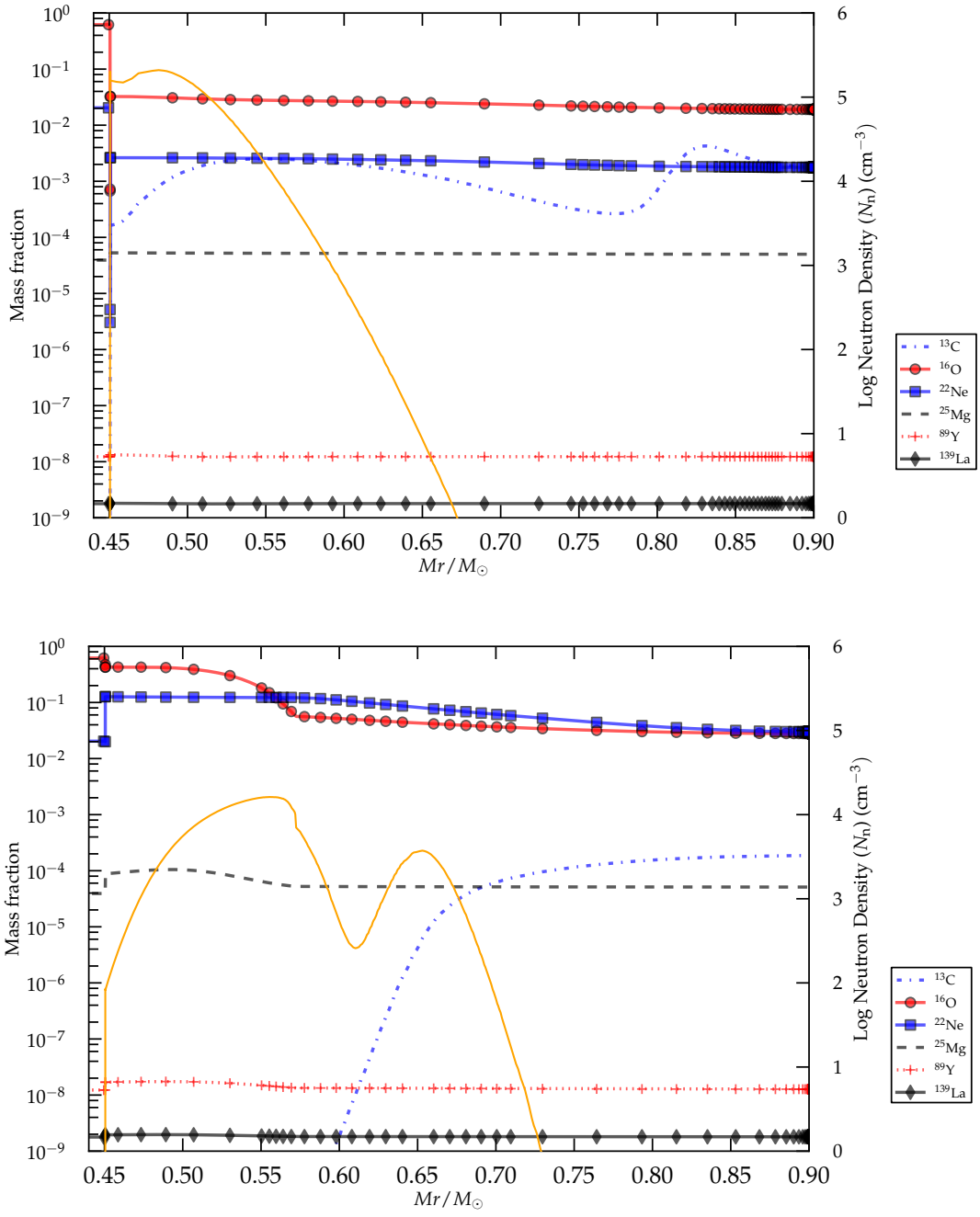

Figure 4.7: The abundance distribution of elements affecting neutron densities (indicated by the orange line) during the post-merger evolution. The top plot is at time=4.3×10^5 years (near the cyan dot) and the bottom one is at time=1.6×10^6 years (near the brown dot in Fig. 4.4).

In the time between the panels (ii) and (iii) of Fig. 4.5 (violet and brown dots in Fig. 4.4), partial He-burning of ^{14}N raises the ^{18}O to its peak value where $T \sim 1.20\times10^8$ K while some of this ^{18}O begins to get destroyed to ^{22}Ne by further α-capture closer to $m_{\rm min}$. The abundances of ^{15}N and ^{19}F also begin to increase in this time period via $^{14}\mathrm{N(n,p)}^{14}\mathrm{C(p,}\gamma)^{15}\mathrm{N}(\alpha,\gamma)^{19}$F. ^{19}F reaches close to its peak surface value in panel (iv), Fig. 4.6 (black dot in Fig. 4.4). As burning and mixing occur simultaneously, all the above species are distributed throughout the outer region of the star. It must be emphasized here that ^{18}O, ^{19}F and ^{22}Ne are created in the star during its evolution and they are mixed to the surface as they are produced, as are all the isotopes of C, N and O.

In panel (iv), Fig. 4.6, T has risen at $m_{\rm min}$ to $\sim 3.16 \times 10^8$ K, and the triple-α chain has been fully activated causing ^{12}C to increase and a further α-capture, viz., $^{12}\mathrm{C}(\alpha,\gamma)^{16}$O causing ^{16}O to rise (Fig. 4.5(iv)a). Below m_k at which the mixing profile drops sharply, complete He-burning of ^{18}O and ^{19}F to ^{22}Ne takes place. By the time the star enters the RCB phase in the HR diagram, it has a strong He-shell burning (panel (v) of Fig. 4.6, black dot in Fig. 4.4). Between panels (iv) and (v), a second weaker neutron-source, that of ^{22}Ne, is initiated through $^{22}\mathrm{Ne}(\alpha,\mathrm{n})^{25}$Mg (Fig. 4.7). The neutron densities ($N_{\rm n}$) are not very high during the post-merger evolution and range between $10^4 - 10^6$ cm^{-3}.

The mixing profile is designed to follow the shell with ^{14}N burning, as it cuts off sharply at the mass-coordinate $m_{\rm k}$ that corresponds to a certain prescribed mass fraction of ^{14}N (Eqs 4.2, section 4.2.3). Thus the material that is processed by strong He-shell burning such as ^{12}C and particularly ^{16}O are not dredged up to the surface (panels (iv)a and (v)a, Fig. 4.6) and the ^{18}O and ^{19}F isotopes above $m_{\rm k}$ are not mixed to the higher temperatures in the interior where they would be easily destroyed. Thus the formulation of the mixing profile avoids an excess pollution of ^{16}O in the surface and preserves the ^{18}O and ^{19}F already present in it.

The results of similar simulations for the other three cases of Table 4.2 are shown in Figs. 4.10 – 4.13, where they are compared with observations in section 4.3.3.

On the creation and destruction of ^{18}O and ^{19}F

The ^{15}N and ^{18}O isotopes are formed at an earlier stage in the star than ^{19}F due to their lower production temperatures. ^{15}N and ^{18}O are mixed simultaneously as they are produced, causing their abundances in the surface to increase. As the temperature in the star rises at a later stage, ^{19}F can be produced by He-burning of the ^{15}N brought down from the surface. However, the production region of ^{19}F is also where the ^{18}O is destroyed to ^{22}Ne by

α-capture. The mass coordinate $m_{\rm k}$ lies in this region. The mixing profile must be tuned as it nears $m_{\rm k}$ in such a way that : (i) it dredges down the ^{15}N to produce ^{19}F, (ii) without destroying too much of the ^{18}O from the surface and (iii) not dredge up too high an amount of ^{16}O. The challenge thus is to enhance the surface with ^{19}F but not at the expense of decreasing ^{18}O and increasing ^{16}O. If $D_{\rm Lag}$ is kept constant all the way to m_k, then one gets an excessive destruction of ^{18}O and an over enhancement of ^{16}O. In order to avoid this, the ramp feature is introduced in the mixing profile causing it to decrease as it nears m_k. As the steepness of the ramp is increased, the mixing profile cuts off sooner and the ^{19}F created is reduced while as the steepness decreases, the mixing profile extends deeper and the surface amount of ^{18}O decreases while that of ^{16}O increases. Our choice of f, which decides the slope of the ramp, lies in the sweet spot that can bring up the maximum amount of ^{19}F without destroying too much ^{18}O and increasing the ^{16}O in the surface. The ramp feature is thus a sensitive, integral and unavoidable part of the mixing profile.

4.3.2 The Shell of Fire (SOF)

The nature of the yields of neutron-capture species, viz., those between Na-Ti and the s-process elements, from the burning of the high-T (case 4) and low-T SOFs are different. In the low-T ($1.23 \times 10^8\,K$) SOF, the neutron density ($N_{\rm n}$) reaches a peak value of $\sim 3.16 \times 10^{11}\,{\rm cm}^{-3}$ and remains nearly constant for the duration of burning of the SOF. At low-T, the neutrons in the SOF are continuously replenished by the slow He-burning of ^{13}C through the reaction $^{13}{\rm C}(\alpha,{\rm n})^{16}{\rm O}$ and are made available for n-capture reactions to take place. As a result, there is a steady increase in the abundance of s-process elements along with nuclei such as Ti (Fig. 4.8) and a proportionate effect on other species between Na-Ti. On the other hand, the ^{13}C in the high-T ($2.42 \times 10^8\,K$) case is quickly destroyed by He-burning within 10^4 seconds and although $N_{\rm n}$ reaches a higher peak value of $\sim 10^{14}\,{\rm cm}^{-3}$, it is immediately consumed by neutron poisons such as ^{14}N and ^{14}O (Eq. 3.3, Fig. 3.10). Later at 10^5 seconds, the neutron density once again increases and reaches a lower peak value of $\sim 6.31 \times 10^{10}\,{\rm cm}^{-3}$ through weaker neutron-sources such as $^{17}{\rm O}(\alpha,{\rm n})^{20}{\rm Ne}$. But these neutrons are also immediately destroyed by the same neutron poisons mentioned above. As a result of the lack of availability of neutrons, s-process elements and elements between Na - Ti are largely unaffected in the high-T SOF, and remain close to their initial values (Fig. 4.8). Within the short-period (8.2×10^5 s) of burning, the abundances of these elements in the low-T case too are not very different from their initial values; hence within this period, the yields of these elements from both the SOFs are the same. However, on increasing the

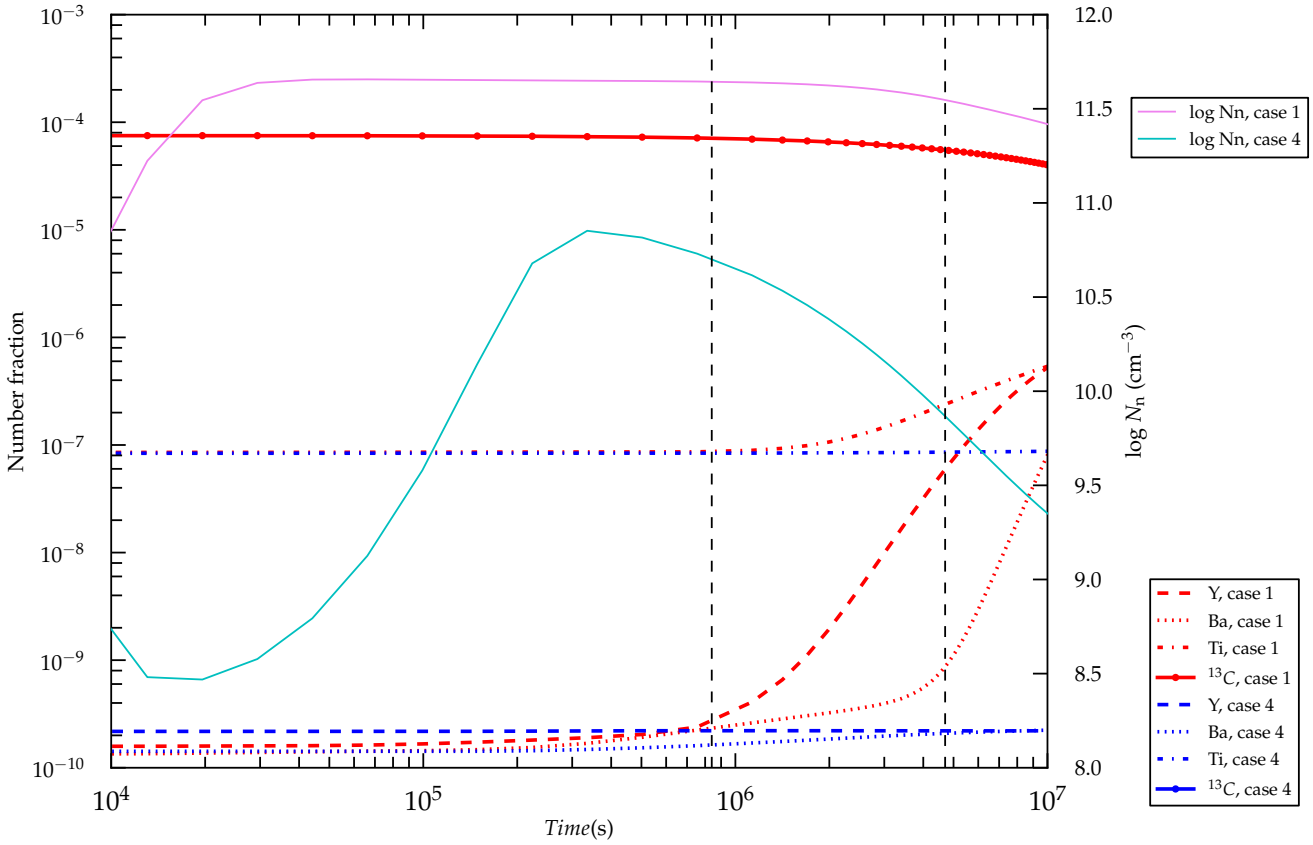

Figure 4.8: The evolution of the abundances by number fraction of ^{13}C(/100), Y, Ba and Ti during the burning of the SOF, along with that of the neutron density (log $N_{\rm n}$), in the low-T and the high-T SOFs. The vertical dashed lines indicate the short-SOF ($8.2 \times 10^5\,s$) and long-SOF ($4.7 \times 10^6\,s$) durations.

duration of burning of the low-T SOF, the abundances of s-process elements become much higher than the high-T case. The long-period SOF (4.7×10^6 s) is the point up to which the s-process elements in the low-T SOF are within the observed upper limits of RCBs.

The situation changes during the post-merger evolution phase. In case 4 (of a low-q, high-T SOF), there is a considerable enhancement of s-process elements in the surface, unlike in cases $1-3$. This is because in case 4, there is a higher dredge-up mass, along with a higher initial abundance of ^{12}C and protons, which together result in the generation of a larger amount of the n-source ^{13}C. Therefore, a higher density of neutrons is produced ($N_{\rm n} \approx 10^6\,{\rm cm}^{-3}$) in case 4 than in cases $1-3$ ($N_{\rm n} \approx 10^5 - 10^4\,{\rm cm}^{-3}$) (Fig. 4.9). The $N_{\rm n}$

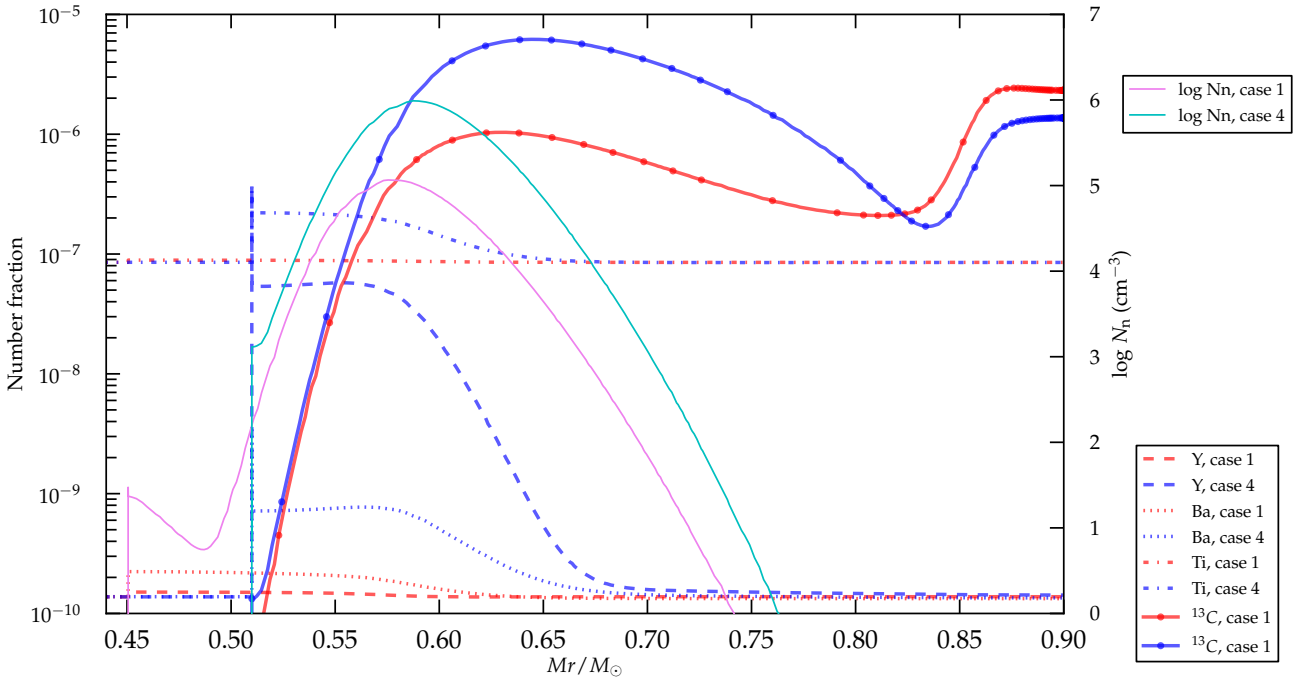

Figure 4.9: Abundances by number fraction of ^{13}C(/100), Y, Ba and Ti during the post-merger evolution of cases 1 and 4, along with neutron densities (log N_n). The snapshots of time for these profiles are at 3.1×10^5 years (case 4) and 4.5×10^5 years (case 1, between the cyan and the violet dots in Fig. 4.4).

of case 4 increases the abundances of s-process elements by up to ~ 1 dex from their initial values and also significantly affects the abundance of species between Na-Ti.

To summarize, the low-q case with a high-T SOF, enhances its s-process elements with the neutron flux available during the post-merger evolution phase, while the high-q cases with low-T SOFs, produce the s-process elements in the SOF before the post-merger evolution. The same reasoning applies to the abundances of elements between Na-Ti. The SOF, which is a characteristic of the dynamic phase, at low-T has a burning timescale that is determined by the abundance of its s-process elements; longer the burning period, higher their abundances. Thus nucleosynthesis processes directly probe features of the dynamic merging phase, making the SOF a vital feature whose physical parameters decide the fate of the spectral features of the star.

4.3.3 Comparison of the surface abundances in our models with observations

RCB stars are classified into two categories based on their values of [Fe] and Si/Fe and S/Fe ratios (Lambert & Rao, 1994). RCB minority stars (plotted as black squares, Fig. 4.10) are identified as having lower [Fe] and higher Si/Fe and S/Fe ratios than the majority (plotted as black stars, Fig. 4.10). We take the data compilation in Jeffery et al. (2011) of measured elemental abundances of RCBs and use the solar scaled log representation of abundances viz., [X]= $\epsilon_i - \epsilon_{i_\odot}$ where $\epsilon_i \equiv \log n_i + C$, n_i being the relative number abundance of species i. This data summary does not include the individual error bars on each data point, but in general the errors are quoted to be 0.2-0.3 dex.

C>N>O : constraints on the mixing

The distribution of RCBs in the (C+O)/N vs. C/O plane shows that the majority of RCB stars lie in a particular range of (C+O)/N ratio, of 1-3 and are more spread in their C/O ratio, with most RCBs having a value of 1-10 (Fig. 4.10). We find that on Keeping the amount of mixing constant at the initial value of $D_{\rm Lag}$ in our models, the ^{14}N in the envelope reduces continuously by being burnt to ^{18}O and this causes an overall decrease in the mass fraction of nitrogen in the surface. On continuing the evolution of the model at the same rate of mixing up to the end of the RCB phase, the (C+O)/N ratio increases at least by up to a factor of 3 higher than its value in most RCB stars (except for 3 stars in Fig. 4.10 but these have N>O). If the rate of mixing is lowered and restricted to smaller depths from the surface once the model attains the (C+O)/N and C/O ratios of most RCBs (the empty circles in Fig. 4.10), the ^{14}N on the surface is preserved through the RCB phase of the star. Thus in order to attain the distribution of C, N and O of RCBs, our models strongly indicate that the magnitude of mixing and its reach from the surface must decrease with time. Schwab et al. (2012) find that continuous transportation of angular momentum from the merged system causes differential rotation to reduce in the envelope. Although the timescale over which they see this happen in their simulations is shorter than what our models indicate, the idea that such a reduction in mixing driven by rotation can happen is very feasible.

The difference in the surface abundances between restricting mixing at the time when the model lies in the observed domain of (C+O)/N and C/O and on continuing mixing as the star enters the RCB phase, is not significant for elements between Na and La. However a considerable difference of the order of 0.5 dex does arise in the C, N, O and F abundances

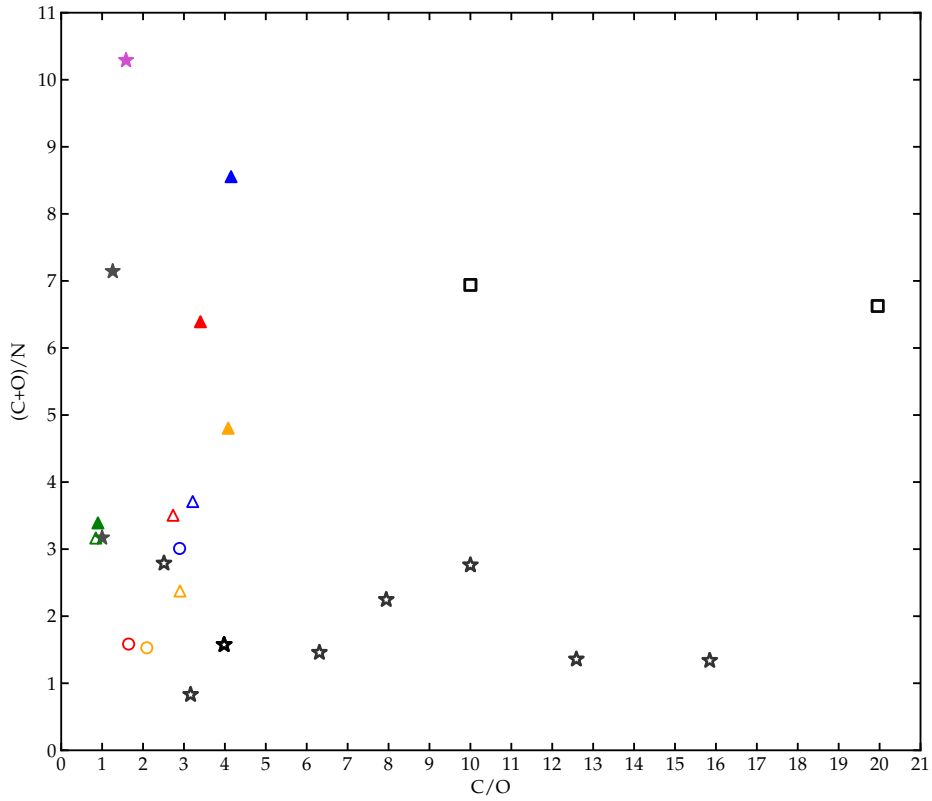

Figure 4.10: The (C+O)/N ratio of the four computed cases (case 1 (orange symbols), case 2 (red symbols), case 3 (blue symbols) and case 4 (green symbols)) and in RCBs (minority - black squares, majority class- black stars) against their C/O ratio. Two minority stars have been omitted due to their C/O ratio being out of the range of the plot. R CrB is indicated by the magenta star in the plot. Plotted for every case is the surface value of these ratios when the model is within the RCB range (empty circles), when it enters the RCB phase in the HR diagram (Fig. 4.4) (empty triangles) and when it leaves this phase (filled triangles). All observed RCBs that have N<O in their surface are indicated by filled symbols.

as seen in in Fig. 4.11). Case 4, does not at any point of time in its evolution have a model with C>N>O on its surface (hence the absence of circles in Fig. 4.11) and its O-content is almost the same as the C-content in its surface.

Surface abundances

The [X] values of the observed nuclear species in majority and minority RCBs are shown in Fig. 4.13, along with the lowest and highest values of each element from the four cases, between the time when star attains the observed C/N and N/O ratios in RCBs and when it exits the RCB phase in Fig. 4.4. Our models are in good agreement with the range of observed abundances of individual nuclear species as well as the observed isotopic ratios (Figs. 4.10 – 4.13).

As RCBs are associated with the old bulge population (intermediate Pop II, section 1.1), we assume that their range of Fe abundances reflect their initial metallicity. Our models were constructed with solar metallicity, which allowed us to take advantage of our detailed nucleosynthesis and stellar evolution progenitors models, currently available only at this metallicity. Fortunately this does not effect the relevance of our models for comparison with observations in any significant way. The nuclear species in our models can be divided into primary and secondary types, depending on the nature of the processes that affect their abundances. With this difference in mind our models can be compared with observations of RCB stars for a range of metallicities in the following way.

The primary elements are formed entirely from the burning of H and He and so, are independent of the initial [Fe] abundance of the star. Therefore in (Fig. 4.13) one must compare only between the [X] values of these elements between the models and the observations.

The abundances of secondary elements in the model depend on the proportion of their seed nuclei which were formed in previous generation of stars. These include species between Na and Ti and the s-process elements. Therefore, in Fig. 4.13, one must compare the offset of the [X] value of the element with the dashed teal line (which stands for the solar scaled composition).

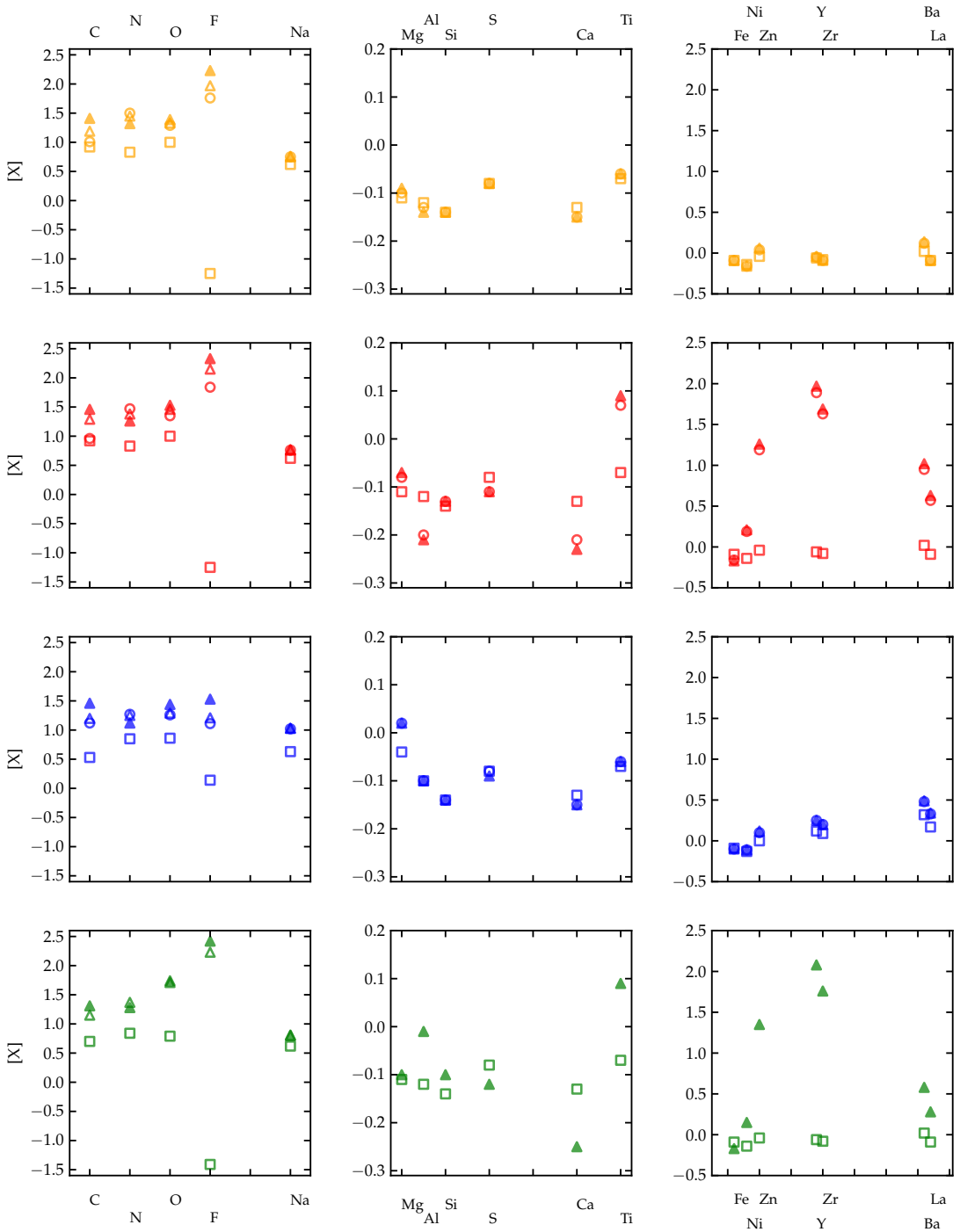

Figure 4.11: Surface [X] abundances of case 1, case 2, case 4 and case 4. The empty squares stand for the initial envelope abundance while the meaning of the rest of the symbols are as explained in Fig. 4.10. For species between Mg to La, the difference in abundances between the models that enter and exit the RCB phase is < 0.2 dex, hence only the average abundances of these species in this phase are plotted (filled triangles).

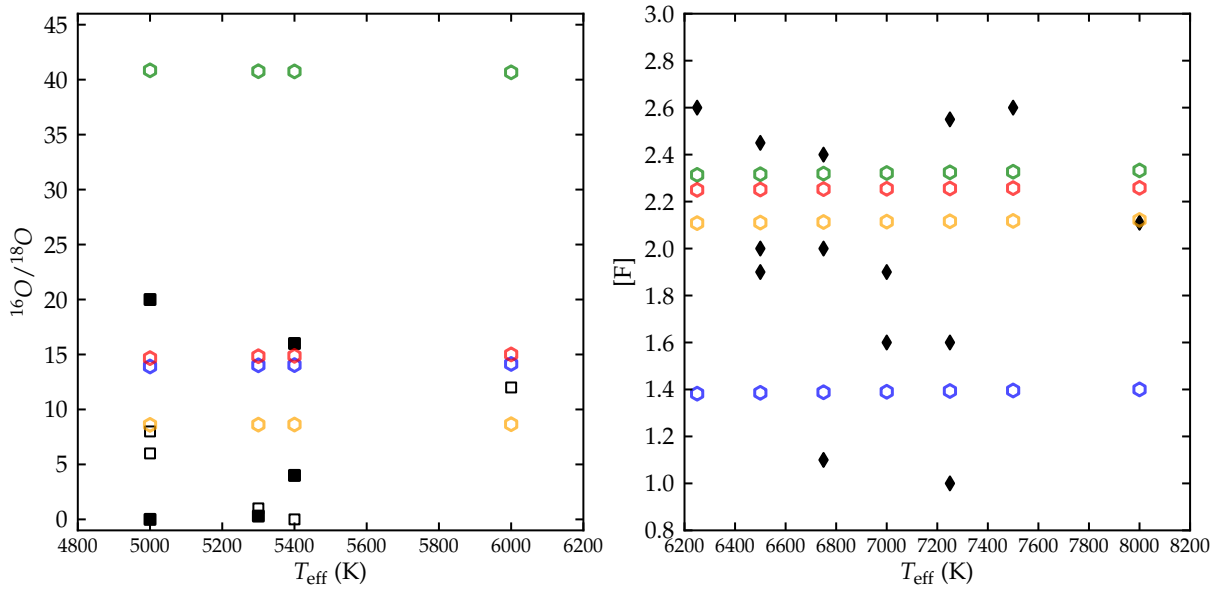

Figure 4.12: Surface $^{16}O/^{18}O$ ratios (squares are the observed data; empty squares from Clayton et al. (2007) and filled ones from García-Hernández et al. (2010)) and [F] (black diamonds are the observed values from Pandey et al. (2008)) against $T_{\rm eff}$ for the four cases (colours are the same as in Fig. 4.11). The model abundances of the nuclei plotted here (hexagons) are averaged between the timesteps at which the star enters and leaves the RCB phase (Fig. 4.4).

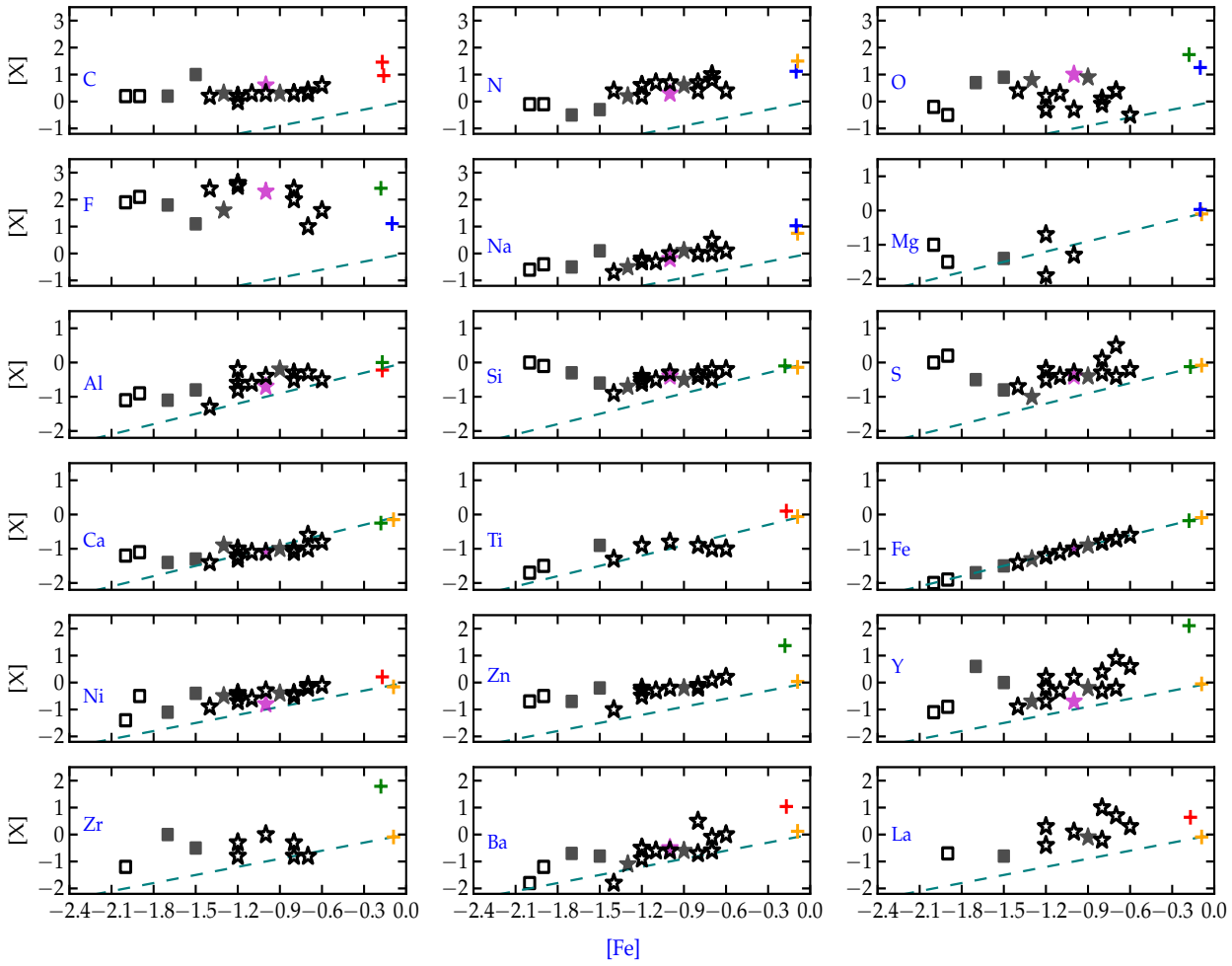

Figure 4.13: The elemental [X] values in the observed RCBs and their range from our cases. The crosses represent the maximum and minimum values of the given element from the four cases (colors according to Fig. 4.11) after the star becomes an RCB star. The dashed lines across each panel show the expected abundances by scaling the solar composition with [Fe].

An element by element discussion follows:

H and Li : The extremely low amounts of hydrogen reported in all RCBs, is a natural outcome of our models. But Li being a fragile element is easily destroyed by H- and He-burning during the merging phase of the WDs itself and consequently in our models too. Therefore we do not include H and Li in the discussion of surface abundance results.

Primary elements

C, N, O and F : One of our main objectives in this work was to find the characteristic high enhancements in fluorine and the low $^{16}O/^{18}O$ ratios of RCBs. Fig. 4.12 shows the strong agreement that our models have with the observed range of these species. Three of the cases have O-isotopic ratios between 6-15 that are within the measured range in RCBs, while this value is higher by a factor of 2 in case 4. The computed fluorine abundances too are spread over nearly the whole range of observed values, the maximum value being 2.3 dex while the observed maximum is slightly higher at 2.7 dex. The $^{12}C/^{13}C$ value is > 300 in our models and goes up to the order of ~ 1000, which is higher than the lower limit of 100 for this ratio.

The C, N, O and F abundances in the surface of the models, rely exclusively on the nucleosynthesis during the post-merger evolution phase. Independent of the choice of the progenitor, the surface C, N and O values of the four cases are within the same order (Fig. 4.11). The surface F abundances are close to each other between cases 1, 2 and 4 (within a factor of 1.5, Fig. 4.12). The highest F abundance is obtained in case 2 since some of it was generated in the SOF by He- burning, while the lowest is in case 2 due to a much smaller depth of mixing, which led to a smaller mass available to produce it. Case 4 has the highest amount of O since its initial SOF was burnt at 2.42×10^8 K, thereby increasing the initial ^{16}O. This is reflected in the high O-isotopic ratio ~ 41 of this case as well (Fig. 4.12). The model C, N, O and F abundances lie well in the observed range.

Secondary elements

Na - Ti :

Both Na and Mg are enhanced compared to initial surface values in all four cases. Na is formed by proton captures on isotopes of Ne during the post-merger evolution (see Ne-Na-Mg-Al cycle, Fig. 1.8). Thus, as the H-shell moves outwards in our simulations (Fig. 4.5(i)a),

the abundance of Na increases throughout the envelope. Na is also initially enriched in case 3 due to its production in the A-TP AGB progenitor used to construct the CO WD of this case.

Al is first generated by proton-capture on Mg isotopes and later, being a neutron poison is destroyed by (n,p) reactions once again to Mg via, $^{26}\mathrm{Al(n,p)}^{26}\mathrm{Mg}$. The Mg content also increases by proton-capture on ^{23}Na. Thus, although Mg is increased in all 4 cases, the level of reduction of Al depends on the interplay between the temperature and burning timescale in the SOF, which explains why the Al abundances can be either higher (cases 1 and 2) or lower than its initial value in the envelope (cases 3 and 4).

The abundance of Ca decreases in all cases, due to n-capture reactions on its isotopes. $^{40}\mathrm{Ca(n,g)}^{41}\mathrm{Ca}$ is a significant n-capture channel and the ^{41}Ca thus formed is used up by further (n,p) and (n,α) reactions, thus decreasing Ca. The reaction chain that further reduces Ca is $^{44}\mathrm{Ca(n,g)}^{45}\mathrm{Ca}(\beta^-)^{45}\mathrm{Sc}(\beta^-)^{46}\mathrm{Ti}$ and in the process increases the amount of Ti. Due to these processes taking place in our models, Ca is depleted and Ti is enhanced.

For the species between Al-Ti, the abundances are independent of the choice of the progenitor AGB model. In cases 1-3, these elements are changed in the long-SOF of low-T, whereas in case 4, their abundances are changed during the post-merger evolution phase (as discussed in section 4.3.2).

From Fig. 4.13, the range of Na values from our models is consistent with the data trend, while those of Al are in marginal agreement with the enrichment levels seen in RCBs. Since there are only 6 stars which have Mg measured and as they are well scattered, it is difficult to draw out a trend in this element; we only barely get the upper limits and do not get the decrements, as seen in two of those stars. Upper limits are also closely achieved in Ti and Ca, while our lower limits do not reach down to those found in some RCBs. Ca is seen to be enriched in a few RCBs, which none of our models show.

Si and S hardly change in all four cases, as temperatures are not hot enough to produce them in the initial SOF or in the star itself. Thus our models do not show the overabundances of Si and S observed in RCBs (see discussion below).

s-process elements : The abundances of s-process nuclei depend on the seed Fe nuclei available in the star (section 1.3.4). Although the neutron source is primary (^{13}C), the main neutron poison is also primary (^{14}N), and therefore the s process is secondary. Thus as one would expect, the [X/Fe] of s-process elements should rise more or less with increasing [Fe].

Except for a very small number of stars, all RCBs show an enhancement in s-process

elements compared to solar on their surface as do our models. The low-T SOF is especially efficient at producing s-process elements and the surfaces of the post-merger evolution models of cases 1-3 which were constructed with this SOF, reflect the abundances of these elements as formed in the SOF (section 4.3.2), while in case 4 (with the high-T SOF), the s-process elements are enhanced during the post-merger evolution. The highest abundances of s-process elements are produced in case 2 (with the long-SOF) and case 4 (Fig. 4.13). We achieve the whole spectrum of s-process enhancement seen in RCBs, except for few stars that seem to be depleted in s-process elements.

4.4 Discussions and Conclusions

We have successfully reproduced almost all the observed characteristics of RCBs in a self-consistent framework. Along with the anomalous isotopic signatures of these stars, our models lie within the observed range of species between Na-Ti and the s-process elements. These models spend between $10^4 - 10^5$ years in the observed range of luminosity and effective temperature of RCBs, which is close to their estimated lifetime from observations.

We achieve a range of $^{16}O/^{18}O$ values that are in concurrence with the observed values, as also are the surface fluorine enhancements and the $^{12}C/^{13}C$ which are much higher than the lower limit determined from spectral data. The individual elemental abundances from the models are spread over their corresponding range measured in RCBs. Thus these models many well represent the many possible thermodynamic conditions arising from various possible binary systems resulting into CO+He WD mergers.

From our study, it is found that the surface abundances of a model depend on the assumed mixing depth, the temperature and duration of burning of their SOFs and the mass ratio of the white dwarfs. The mixing limit for a model is restricted to above the CO core and is thus dependent on the choice of its AGB progenitor; the further up on the AGB it is, the more O-rich its CO core and the closer to the surface the mixing is.

The surface enhancements of C, N, O and F in the models, are due to nucleosynthesis in the post-merger evolution of the star and are dependent only on the H and He available, whose initial amounts do not vary much between the progenitor stars used to construct the WDs. Thus the evolution of these primary species are independent of the choice of the progenitor AGB star. The amount of F formed is also dependent on the depth of mixing; the lesser the depth, the lesser the mass available to produce F, the smaller the F abundance is. This explains the range in F abundance obtained in the models.

With the conditions of the SOF taken from the hydrodynamic simulations, the abundances of the species between Na-Ti and more significantly the s-process elements depend on the temperature and period of burning of the SOF. It is found that the long-SOF at low temperatures produces copious amounts of s-process elements and significantly changes the abundances of elements between Na-Ti. The SOF is the contributor of n-capture elements, especially the s-process elements, in the low-T SOF of the high-q simulations. The duration of burning of the SOF feature is constrained by the abundance of s-process elements; the longer the SOF is burnt, the higher their abundances. Thus the SOF burning period is limited such that the s-process elemental abundances are lower than the observed upper limits. On the other hand, these elements are unchanged in the high-T SOF and are affected only during the post-merger evolution of the case with such an SOF. The enrichment levels of s-process elements in the models agree with those seen in RCBs. Amongst the species between Na - Ti, barring Mg and Al, our models are in reasonable agreement with observed Ca and Ti abundances. Contrary to the prediction of previous authors, the n-capture elements, particularly the s-process elements, are not significantly contributed by the TP-AGB progenitor star but by processes in the post-merger remnant.

Along with constraining a feature directly obtained from the hydrodynamic simulations, this work also presents indicative results on the nature of the mixing during the post-merger evolution. Continuous mixing throughout the evolution of the star causes the star to become O-rich as against being C-rich. This implies that mixing due to rotation (which would probably be the primary source of mixing in a post-merger object), should reduce its rate and depth with time. Our models do not show the required overabundance of Si and S seen especially in the RCB stars with the lowest [Fe]. In light of the fact that RCB stars are rich in dust, the role of dust depletion on their abundances cannot be ruled out (Asplund et al., 1998, 2000), particularly to explain the distinctly low [Fe] values of the minority RCBs from the majority. It does not appear that the dust-gas separation in RCBs follows as it occurs in the ISM. An ISM-like dust-depletion can explain the high [S/Fe] and [Na/Fe] observed in RCBs, but not their [Al/Fe] and [Ca/Fe] values, both of which are much lower in the ISM. In particular, the Si in a carbon-rich dust environment is expected to condense into SiC grains, thus severely reducing the Si content. However all RCBs have high [Si/Fe] ratios. It should be noted however, that only amorphous graphite grains and no SiC grains have been detected in RCBs. This maybe indicative of a different dust-gas separation mechanism from that of the ISM.

Alternatively, these species are produced in O burning at $T \approx 10^9\,\mathrm{K}$, which could be

achieved in the SOF of a merger of more massive WDs (Lorén-Aguilar et al., 2009, $0.6 - 1.0 \times 10^9$K for combined mass $\geq 1.2\,M_{\odot}$). The theoretical initial-final mass relationship predicts for a given initial mass higher WD masses for lower metallicity. Assuming the initial mass function does not depend on metallicity in the range observed for RCB stars higher WD masses are expected for lower metallicity mergers, and this may be the reason for the larger enhancements in S and Si for the RCB stars with the lowest Fe content. This would also imply that RCBs are in fact $> 1M_{\odot}$ in mass.

On a preliminary note, we do see enhancements of ^{22}Ne on the surface of our models that seem to agree with the levels of Ne found in EHes. A detailed comparison of models like the ones presented here and the observations of EHe is beyond the scope of this work. A few exceptions include those RCBs that are found to be richer in hydrogen compared to the majority, four RCBs in which lithium is enhanced in their surface (Asplund et al., 2000; Kipper & Klochkova, 2006) and four other RCBs that have a relatively higher amount of ^{13}C in their surface (Rao, 2008; Hema et al., 2012), with $^{12}\mathrm{C}/^{13}\mathrm{C} \lesssim 25$. Both these characteristics are not found in our models. Recent SPH simulation results of Longland et al. (2012) indicate that any Li that maybe produced in a DD merger will have to be ejected in to the mass that forms clouds around the RCB star to be preserved. Since mass-ejection during the dynamic merger phase is not part of the hydrodynamic simulations, our models cannot predict lithium abundances from such a scenario. Thus, the question of whether Li-rich RCBs are an outcome of the FF scenario or of the merger between WDs remains open and needs a separate, more in-depth analysis.

Chapter 5

Summary and Discussions

For the first time, a thorough investigation of the nuclear processes and their resultant yields, from an evolved remnant of a CO+He WD merger has been done. The motivation to explore the conditions of these remnants, was to find how they might reproduce the surface composition of RCB stars.

Nucleosynthesis calculations performed with the conditions obtained at the end of the merging phase itself, i.e at the end of 100-1000 seconds, show that the low $^{16}O/^{18}O$ ratio, high $^{12}C/^{13}C$ ratio and high F enhancements associated with RCBs, are not found in the dynamically heated Shell of Fire (SOF) region during the merging phase of the WDs.

But, on keeping the T, ρ conditions of the SOF longer, between 10^6 and 10^9 s, the above chemical signatures were achieved. This implied that a long term period of evolution following the merger may be responsible for the observed chemical composition of RCBs. Following the dynamic merging, the remnant is expected to evolve to a rotating, spherically symmetric star with an He-burning shell, that would cause it to inflate into a giant.

To study the nucleosynthesis taking place in the stellar evolution phase of the remnant, a four-zone initial composition model, that reflects the structure of the merged object from the hydrodynamic simulations was built. This composition was relaxed onto a homogeneous star, which was then allowed to evolve over a period of$\sim 10^6$ years. During this period, the star evolved to a giant in the RCB domain of the HR diagram where it stayed for $\sim 10^4 - 10^5$ years, which is well within the predicted timescale of RCBs from observations.

The surface abundance pattern of RCBs from the long-term post-merger stellar models were successfully reproduced. These models achieved a quantitative range in elemental abundances which spanned their corresponding observed range in RCBs, thus representing a distribution of possible binary systems that would have been responsible in producing the

observed range. Our success includes the primary elements, C,N,O and F and the secondary elements between Na - Ti (except for Si and S) as well as the s-process elements.

The primary elemental composition in the surface of the models, are predominantly produced in the star during its post-merger evolution. The situation for the secondary elements is slightly more complicated. When the SOF is burnt at low temperatures ($\leq 1.23 \times 10^8$ K), the abundances of s-process elements increase and those between Na-Ti change substantially. Those post-merger evolution cases (of high mass-ratio, $q = 0.7$) that were built with this SOF, dredge up the content of these elements from the SOF alone and do not produce/destroy them during the evolution itself. On the other hand, the secondary elements are unaffected during the burning of the high temperature SOF (2.42×10^8 K) which is a part of the low mass-ratio ($q = 0.5$) case. Their abundances are changed during the post-merger evolution of this case, due to a higher neutron density available than the post-merger evolution of the high-q cases.

The abundance of s-process elements in the low-T SOF increases in accordance with it's duration of burning, thus placing a nucleosynthesis-motivated constraint on the existence of this feature from the hydrodynamic simulations. For the cases we consider, the SOF is burnt between $10^4 - 10^6$ s. This is lower than the timescale indicated by the previous single zone nucleosynthesis results; this explains why the SOF is not where the ^{18}O, ^{19}F or the ^{12}C/^{13}C ratio originate from in the long-term stellar evolution phase.

In terms of the choice of the progenitor AGB star for the CO WD, we do not find much of an influence on the final composition of the post-merger model. This is unlike what was expected by previous work done in this subject. This result is a consequence of the limit in the depth of envelope mixing, that is imposed on the star during its evolution. The envelope mixing of the post-merger models includes convective mixing arising due to internal processes in the star and an essential additional mixing component that may be attributed to the rotation of the merger remnant. This mixing extends only in to the He-rich layers of the CO WD; extending it deeper in to the CO core would cause an extensive amount of ^{16}O to be dredged up to the surface and make the star O-rich, as against C-rich. The post-merger models thus implied that the dredge up which occured well into the core of the CO WD from the results of the hydrodynamic simulations, may be far too high.

Despite this initial constraint on the dredge-up depth, the star still tended to become increasingly O-rich and N-poor in the surface, because of the ^{18}O and ^{16}O produced during its evolution and the ^{14}N decreasing due to He-burning. This indicated the need for another constraint on the mixing phenomenon. In order to keep the surface composition at C>N>O,

as is wont in RCBs, we find that the magnitude of mixing in the envelope must be decreased. This ties well with the result that the differential rotation in the envelope of the merger remnant decreases with time, as ascertained in studies of post-merger remnant evolution by other authors.

Along with the few exceptional RCBs that show Li and ^{13}C enrichment in their surfaces, our models cannot replicate the overabundances of Si and S seen in almost all RCBs. As RCBs do belong to the bulge population of the Galaxy and have relatively low [Fe] values, these may indicate that these stars have originated from progenitors of lower-metallicities. From the IMF, lower-metallicity stars are higher in mass and these stars are relatively over-abundant in Si and S with respect to their Fe content, due to having undergone O-fusion. The results of mergers of high-mass WDs from previous SPH simulations, with a total mass greater than the current expected mass of $\sim 1M_{\odot}$ for RCBs, produce Si and S even during the merging phase. Thus if RCBs originate from low-metallicity, high mass stars, then their masses should be greater than $1M_{\odot}$. It is thus essential to perform an investigation such as the one carried out in this thesis, of the long-term evolution of the remnant of high-mass WD mergers and compare the nuclear yields from the results of this evolution to those of RCBs. On a preliminary note, an SOF with the temperature-density conditions of high-mass WD mergers found in the SPH simulations of Lorén-Aguilar et al. (2009), do show high amounts of Si and S being formed, motivating the need to perform a more extensive investigation of these mergers.

It is also essential to have an understanding of the role of dust in the circumstellar environments of RCBs on the abundances of their detected elements. Dust absorption maybe responsible in depleting certain elements (such as Fe) and thus seemingly enhancing other elements (such as Si or S). A robust theoretical model of the dust-gas separation mechanisms in graphite-rich environments such as those around RCBs, must be made available to place more stringent constraints on processes affecting their elemental abundances.

Thus overall we have accomplished our goal of simultaneously attaining all the isotopic ratios and individual elemental abundances of RCB stars with our post-merger stellar models. Hence the one-dimensional mixing profile we used, may possibly be indicative of the kind of mixing that can occur in a long-term evolution of WD merger objects and thus be useful for future 3D simulations of the same.

Chapter 6

Appendix

6.1 Validation of the EOS of the 3D hydrodynamic simulations

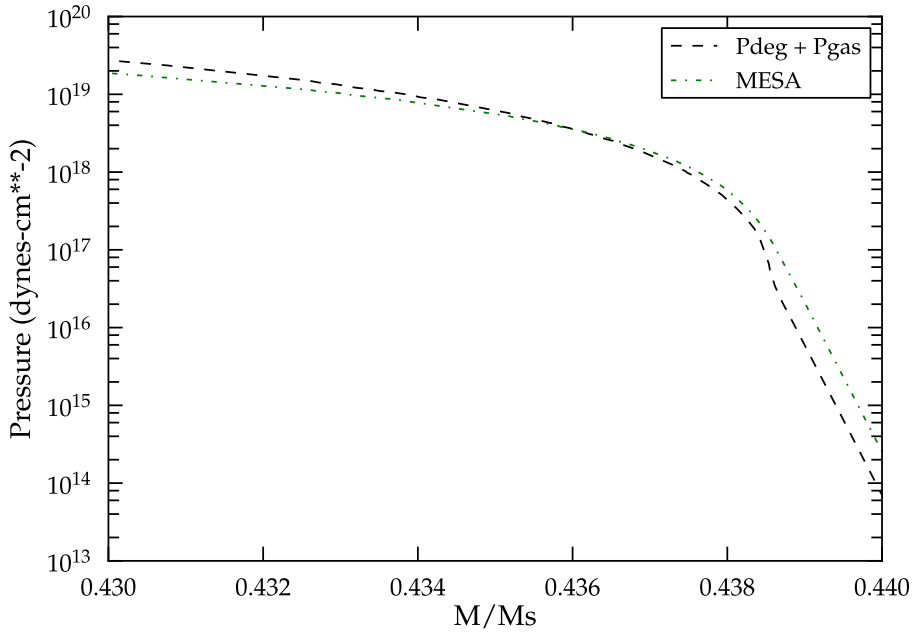

Figure 6.1: Pressure profile of a model in the 11th thermal pulse on the AGB of an initial mass of 2 $M_{\odot}$, compared against the pressure calculated using the EOS used in the hydrodynamic simulations. The region shown here is typically where the SOF is located during the course of the merger simulations.

We perform a simple validation test of the EOS used in the hydrodynamic simulations. To do this, we compare the pressure calculated using this EOS, for the density and temperature of the H-free core of an AGB model on its 11th thermal pulse (taken from the MESA Set 1.2 library, Pignatari et al. in prep) having an initial mass of $2\,M_{\odot}$, against the pressure profile given by MESA for the same model. Fig. 6.1 shows the outer portion of the CO WD where the SOF appears in the simulations. We can see the pressure of the CO WD model from MESA is very close to that obtained from the EOS used in the hydrodynamic simulations, the pressure being slightly lower within 0.436 $M_{\odot}$ and higher above it. This gives a reasonable confirmation on the choice of the EOS for the purpose of these simulations.

6.2 Nuclear energy released in the SOF

From the nucleosynthesis calculations for each q, we also compute the total energy released by nuclear processes per unit time in the SOF (Fig. 6.2). Note that the energy calculated here does not account for the loss of energy by neutrinos from weak interactions and therefore the energy added to the SOF will be lower by a factor of 1.5-2. Taking this into account, we see from (Fig. 6.2) that within the timescale of the simulation (δt in Table 3.3) the nuclear energy released is comparable to the internal energy of the SOF (depending on the initial q). The energy released in the first few hundred seconds is mainly from proton captures. Helium (for instance, triple α or $^{14}\mathrm{N}(\alpha,\gamma)^{18}\mathrm{F}$) interacts on a much longer timescale resulting in a plateau for $q = 0.5$ and 0.6 in Fig. 6.2 between 10 and 100 seconds. The extra energy released from nuclear processes may lead to higher temperatures, and these processes could play an important role in determining the temperature of the SOF. Cooling processes and dynamical effects may also be important but these cannot be estimated with our current tools.

6.3 The α-formalism construction of the binary evolution

This section is an alternative approach to the progenitor binary evolution considered in section 3.3.2.

We fix $M_{\mathrm{He\,WD}}/M_{\odot} = 0.302$ as originating from an RGB progenitor $M_{\mathrm{RGB}}/M_{\odot} = 1.65$ which has a radius $R_{\mathrm{RGB}}/R_{\odot} \sim 21$ and provide a binary evolution scenario that would lead to the CO WD models of Table 3.4, by using the α-formalism of Iben & Tutukov (1984).

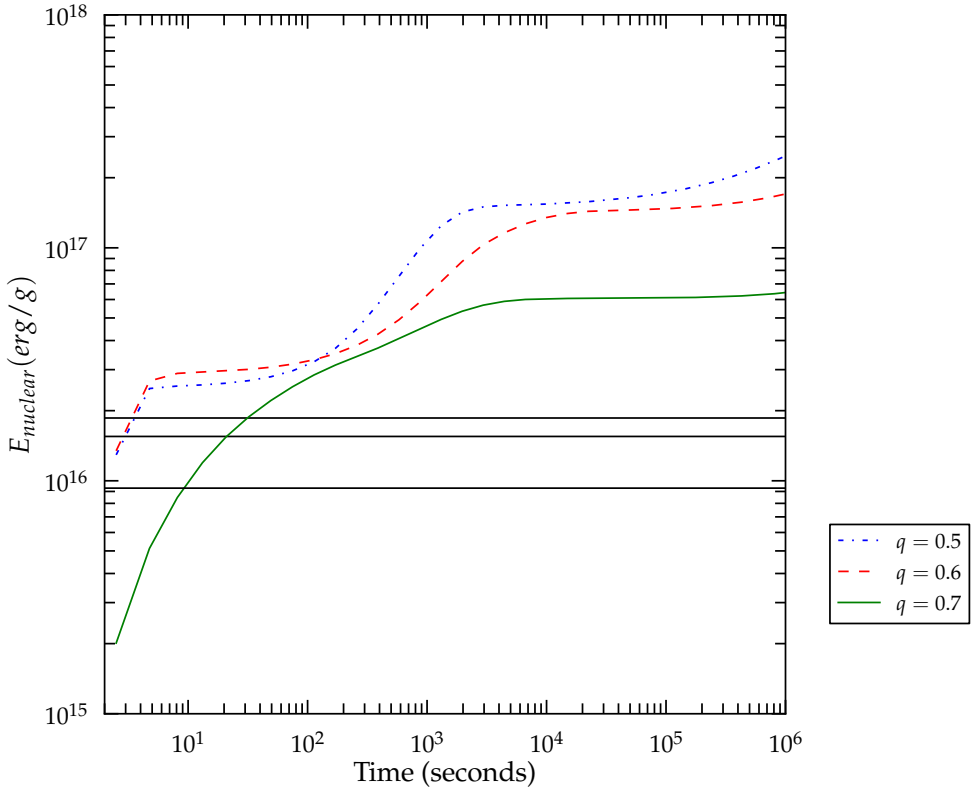

Figure 6.2: The cumulative energy via nuclear processes released as a function of time for the three cases. We note that these are upper limits on how much energy would be added to the SOF, since energy lost by neutrinos are not taken into account, and hence may be higher by a factor of 1.5-2. The solid horizontal black lines indicate the internal energy in the SOF at the end of the simulation.

The choice of the mass of the progenitors and their initial separation distances, over varying values of α, have been verified by the Binary Star Evolution (BSE) of Hurley et al. (2002) to lead to WD mergers within the Hubble time.

CO WD(1):

$R_{\rm AGB}/R_\odot$=93.25, $q = M_1/M_2$= 3/1.65 = 1.818 and α=2.

In order to know what the separation (A_1) is between the primary AGB M_1 and the secondary MS M_2 when the first RLOF occurs (that would lead to the CE event), plug $R_{\rm AGB}/R_\odot = R_{\rm L}/R_\odot$ and q into Eq. 1.1. This gives us $A_1/R_\odot$=216.3.

The mass of the remnant of M_1 (i.e, the CO WD) is $M_{1,\rm R}/M_\odot = 0.5815$. Plugging this, along with A_1, M_1, M_2 and α=2 into Eq. 1.2, we get the final separation after the first CE

event as, $A_{\rm fl}/R_{\odot}$=46.11.

Assuming the next CE event occurs soon after the first one, then with $M_1 = /M_{\odot} = 1.65$ and $M_2 = /M_{\odot} = 0.5815$, we get $q = 2.837$. Using this in Eq. 1.1 with $A_2/R_{\odot} = A_{\rm fl}/R_{\odot}$=46.11, we get $R_{\rm RGB}/R_{\odot} = 21.77$.

Our choice of $\alpha > 1$ is justified since processes such as thermal, dissociation and ionization (De Marco et al., 2011), can increase the energy in the envelope to exceed the amount gained by only loss of orbital momentum.

CO WD(2):

$R_{\rm AGB}/R_{\odot}$=223.87 and $q = M_1/M_2$= 2/1.65 = 1.212

In order to know what the separation (A_1) is between the primary AGB M_1 and the secondary MS M_2 when the first RLOF occurs (that would lead to the CE event), plug $R_{\rm AGB}/R_{\odot} = R_{\rm L}/R_{\odot}$ and q into Eq. 1.1. This gives us $A_1/R_{\odot}$=285.

The mass of the remnant of M_1 (i.e, the CO WD) is $M_{1,\rm R}/M_{\odot} = 0.5337$. Plugging this, along with A_1, M_1, M_2 and α=0.66 into Eq. 1.2, we get the final separation after the first CE event as, $A_{\rm fl}/R_{\odot}$=62.74.

Assuming the next CE event occurs soon after the first one, then with $M_1 = /M_{\odot} = 1.65$ and $M_2 = /M_{\odot} = 0.5337$, we get $q = 3.092$. Using this in Eq. 1.1 with $A_2/R_{\odot} = A_{\rm fl}/R_{\odot}$=62.74, we get $R_{\rm RGB}/R_{\odot} = 41$.

CO WD(3):

$R_{\rm AGB}/R_{\odot}$=446.683 and $q = M_1/M_2$= 2/1.65 = 1.212

In order to know what the separation (A_1) is between the primary AGB M_1 and the secondary MS M_2 when the first RLOF occurs (that would lead to the CE event), plug $R_{\rm AGB}/R_{\odot} = R_{\rm L}/R_{\odot}$ and q into Eq. 1.1. This gives us $A_1/R_{\odot}$=570.

The mass of the remnant of M_1 (i.e, the CO WD) is $M_{1,\rm R}/M_{\odot} = 0.6122$. Plugging this, along with A_1, M_1, M_2 and α=0.354 into Eq. 1.2, we get the final separation after the first CE event as, $A_{\rm fl}/R_{\odot}$=113.

Assuming the next CE event occurs soon after the first one, then with $M_1 = /M_{\odot} = 1.65$ and $M_2 = /M_{\odot} = 0.6122$, we get $q = 2.695$. Using this in Eq. 1.1 with $A_2/R_{\odot} = A_{\rm fl}/R_{\odot}$=113, we get $R_{\rm RGB}/R_{\odot} = 41$.

Bibliography

Alcock C. et al., 2001, ApJ, 554, 298

Asplund M., 1999, in IAU Symposium, Vol. 191, Asymptotic Giant Branch Stars, Le Bertre T., Lebre A., Waelkens C., eds., p. 481

Asplund M., Gustafsson B., Kameswara Rao N., Lambert D. L., 1998, A&A, 332, 651

Asplund M., Gustafsson B., Lambert D. L., Kameswara Rao N., 1997, A&A, 321, L17

Asplund M., Gustafsson B., Lambert D. L., Rao N. K., 2000, A&A, 353, 287

Badenes C., Maoz D., 2012, ApJL, 749, L11

Bergeron P., Gianninas A., Boudreault S., 2007, in Astronomical Society of the Pacific Conference Series, Vol. 372, 15th European Workshop on White Dwarfs, Napiwotzki R., Burleigh M. R., eds., p. 29

Bohm-Vitense E., 1992, Introduction to Stellar Astrophysics:, Volume 2. Cambridge University Press

Brown J. M., Kilic M., Brown W. R., Kenyon S. J., 2011a, ApJ, 730, 67

Brown W. R., Kilic M., Hermes J. J., Allende Prieto C., Kenyon S. J., Winget D. E., 2011b, ApJL, 737, L23

Clayton D. D., 1983, Principles of Stellar Evolution and Nucleosynthesis. University of Chicago Press

Clayton G. C., 1996, PASP, 108, 225

Clayton G. C., 2000, in Astronomical Society of the Pacific Conference Series, Vol. 199, Asymmetrical Planetary Nebulae II: From Origins to Microstructures, Kastner J. H., Soker N., Rappaport S., eds., p. 437

Clayton G. C., 2012, Journal of the American Association of Variable Star Observers (JAAVSO), 40, 539

Clayton G. C., Geballe T. R., Herwig F., Fryer C., Asplund M., 2007, ApJ, 662, 1220

Clayton G. C., Herwig F., Geballe T. R., Asplund M., Tenenbaum E. D., Engelbracht C. W., Gordon K. D., 2005, ApJL, 623, L141

Clayton G. C., Kerber F., Pirzkal N., De Marco O., Crowther P. A., Fedrow J. M., 2006, ApJL, 646, L69

Cottrell P. L., Lawson W. A., 1998, PASA, 15, 179

Crause L. A., Lawson W. A., Henden A. A., 2007, MNRAS, 375, 301

Dan M., Rosswog S., Guillochon J., Ramirez-Ruiz E., 2012, MNRAS, 422, 2417

de Laeter J. R., Bukilic N., 2006, International Journal of Mass Spectrometry, 252, 222

de Loore C. W. H., Doom C., 1992, Structure and Evolution of Single and Binary Stars. Kluwer Academic Publishers

De Marco O., Passy J.-C., Moe M., Herwig F., Mac Low M.-M., Paxton B., 2011, MNRAS, 411, 2277

Denissenkov P. A., Pinsonneault M., 2008, ApJ, 684, 626

Driebe T., Schönberner D., Bloecker T., Herwig F., 1998, A&A, 339, 123

Eyres S. P. S., Evans A., Geballe T. R., Salama A., Smalley B., 1998, MNRAS, 298, L37

Feast M. W., 1979, in IAU Colloq. 46: Changing Trends in Variable Star Research, Bateson F. M., Smak J., Urch I. H., eds., p. 246

García-Hernández D. A., Lambert D. L., Kameswara Rao N., Hinkle K. H., Eriksson K., 2010, ApJ, 714, 144

Geballe T. R., Evans A., Smalley B., Tyne V. H., Eyres S. P. S., 2002, APSS, 279, 39

Gonzalez G., Lambert D. L., Wallerstein G., Rao N. K., Smith V. V., McCarthy J. K., 1998, ApJS, 114, 133

Hajduk M. et al., 2005, Science, 308, 231

Han Z., 1998, MNRAS, 296, 1019

Han Z., Podsiadlowski P., Maxted P. F. L., Marsh T. R., Ivanova N., 2002, MNRAS, 336, 449

Hema B. P., Pandey G., Lambert D. L., 2012, ApJ, 747, 102

Herwig F., 2001, ApJL, 554, L71

Herwig F., 2005, ARA&A, 43, 435

Herwig F., Blöcker T., Langer N., Driebe T., 1999, A&A, 349, L5

Herwig F. et al., 2008, in Nuclei in the Cosmos (NIC X)

Herwig F., Pignatari M., Woodward P. R., Porter D. H., Rockefeller G., Fryer C. L., Bennett M., Hirschi R., 2011, ApJ, 727, 89

Hurley J. R., Tout C. A., Pols O. R., 2002, MNRAS, 329, 897

Iben I., Tutukov A. V., Yungelson L. R., 1996, in Astronomical Society of the Pacific Conference Series, Vol. 96, Hydrogen Deficient Stars, Jeffery C. S., Heber U., eds., p. 409

Iben, Jr. I., Tutukov A. V., 1984, ApJ, 284, 719

Iben, Jr. I., Tutukov A. V., 1987, ApJ, 313, 727

Iben, Jr. I., Webbink R. F., 1987, in IAU Colloq. 95: Second Conference on Faint Blue Stars, Philip A. G. D., Hayes D. S., Liebert J. W., eds., pp. 401–412

Igashira M., Ohsaki T., 2004, Science and Technology of Advanced Materials, 5, 567

Iliadis C., 2007, Nuclear Physics of Stars. Wiley -VCH

J. H. H., Olofsson H., 2004, Asymptotic Giant Branch. Springer-Verlag

Jeffery C. S., Karakas A. I., Saio H., 2011, MNRAS, 414, 3599

Jurado B., Barreau G., Bacri C.-O., 2010, Nuclear Instruments and Methods in Physics Research Section A: Accelerators, Spectrometers, Detectors and Associated Equipment, 613, 343

Kerber F., Pirzkal N., De Marco O., Asplund M., Clayton G. C., Rosa M. R., 2002, ApJL, 581, L39

Kilic M., Brown W. R., Allende Prieto C., Kenyon S. J., Heinke C. O., Agüeros M. A., Kleinman S. J., 2012, ApJ, 751, 141

Kipper T., Klochkova V. G., 2006, Baltic Astronomy, 15, 531

Lambert D. L., Rao N. K., 1994, Journal of Astrophysics and Astronomy, 15, 47

Lawson W. A., Cottrell P. L., Gilmore A. C., Kilmartin P. M., 1992, MNRAS, 256, 339

Longland R., Lorén-Aguilar P., José J., García-Berro E., Althaus L. G., 2012, A&A, 542, A117

Longland R., Lorén-Aguilar P., José J., García-Berro E., Althaus L. G., Isern J., 2011, ApJL, 737, L34

Lorén-Aguilar P., Isern J., García-Berro E., 2009, A&A, 500, 1193

Marsh T. R., Dhillon V. S., Duck S. R., 1995, MNRAS, 275, 828

Maxted P. F. L., Marsh T. R., Moran C. K. J., 2002, MNRAS, 332, 745

Motl P. M., Tohline J. E., Frank J., 2002, ApJS, 138, 121

Napiwotzki R. et al., 2001, Astronomische Nachrichten, 322, 411

Nelemans G. et al., 2005, A&A, 440, 1087

Nelemans G., Yungelson L. R., Portegies Zwart S. F., Verbunt F., 2001, A&A, 365, 491

O'Keefe J. A., 1939, ApJ, 90, 294

Paczyǹski B., 1976, in IAU Symposium, Vol. 73, Structure and Evolution of Close Binary Systems, Eggleton P., Mitton S., Whelan J., eds., p. 75

Pandey G., Lambert D. L., Rao N. K., 2008, ApJ, 674, 1068

Passy J.-C., Herwig F., Paxton B., 2012, ApJ, 760, 90

Paxton B., Bildsten L., Dotter A., Herwig F., Lesaffre P., Timmes F., 2011, ApJS, 192, 3

Pigott E., Englefield H. C., 1797, Royal Society of London Philosophical Transactions Series I, 87, 133

Podsiadlowski P., 2008a, in Astronomical Society of the Pacific Conference Series, Vol. 401, RS Ophiuchi (2006) and the Recurrent Nova Phenomenon, Evans A., Bode M. F., O'Brien T. J., Darnley M. J., eds., p. 63

Podsiadlowski P., 2008b, in Astronomical Society of the Pacific Conference Series, Vol. 391, Hydrogen-Deficient Stars, Werner A., Rauch T., eds., p. 323

Popova E. I., Tutukov A. V., Yungelson L. R., 1982, APSS, 88, 55

Rao N. K., 2008, in Astronomical Society of the Pacific Conference Series, Vol. 391, Hydrogen-Deficient Stars, Werner A., Rauch T., eds., p. 25

Rao N. K., Lambert D. L., García-Hernández D. A., Jeffery C. S., Woolf V. M., McArthur B., 2012, ApJL, 760, L3

Raskin C., Scannapieco E., Fryer C., Rockefeller G., Timmes F. X., 2012, ApJ, 746, 62

Renzini A., 1990, in Astronomical Society of the Pacific Conference Series, Vol. 11, Confrontation Between Stellar Pulsation and Evolution, Cacciari C., Clementini G., eds., pp. 549–556

Rose W. J., 1998, Advanced Stellar Astrophysics. Cambridge University Press

Ryan S. G., Norton A. J., 2010, Stellar Evolution and Nucleosynthesis. Cambridge University Press

Saio H., 2008, in Astronomical Society of the Pacific Conference Series, Vol. 391, Hydrogen-Deficient Stars, Werner A., Rauch T., eds., p. 69

Saio H., Jeffery C. S., 2000, MNRAS, 313, 671

Saio H., Jeffery C. S., 2002, MNRAS, 333, 121

Salaris M., Cassisi S., 2008, Evolution of Stars and Stellar Populations. Wiley

Schönberner D., 1983, ApJ, 272, 708

Schönberner D., 1986, in Astrophysics and Space Science Library, Vol. 128, IAU Colloq. 87: Hydrogen Deficient Stars and Related Objects, Hunger K., Schönberner D., Kameswara Rao N., eds., pp. 471–480

Schwab J., Shen K. J., Quataert E., Dan M., Rosswog S., 2012, ArXiv e-prints

Shen K. J., Bildsten L., Kasen D., Quataert E., 2012, ApJ, 748, 35

Solheim J.-E., 2010, PASP, 122, 1133

Staff J. E. et al., 2012, ApJ, 757, 76

Tisserand P., 2012, A&A, 539, A51

Tisserand P. et al., 2004, A&A, 424, 245

Tisserand P. et al., 2008, A&A, 481, 673

Tisserand P. et al., 2009, A&A, 501, 985

van Kerkwijk M. H., Chang P., Justham S., 2010, ApJL, 722, L157

Wagoner R. V., 1973, ApJ, 179, 343

Webbink R. F., 1984, ApJ, 277, 355

Webbink R. F., Iben, Jr. I., 1987, in IAU Colloq. 95: Second Conference on Faint Blue Stars, Philip A. G. D., Hayes D. S., Liebert J. W., eds., pp. 445–456

Weiss A., 1987, A&A, 185, 165

Woitke P., Goeres A., Sedlmayr E., 1996, A&A, 313, 217

Yoon S.-C., Podsiadlowski P., Rosswog S., 2007, MNRAS, 380, 933

Zaniewski A., Clayton G. C., Welch D. L., Gordon K. D., Minniti D., Cook K. H., 2005, AJ, 130, 2293